Final Report

Project No. 582-15-54181-09

CMAQ Modeling Archive for Exceptional Events Analyses

Prepared for

The Texas Commission on Environmental Quality (TCEQ)

PREPARED BY

University of Houston

4800 Calhoun Road

Houston, Texas 77204-5007

Principal Investigator

Yunsoo Choi

Project Time Period: 05/21/2015-09/01/2016

Contributors: Dr. Yunsoo Choi, Dr. Wonbae Jeon, Dr. Anirban Roy, Amir Hossein Souri, Lijun Diao, Shuai Pan, Ebrahim Eslami

Contents

List of Figures

List of Tables

Executive Summary

The effects of biomass burning emissions on regional air quality are well documented. This study produced a comprehensive evaluation of the impacts of biomass burning on regional ozone, fine particulate matter ($PM_{2.5}$) and carbon monoxide, along with other species formed due to resulting chemistry involving biomass emissions. The evaluation was conducted over the continental United States, southern Canada and northern Mexico for the ozone seasons (April-October) of 2012, 2013 and 2014. The National Center for Atmospheric Research (NCAR)'s Fire Inventory from NCAR (FINN) biomass burning inventory was used as input for the Community Multiscale Air Quality (CMAQ) chemical transport model. Meteorological fields were input by the Weather Research and Forecasting (WRF) model. Anthropogenic emissions fields were provided by the National Emissions Inventory of 2011, speciated and spatio-temporally allocated using the Sparse Matrix Operator Kernel Emissions (SMOKE) model. Biogenic emissions were modeled using the Biogenic Emissions Inventory System (BEIS) instead of MEGAN, since using the latter was shown to result in model over-prediction of several VOCs and ozone, as indicated by the literature. The model was evaluated against observations from the TCEQ's CAMS and the U.S. Environmental Protection Agency's (EPA) AQS network. This study has marked improvements over the previous biomass burning evaluations, which are as follows:

a) A longer simulation episode spanning three ozone seasons (April-October); e.g., the previous FINN evaluation conducted by AQRP project 14-011 spanned 45 days.

b) Use of dynamic chemical boundary conditions which give a more realistic physical representation of 3-D concentration fields.

c) Use of data assimilation (grid nudging) to improve meteorological fields and consequently model performance.

d) Use of a physically representative plume-rise model to evaluate the fire injection height and vertical profiles.

For evaluation and analysis, we divided our simulation to spring (April-May), summer (June-August), and fall (September-October) seasons. During 2012, broadly, in-situ (monitor) data showed ozone hotspots of 60-70 ppb across the Western Mountain region and in California, which the model did a good job reproducing. During this ozone season, biomass fires added up to 3 ppb in southern Canada in June, and similar amounts in Idaho and California in August. The time series comparisons for the state of Texas indicated that overall, the model-measurement comparison demonstrates a very good correlation across all seasons, indicating that the model is able to capture the spatio-temporal trends of the in-situ data.

Similar to 2012, in-situ data for 2013 again showed hotspots over the Western Mountain region and California. The model was able to capture hotspots over the Western Mountain region for a couple of the months (July and August) but consistently under-predicted in California. Also, the in-situ data over the eastern half of the U.S. showed quite low concentrations, 30-40 ppb. The model significantly under-predicted these in the spring month of May, and over-predicted in September; capturing these trends reasonably well in the other months. The largest wildfire impacts happened in June, August and September. The June events caused changes of up to 3 ppb in northern Mexico and southeastern Canada, along with 1 ppb in Florida, New Mexico and Colorado. Biomass impacts in August indicated changes of ~ 2 ppb in Idaho and northern

California. Impacts of 2-3 ppb impact in northeastern California were predicted for September of 2013. The time series comparisons for Texas show a good correlation in spring (0.81), but excellent correlation in summer and fall (0.93 and 0.92 respectively). However, the 2013 model tends to over-predict more than 2012. The over-prediction could potentially be due to combined problems in emissions and meteorological fields, as indicated in a submitted manuscript by Pan et al. this year.

Similar to 2013, in-situ data for 2014 again showed ozone hotspots over the Western Mountain region and in California. While the model was able to capture the hotspots over the Western Mountain region, it once again under-predicted in California. Additionally, the eastern U.S. showed low concentrations of ozone overall during the ozone season, 30-40 ppb. The model reproduced these reasonably well in April, July and October; significantly under-predicting in May by 5-10 ppb and over-predicting in June and August by 10-20 ppb. The time series comparison for Texas reported the highest over-prediction for the three years. For the month of April 2014, the model predicted 1-2 ppb changes in some places such as Georgia, South Carolina, Florida and Kansas; a 1-2 ppb impact in southeastern Oregon, northwestern Nevada and southern Idaho during July 2014, while in August, up to 3 ppb changes in western California, central Oregon, Idaho, southwestern Canada and southern Georgia.

During the summer ozone seasons of 2012, 2013 and 2014, the model was unable to capture the high $PM_{2.5}$ concentrations across the continental U.S. Large $PM_{2.5}$ impacts due to fires of up to 10 $\mu g\ m^{-3}$ in southeastern Canada were predicted for July 2012. Biomass fires in southeastern Canada elevated $PM_{2.5}$ concentrations there by 5-10 $\mu g\ m^{-3}$ during the summer months of June and July 2013. In October 2013, changes of 5-10 $\mu g\ m^{-3}$ were predicted in eastern Texas, Louisiana, Alabama, Georgia, Idaho and southwestern Canada. One interesting case in point is that for June 2014 the model significantly under-predicted when the biomass impact was minimal, indicating that probable error in biomass emissions was not the potential cause for model-measurement error.

It should be noted that ozone concentrations were 12-hr averaged values; hence concentrations were typically low during simulation episodes, even in places such as New York, Houston and Los Angeles which are known to be nonattainment regions. Additionally, the evaluations conducted through this study were on a monthly average basis; there were day-to-day events which had much larger magnitudes vis-à-vis the monthly averages. This could also explain the typically low monthly mean biomass impact numbers for ozone. A comparison of Maximum Daily 8-hr Averages (MDA8s) typically done in modeling studies could tell an altogether different story. There could be several causes behind the model-measurement discrepancies. Some of these issues could be attributed to uncertainties in emissions, chemistry and inaccurate meteorological fields. It would be helpful to conduct the model-measurement comparisons for each component of speciated $PM_{2.5}$ to understand what is driving the broadly poor model performance of $PM_{2.5}$. This study motivates the need for additional analyses on the impact of biomass burning, from Texas as well as its neighboring states, on the air quality in Texas cities, and how that could potentially impede efforts by the TCEQ and subsequently the EPA to bring Harris County and other nonattainment regions in Houston into attainment. With that end in view, it would be helpful to conduct a follow-up study exploring the impact of biomass emissions on attainment status in Texas. Additionally, it motivates the extension of the simulation episode to include 2011 and 2015, both years which experienced massive fire events in the state.

Introduction

Background

A number of major metropolitan areas in Texas currently monitor above or close to the 2008 Federal eight-hour ozone National Ambient Air Quality Standards (NAAQS) of 75 parts per billion (ppb). On December 17, 2014, the U.S. Environmental Protection Agency (EPA) further proposed to reduce the level of the ozone NAAQS to a range of 65-70 ppb putting additional areas in danger of being designated as nonattainment (79 Federal Register 242, 17 December 2014, pp. 75234-75411).

Extensive research over the past several decades shows that surface ozone and particulate matter concentrations can be influenced by emissions from wildfires burning in areas far upwind of areas which usually experience elevated surface ozone and particulate matter concentrations (e.g., Bertschi and Jaffe, 2005; Fiore et al., 2014; Jaffe et al., 2004; Jiang et al., 2012; Lapina et al., 2006; McKeen et al., 2002; Morris et al., 2006; Pfister et al., 2008; Singh et al., 1996; Sinha et al., 2004; Val Martin et al., 2006). Wildfire emissions can include ozone and ozone precursors such as oxides of nitrogen (NO_X) which often travel as peroxyacetyl nitrate (PAN) before converting back into NO_X; as well as compounds that can be chemically traced to wildfires such as carbon monoxide (CO), carbon dioxide, aerosols such as fine particulate matter ($PM_{2.5}$), carbon species (e.g., organic carbon or OC), formaldehyde (HCHO) and many others. Depending on the specific nature of compounds emitted from wildfires, these compounds can undergo photochemical reactions and can be transported very long distances at high altitudes before descending into the mixing layer and impacting surface air quality.

With this GAD, we develop model input files and perform CMAQ photochemical modeling over North America for the ozone seasons (April – October) of 2012-2014 under two scenarios: (a) with the wildfire emissions inventory, FINN, turned on and (b) with FINN turned off (this is sometimes referred to as a "zero-out" of emissions). We evaluate model results against available measurements from the surface monitoring network and, if resources permit, against validated remotely sensed retrievals from satellite-deployed instruments such as OMI (Ozone Monitoring Instrument), TES (Tropospheric Emissions Spectrometer), MOPITT (Measurement Of Pollution In The Troposphere), MODIS (MODerate Resolution Imaging Spectroradiometer) or others (e.g., Choi et al., 2005; 2008a, 2008b, 2009, 2010, 2012; Choi, 2014; Choi and Souri, 2015).

Several emission inventories for wild fires and biomass burning have been developed for use in atmospheric chemistry models. Among these is FINN which has global daily fire emissions at 1 km by 1 km resolution from 2002 to the present, available online at https://www2.acd.ucar.edu/modeling/finn-fire-inventory-ncar. The product differs from other inventories because it provides a unique combination of high temporal and spatial resolution, global coverage, and estimates for a large number of chemical species. These reasons are the potential motivation to use the FINN inventory for this study.

Objectives

Our main objectives are:

1) Evaluate the impacts of biomass burning on fine particulate matter, ozone, carbon monoxide and other related chemistry products over the continental U.S. during the ozone season for three years: 2012, 2013, and 2014.

2) Evaluate model-measurement comparisons with biomass burning emissions to quantify the impacts of biomass burning on regional air quality.

Tasks

The following tasks were completed for this work:

1) Submission of Scope of Work with budget
2) Submission of Quarterly Technical Reports
3) Processing the FINN emissions inventory to make it model-ready.
4) Comparison of model runs with and without biomass burning.
5) Documentation of the pre-processing, installation and testing of necessary modeling components.
6) Provide an archive of model input and output files along with associated metadata.
7) Submission of a Final Report (this document)

Observations, Methodology and Model Setup

Observations

The study uses observational data of several types and sources. These include NO_x and O_3 observations from remote-sensed (satellite and aircraft) and surface observations. Additionally, we use remote-sensed plume height observations. Each of these data sources is described in the following sections, along with the procedure to extract the data and make it compatible with model format.

Surface Data

Surface observational data were taken from regular measurements at the Continuous Ambient Monitoring Stations (CAMS) operated by the Texas Commission on Environmental Quality (TCEQ). The CAMS measurement network collects real-time data for species and meteorological variables. Measured parameters differ from station to station, with station density in southeastern Texas being relatively high. The location and status of these sites measuring ozone and nitrogen oxide are shown in Figure 1. CAMS data are archived by our group from the TCEQ website.

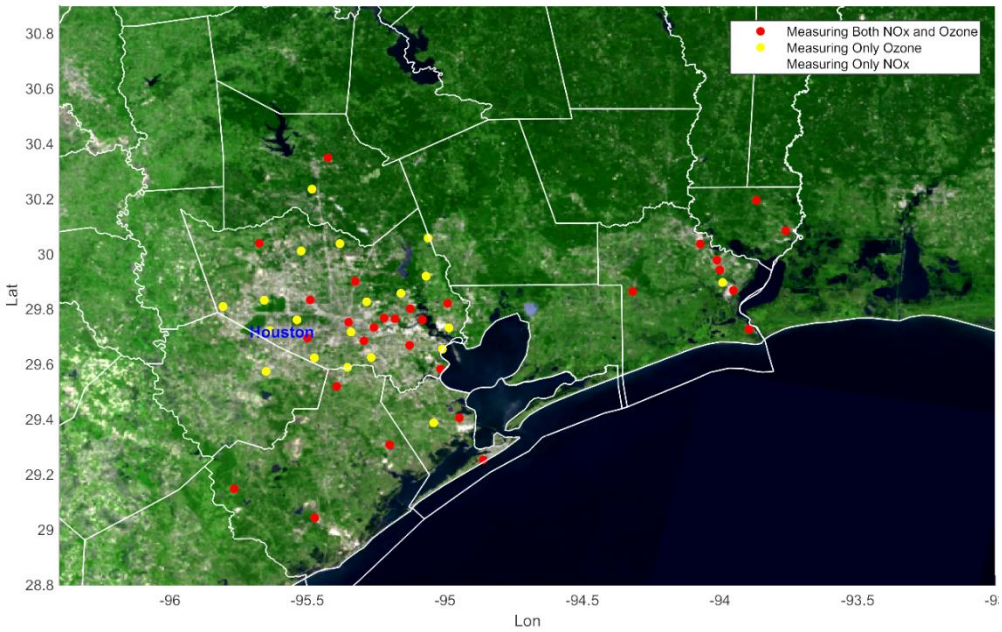

Figure 1. MODIS true color image showing the location and status of the CAMS ozone and NOx sites.

Comparison of CAMS data with model predictions is relatively straightforward. The first step is to extract model variables at the surface. The CMAQ model outputs binary netCDF files and we have developed an in-house code to extract data for any variable at any layer. To compare model value with observation from a site, we first use the latitude and longitude of a site to determine its cell location in the model grid, then extract the corresponding value from model output. The temporal frequency of model output and CAMS are both hourly, making direct comparison easy.

Additionally, we used hourly surface O_3, CO, and $PM_{2.5}$ concentrations from the EPA's AQS measurement network (http://aqsdr1.epa.gov/aqsweb/aqstmp/airdata/download_files.html). The number of ozone sites differs from month to month, but on average, 1,300 stations are available in 2012-2014. The network includes 300 CO measurements over the continental U.S. The quality of CO measurement is highly variable, and a majority of sites lack continuous hourly measurements. We attempted to reduce their uncertainties by removing any observations that included 250 ppbv as fill values, and abnormal levels; nevertheless, the comparison of CO measurements with model should be interpreted with caution. The AQS network provides abundant hourly $PM_{2.5}$ values at more than 400 sites. Stations measuring the mentioned species are more concentrated in eastern and western regions of the U.S. where the population density is higher. AQS data are archived by our group using a MATLAB code which reads and decodes the raw format file.

Remote Sensing Data

Remote-sensed ozone and NOx data from the Ozone Monitoring Instrument

NASA OMI tropospheric NO_2 (Level 2, V2.1) was also used for this project. Level 2 data has been post-processed from Level 1 (calibrated, georeferenced but unprocessed instrument data) into derived geophysical variables. Comparison of OMI data to DOMINO (Dutch OMI NO_2) indicate that the NASA product was more consistent with validation studies. It has a ground footprint varying across the instrument swath from 13×24 km^2 at nadir to ~40×160 km^2 for the edge of the orbit due to wide field of view angle and swath width (i.e., panoramic). A detailed description of NO_2 retrieval algorithms can be found in Bucsela et al. (2013). Acquired spectra sensed by OMI detectors are analyzed with the Differential Optical Absorption Spectroscopy (DOAS) method in a fitting window from 405 nm to 465 nm. Calculated NO_2 slant column densities are then corrected for instrumental defects. This is named "destriping" due to variability of effects across the orbital track. In order to convert NO_2 slant column densities to vertical ones, Air Mass Factors (AMFs) which are functions of temperature, cloud cover, topography, albedo, and other factors are calculated using a pre-computed scattering-weight table from NASA's TOMRAD forward vector radiative transfer model and monthly mean NO_2 profiles from the Global Model Initiative (GMI) simulation (here GEOS-CHEM in a $2.5^o \times 2.5^o$ grid). The uncertainties of the product vary from location to location and under different meteorological conditions. The overall error on the tropospheric vertical column density is <30% under clear-sky conditions and typical polluted conditions ($>1\times10^{15}$ molecules cm^{-2}) (Bucsela et al., 2013).

Daily granules of tropospheric OMI NO_2 are available at http://mirador.gsfc.nasa.gov/cgi-bin/mirador/collectionlist.pl?keyword=omno2.

Three important steps in preprocessing are:

1) Masking pixels having low quality

The common thresholds for performing the mask are: Solar Zenith Angle $0 \leq SZA \leq 85^0$, VCD (vertical column density) Quality Flags=0, Root Mean Squared Error of Fit < 0.0003, Terrain Reflectivity < 30% and Cloud Fraction < 20%. Note that pixels lacking below criteria are filtered out

2) Removing the vertical a priori profile impact from the granules to conduct an "apples-to-apples" comparison between model predictions and satellite data: A direct comparison of model output to OMI NO_2 requires that an a priori vertical profile of NO_2 in the OMI retrieval algorithm

(here 2.5°×2.5° monthly averaged profiles from GEOS-Chem) be minimized. Although this coarse initial guess could bias results, the main problem lies in applying an average semi-polluted profile over the large grid cell that encompasses both urban and rural regions, resulting in an underestimation of NO_2 vertical columns in urban regions and an overestimation in rural regions (Russell et al., 2011). Following the approach described in Duncan et al. (2014), we first use the variable called "scattering weight" provided for various pressure levels from the surface to the top of the atmosphere that is included in OMI NO_2 data files. We sum over all model layers the product of the scattering weight and model partial column (molecules cm^{-2}) in each model layer (up to the tropopause pressure provided in OMI HDF file). This sum divided by vertical column density of the model is called the air mass factor (AMF) of the model (AMF_{model}). Subsequently, we divide the product of VCD and AMF of satellite data from the HDF data file by AMF_{model} to obtain a modified form of vertical column density of the satellite through the following equation:

$$VCD'_{satellite} = (VCD_{satellite} \times AMF_{satellite})/AMF_{model} \quad (1)$$

Now we can directly compare $VCD'_{satellite}$ to model output. It is worth mentioning that a bilinear interpolation method is used to co-register pixels between the satellite and model.

3) Gridding granules in high spatial resolution

As outlined earlier, pixels located far from nadir experience very poor spatial resolution. In order to make a smooth and uniform gridding, a recent novel method (Kuhlmann et al., 2014) is deployed. Using a parabolic spline method in this new approach, NO_2 maps become smoother and pixels at the extremities of scan line are more accurately reconstructed. Traditionally, oversampling was the main approach to ensure high spatial resolution for regional analysis. Here, this approach is used for the first time in the field of inverse modeling without extensive oversampling.

A sample result of the corrected OMI NO_2 column is plotted in Figure 2. It is evident that adjusted OMI output differs from the unadjusted one. After adjusting OMI tropospheric NO_2, background NO_2 in rural regions decreased. The bottom panel in Figure 2 presents a very detailed OMI map for Houston. We believe this figure communicates a crucial message to the air quality community: removing the influence of the a priori profile undeniably has considerable impacts (both in magnitude and distribution) on OMI tropospheric NO_2.

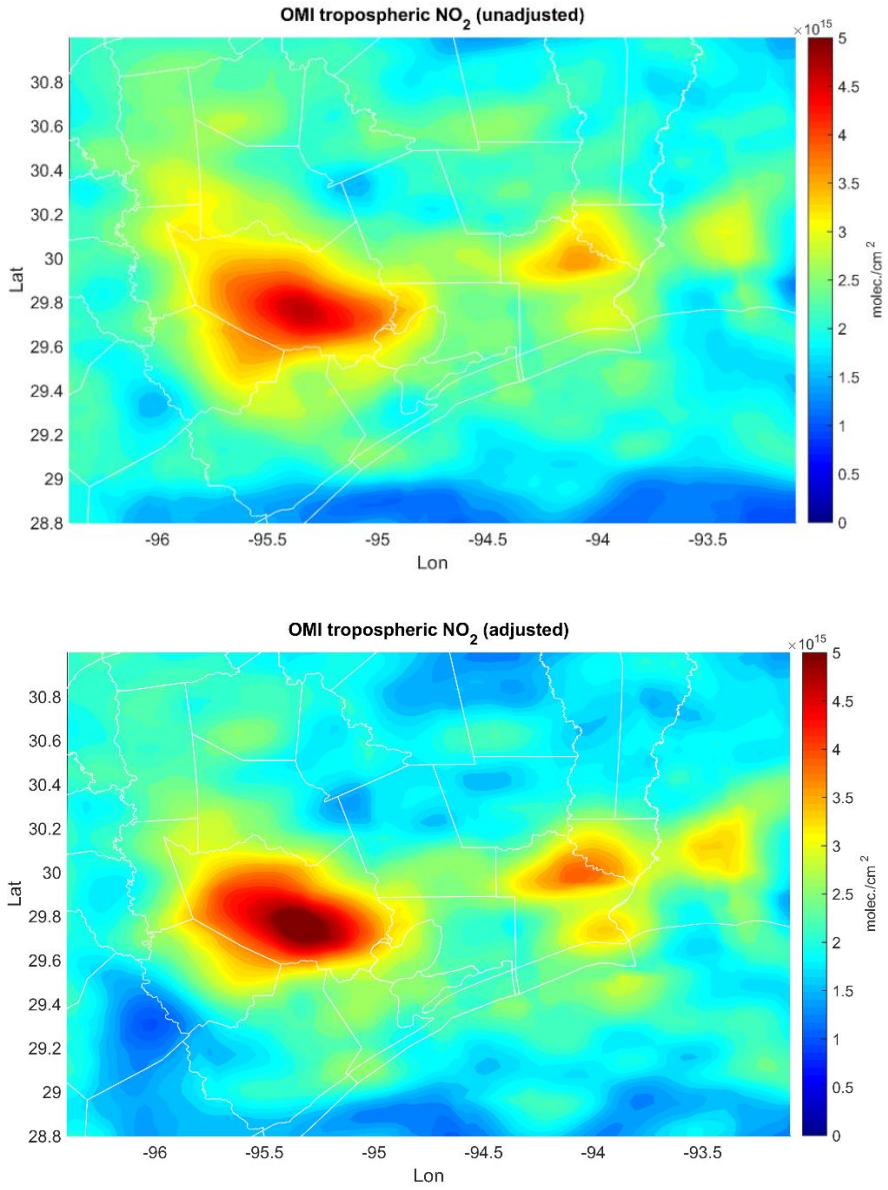

Figure 2: Top panel: average OMI tropospheric NO_2 in September of 2013. Noisy pixels have been screened out but the effect of the a priori profile remains. Bottom panel: average adjusted OMI tropospheric NO_2 in September of 2013. Noisy pixels have been screened out and the effect of the a priori guess is mitigated.

Plume height rise data to determine injection height

The plume injection height is the initial altitude at which wildfire smoke begins to be transported away by the horizontal winds. The injection height and plume top define a vertical plume transportation zone (Raffuse et al., 2012; Grell et al., 2011). Injection height is important for air quality modeling since it determines the direction and amount of smoke to be transported.

Satellite remote-sensing observations are used to provide relatively accurate values of aerosol top height. Two typical main sensors used for this application are the Cloud-Aerosol Lidar with Orthogonal Polarization (CALIOP) on board the CALIPSO satellite (an active sensor), and the Multi-angle Imaging SpectroRadiometer (MISR) instrument on board the NASA Terra satellite (a passive sensor). CALIOP can provide insight into the vertical characteristics of aerosol (i.e., magnitude and type) due to utilizing backscattered nadir laser beam in two polarizations at green and near-infrared wavelengths. However, the swath width of CALIPSO observations is too narrow (~100 m). Therefore, the coincidence of biomass burning and observed plumes occurrence is very unlikely. Consequently, we will only use it for gathering a general picture of vertical distribution of aerosols near the source rather than do a quantitative comparison in core of fires. On the other hand, the MISR swath is nearly a factor of 4×10^3 wider than that of CALIPSO. Kahn et al. (2008) stated that over the 16-day ground-track revisit cycle of both satellites, MISR is nearly 4,000 times more likely to observe buoyant plume cores than CALIOP. Thus, MISR is preferable for height injection verification in this study.

The MISR height injection algorithm is based on a stereo-photogrammetric approach involving two steps. Firstly, mean wind is derived based on two triplets of images, the 70^o and 45^o forward nadir views, and the 70^o and 45^o aft and nadir images. Subsequently, to calculate the reflecting layer height (here smoke), matching is performed between 26^o forward and nadir views, and independently between the 26^o aft and nadir views. Based on the maximum reflectance contrast, an accurate parallax is used for height retrieval. More details of the retrieval can be found in Diner et al. (1999). We estimated injection height using the MINX tool. The estimation occurs in several steps. Firstly, MODIS fire radiative power (FRP, in unit of MWatt) data are downloaded for the region of interest (here U.S.). Next, MISR granules that have observed plume cores are identified by defining the threshold of FRP and the level of uncertainty of MODIS. The source and the boundaries of each plume, and the wind direction should be selected manually and several properties regarding the matching kernel size, minimum and maximum height, the selection of camera and other parameters should be defined. The outputs of MINX are plume rise height regions with and without wind-correction. Although the wind-corrected values are few compared to no-wind case, they give a more realistic representation of smoke height. The MISR-derived plume height is based on blue or red bands which have different values. It is still not clear which one should be adopted for injection height estimation, since the blue band has only recently been included in MINX. However, generally for optically thin smoke over bright surfaces, blue bands perform matching more practically, while red bands provide better injection height for thick plumes over relatively darker surfaces (e.g., vegetation and water) which are more likely to be seen since biomass burning often happens in forested regions.

Figure 3 plots the MISR imagery plume height rise for a brush fire in Oregon on the 8^{th} of July, 2012, as calculated by the MINX software. Due to the bright surface landscape, we used the blue band and calculated plume top height accordingly. Wind-corrected top height is relatively lower than the no-wind case.

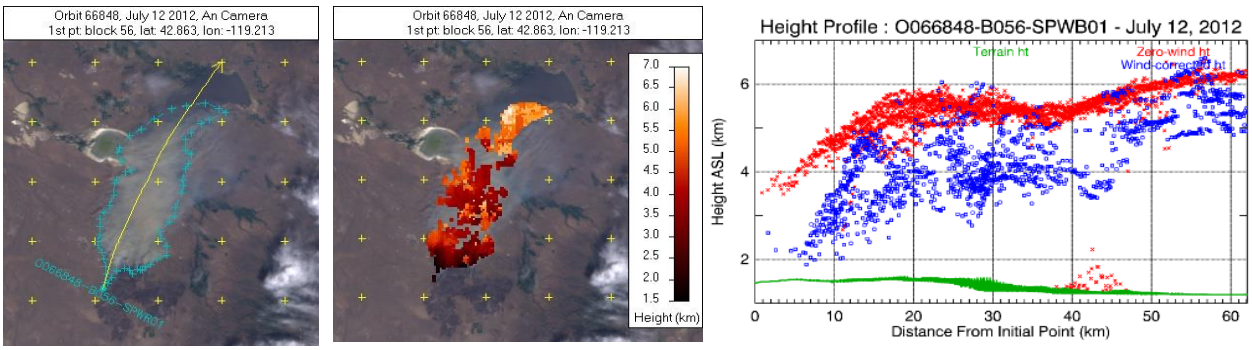

Figure 3: MISR derived plume height rise for the Oregon fire event on 8th July, 2012. The left panel shows the smoke event as detected by the satellite along with the plume boundaries and direction of the plume. The central panel shows the spatial distribution of the plume height rise. The right panel plots the plume height rise with and without wind corrections.

Methodologies used for modeling

Conversion of the FINN inventory to CMAQ format

The fire inventory from NCAR (FINN) version 1.5 provides global daily emissions of trace gases and particle from biomass burnings (Wiedinmyer et al., 2011) (available at http://bai.acom.ucar.edu/Data/fire/). The data has high spatial resolution of 1 km owing to the MODIS Thermal Anomalies Product used for fire detection. The land cover/land use (LULC) of the spotted fire is initially classified by the MODIS Collection 5 Land Cover Type (LCT) product for 2005. Vegetation density in each fire pixel is assigned based on the MODIS Vegetation Continuous Fields (VCF) product. Emissions are speciated for MOZART-4, SAPRC-99 and GEOS-Chem chemical mechanisms for global and regional model applications.

The steps involved in the conversion were (a) re-gridding the FINN inventory to the model grid cell resolution; (b) mapping the speciation lumping of VOC and $PM_{2.5}$ emissions, since FINN was speciated for MOZART while CMAQ needed CB05; and (c) vertical allocation of fire emissions. Each of these is described in detail below.

Re-gridding of biomass burning emissions

The FINN emissions were re-gridded to the CMAQ domain using the utility provided by the data developer. After re-gridding, species fire emissions (in moles $km^{-2}\,h^{-1}$) were classified by fire sizes (in m^{-2}) and area fractions of four vegetation types, tropical forest, extra tropical forest, savanna, and grassland. For gases, emissions (in moles s^{-1}) required by the SMOKE processing were calculated as:

$$\text{emissions (moles s}^{-1}\text{)} = \text{emissions (moles km}^{-2}\,\text{h}^{-1}\text{)} \times 144 / 3600 \qquad (2)$$

The number 144 comes from the area of a grid cell of our domain which is of size 12 km × 12 km.

Aerosols (from µg m^{-2} s^{-1} to g s^{-1}) were made in a similar way as:

$$\text{emissions (g s}^{-1}\text{)} = \text{emissions (µg m}^{-2}\,\text{s}^{-1}\text{)} \times 144 \qquad (3)$$

Emissions were assumed to represent the center of the grid cells.

Mapping from MOZART-4 to CB05

Table 1 lists the mapping from MOZART-4 to CMAQ cb05tucl_ae6_aq speciation profile developed by Tai et al. (2008).

Since CMAQ v5.0, primary $PM_{2.5}$ emissions are split into 18 species: organic carbon (OC), elemental carbon (EC), sulfate (SO_4^{-2}), nitrate (NO_3^-), water (H_2O), sodium (Na^+), chloride (Cl^-), ammonium (NH_4^+), selected trace elements (Al, Ca^{2+}, Fe, Si, Ti, Mg^{2+}, K^+, Mn), non-carbon organic matter (NCOM) and un-speciated fine PM (PMOTHR). Primary unspeciated coarse particulate matter (PM) is named PMC (Simon, 2015).

In the FINN inventory, $PM_{2.5}$ includes OC and EC. $PM_{2.5}$ particles are a subset of PM_{10}.

Table 1: Mapping of MOZART-4 to CMAQ cb05tucl_ae6_aq species.

cb05tucl_ae6_aq	**MOZART-4**
NO	NO
NO_2	NO_2
CO	CO
FORM	CH2O
ALD2	CH3CHO
ALDX	GLYALD
ETOH	C2H5OH
MEOH	CH3OH
ETHA	C2H6
PAR	C3H6 + 1.7*BIGENE + 5.0*BIGALK + 1.5*C3H8 +3.0*CH3COCH3 + 4.0*MEK + 1.0*C2H2 + 3.0*HYAC
ETH	C2H4
OLE	C3H6 + BIGENE
ISOP	ISOP
TERP	C10H16
TOL	0.3*TOLUENE
XYL	0.1*TOLUENE
SO2	SO2
NH3	NH3
BENZENE	0.6*TOLUENE

NR	C2H2 + 1.5*C3H8 + 0.5*TOLUENE + 0.3*BIGENE
CH4	CH4
POC	OC
PEC	BC
PMOTHR	PM25 – OC - BC
PMC	PM10 – PM25

Vertical allocation of fire emissions

The vertical fraction of FINN emissions is calculated on both pressure and smoke smoldering effect. The computed vertical layer fraction (LFRAC) for one model grid cell having the largest emission is shown in Figure 4. The fraction of emissions on the surface (Lay1F) is small (0.01) without considering the smoke smoldering effect. Pouliot et al. (2005) estimated the smoldering effect as:

$$BE_{size} = 0.0703 \times \ln(acres) + 0.3 \qquad (4)$$

$$S_{fract} = 1 - BE_{size} \qquad (5)$$

Where BE_{size} is buoyancy efficiency as a function of fire size, acres is fire size in the unit of acres, and S_{fract} the smoldering fraction. In the above example, the new Lay1F is 0.27, which is consistent with the values from Tai et al. (2008).

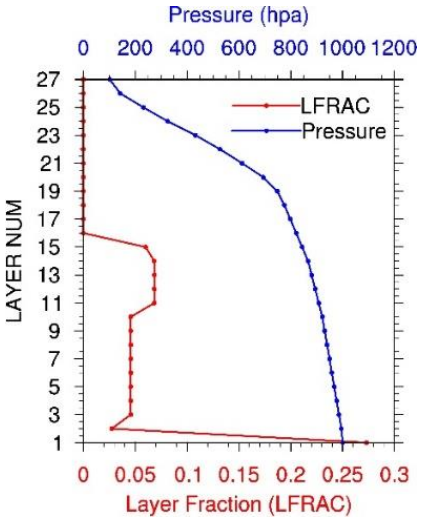

Figure 4: An example of vertical layer fraction (LFRAC) for one model grid cell with non-zero FINN emission.

Processing BEIS to obtain model-ready emissions

The Biogenic Emission Inventory System (BEIS) version 3.14 from EPA is used to create gridded, hourly emissions of VOCs and NO_x from vegetation and soils. The BEIS uses meteorological inputs including hourly temperature and shortwave downward radiation, which is internally

converted to photosynthetically activate radiation (PAR). PAR is the visible light fraction of shortwave downward radiation. The BEIS uses vegetation speciation data from the Biogenic Emissions Landuse Database version 3 (BELD3), which provides data on 230 land use and vegetation classes at 1 km resolution over the continental U.S. The BELD3 are based on combined county-level U.S. Department of Agriculture (USDA) agriculture data and U.S. Forest Service (USFS) Forest Inventory and Analysis (FIA) vegetation species data. The soil NO algorithm is a function of temperature, rainfall, and growing season (Yienger and Levy, 1995). Additional descriptions of BEIS algorithms are to be found in Pouliot and Pierce (2009).

One point in question is the motivation to use BEIS as compared to using the Model of Emissions of Gases from Nature (MEGAN). Our group actually did set up the MEGAN model and obtained preliminary emissions results using the same. However, previous studies have indicated that CMAQ simulations using MEGAN inputs have over-predicted concentrations of several species such as isoprene (e.g. Kota et al., 2015; Warneke et al., 2010) which resulted in large over-prediction of ozone. In order to clearly understand the effect of biomass burning, the base inventory needs to be accurate; hence we chose to go with BEIS.

Plume rise approaches

This study compared plume rise algorithms from two models. Here the Western Regional Air Partnership's (WRAP) plume model, and the Weather Research and Forecasting Chemistry's (WRF-Chem) online plume model are compared over a simulation episode in September 2013. We first used the WRAP model here for our model-measurement analyses because it is already employed by other researchers for CMAQ modeling exercise (e.g. Fu et al. 2012). To the best of our knowledge, no one has yet applied the WRF-Chem plume rise module for use in smoke emissions modeling of CMAQ.

In this study, plume top and bottom define a vertical zone within which the smoke begins to transport away from the source region, which is akin to the approach adopted by Raffuse et al. (2012). Smoke heights exhibit significant variability ranging from a few hundred meters to about 4.5 km above the terrain (Kahn et al., 2008). The terminal height of smoke depends on several factors including atmospheric static stability, amount of water vapor, wind speed and heat flux released by the fire (Freitas et al., 2007). On average, pyrogenic trace gases and aerosols in an unstable air mass can be lifted ~600 m higher than those in stable one (Val Martin et al., 2010). The latent heat from condensation of water vapor adds buoyancy to the lofted smoke (Penner et al., 1986). Strong horizontal wind speed causes greater entrainment, lowering plume height (Freitas et al., 2010) and bending the smoke. The smoke injection height determines smoke transport distance and direction. The model simulation indicated that higher smoke injection height produced larger downwind ozone enhancement (Leung et al., 2007). Therefore, an accurate plume rise model considering those physical processes is necessary to distribute fire emissions vertically in chemical transport models (CTMs).

Given the multiplicity and complexity of the dynamic evolution of BB plumes, a simplified approach in CTMs is to distribute fire emissions uniformly within the planetary boundary layer (Parrington et al., 2012) or below some altitude (Pfister et al., 2006). An empirical parameterization, the WRAP scheme (Tai et al., 2008; WRAP 2005), estimates the plume top and bottom as a function of the time of day and fire size. However, both of the two methods cannot realistically capture the variations of smoke plume rise. By analyzing stereographic plume heights for 2002 and 2004–2007 observed from the Terra Multi-angle Imaging SpectroRadiometer

(MISR), Val Martin et al. (2010) found that about 4–12% of fire plumes over North America reached the free troposphere. The WRAP scheme releases all nighttime fire emissions into the first model layer, which may lead to overestimation of ground level biomass burning emissions impacts near the fire source region. The BlueSky algorithm, another empirical plume rise model based on the Briggs equations (Briggs, 1975), was implemented into CMAQ. Although suitable for controlled fires, this model is not capable of predicting wildfire behaviors (Paugam et al., 2016) because it generally underestimates smoke injection heights compared with satellite measurements (Raffuse et al., 2012). Thus, in this study, we adopted the 1-D plume rise model developed by Freitas et al. (2007), which explicitly treats pyro-convection by solving equations of momentum (vertical motion), energy (the first law of thermodynamics), and mass balance (continuity) of water vapor iteratively. The model obtains environmental input conditions from the host model and returns estimated plume heights. We setup two different plume rise modules -- WRAP and 1-D plume rise modules. Below are detailed explanations of two modules. Again, for our biomass burning analysis, we implemented two different modules into the CMAQ simulations, evaluated both results and finally chose the 1-D plume rise module for this study.

Plume rise estimation using the WRAP model

In the WRAP model, fires are categorized into five classes (Table 2) based on burned virtual acreage. The virtual acreage is defined in Equation 6 (WRAP, 2005).

Table 2: Fire size classes.

Class	1	2	3	4	5
Virtual acres (a)	0–10	10 <a <100	100<a<1000	1000 <a<5000	≥5000

$$Acreage_{virtaul} = Acreage_{actual} \cdot \sqrt{\frac{Fuel\ Loading}{Normalizer}} \quad (6)$$

Where $Acreage_{actual}$ is the actual fire size in acres and $Normalizer$ equals 13.8 tons per acre.

Instead of using fuel loadings provided in the WRAP report which are assigned for western land-use/land-cover (LULC), fuel loadings for North America were converted from Wiedinmyer et al. (2011) and listed in Table 3. Using these numbers provided a more accurate representation of fuel loading for the inventory. Buoyancy efficiencies and fire related parameters for the WRAP module are addressed in Tables 4 and 5.

Table 3: Fuel loadings (tons/acre) assigned to North America land cover classifications used by FINN emission inventory.

Tropical Forest	Extra tropical Forest	Savanna	Grassland
113.62	42.46	3.95	3.95

Hourly plume top and bottom are calculated as follows:

$$p_{top_{hour}} = (BE_{hour})^2 \cdot (BE_{size})^2 \cdot p_{top_{max}}$$
$$p_{bot_{hour}} = (BE_{hour})^2 \cdot (BE_{size})^2 \cdot p_{bot_{max}} \quad (7)$$

Where BE_{hour} and BE_{size} are buoyancy efficiencies as a function of hour of day and fire size, respectively. The values and formulations follow in the tables and equations below, taken from WRAP (2005).

Table 4: Buoyancy efficiencies as a function of hour of day

Hour	1	2	3	4		5	6	7	8	9	10	11	12
BE_{hour}	0.03	0.03	0.03	0.03		0.03	0.03	0.03	0.03	0.06	0.1	0.2	0.4
Hour	13	14	15	16		17	18	19	20	21	22	23	24
BE_{hour}	0.7	0.8	0.9	0.95		0.99	0.8	0.7	0.4	0.06	0.03	0.03	0.03

Table 5: Fire-Related parameters as a function of fire size classes

Class	1	2	3	4	5
Virtual acres (a)	0–10	10 <a <100	100<a<1000	1000 <a<5000	≥5000
BE_{size}	0.4	0.6	0.75	0.85	0.90
$p_{top_{max}}$ (m)	160	2400	6400	7200	8000
$p_{bot_{max}}$ (m)	0	900	2200	3000	3000

Plume rise estimation using the 1-D WRF-Chem plume rise model

As described by Freitas et al. (2007), the water balance can be written as

$$\frac{\partial y}{\partial t} + w\frac{\partial w}{\partial z} = \frac{1}{1+\gamma} gB - \frac{2\alpha}{R_p} w^2 + \frac{\partial}{\partial z}\left(K_m \frac{\partial w}{\partial z}\right) \quad (8)$$

$$\frac{\partial T}{\partial t} + w\frac{\partial T}{\partial z} = -w\frac{g}{c_p} - \frac{2\alpha}{R_p}|w|(T - T_e) + \frac{\partial}{\partial z}\left(K_T \frac{\partial T}{\partial z}\right) + \left(\frac{\partial T}{\partial z}\right)_{microphysics} \quad (9)$$

$$\frac{\partial r_v}{\partial t} + w\frac{\partial r_v}{\partial z} = -\frac{2\alpha}{R_p}|w|\left(r_v - r_{v_e}\right) + \frac{\partial}{\partial z}\left(K_T \frac{\partial r_v}{\partial z}\right) + \left(\frac{\partial r_v}{\partial z}\right)_{microphysics} \quad (10)$$

$$\frac{\partial r_c}{\partial t} + w\frac{\partial r_c}{\partial z} = -\frac{2\alpha}{R_p}|w|r_c + \frac{\partial}{\partial z}\left(K_T \frac{\partial r_c}{\partial z}\right) + \left(\frac{\partial r_c}{\partial z}\right)_{microphysics} \quad (11)$$

$$\frac{\partial r_{ice,rain}}{\partial t} + w\frac{\partial r_{ice,rain}}{\partial t} = -\frac{2\alpha}{R_p}|w|r_{ice,rain} + \frac{\partial}{\partial z}\left(K_T \frac{\partial r_{ice,rain}}{\partial z}\right) + \left(\frac{\partial r_{ice,rain}}{\partial z}\right)_{microphysics} + sedim_{ice,rain} \quad (12)$$

Where $w, T, r_v, r_c, r_{rain},$ and r_{ice} are the vertical velocity, air temperature, water vapor, and cloud, rain and ice mixing ratios, respectively, which are associated with in-cloud air parcels. Freitas et al. (2007) report that "[e]ntrainment of environmental air is taken to be proportional to the vertical velocity in the cloud, and the entrainment coefficient is based on the traditional formulation $\frac{2\alpha}{R_p}$ where R_p stands for the radius of the plume and α =0.1." In our Eq. (8) γ = 0.5; it is a term introduced to offset exclusion of non-hydrostatic pressure perturbations (Simpson and Wiggert, 1969), g is acceleration due to gravity and B is the buoyancy term related to the temperature difference between the in-cloud air parcel and its surrounding environment and includes the downward drag of condensate water. In Eqs. (9) and (10), the index e indicates the value refers to the surrounding environment, while c_p represents specific heat at constant pressure. K_m and K_T

are the eddy coefficients for the diffusivity of momentum and heat, respectively. They are based on the Smagorinsky (1963) scheme and include corrections for the influence of the Brunt-Vaisala frequency (Hill, 1974) and Richardson number (Lilly, 1962).

The lower boundary condition is based on a virtual source of buoyancy placed below the model surface (Turner, 1973; Latham, 1994). The buoyancy generated by this source is obtained from the convective energy flux E and the plume radius:

$$F = \frac{gR}{c_p p_e} E R_p^2 \qquad (13)$$

Where R is the ideal gas constant and p_e is the ambient surface pressure. Once the buoyancy flux is determined, it provides the vertical velocity (w_0) and the temperature excess ($T_0 - T_{e,0}$) for the air parcels at the surface according to Morton et al. (1956) and Latham (1994).

$$w_0 = \frac{5}{6\alpha}\left(\frac{0.9\alpha F}{z_v}\right)^{1/3} \qquad (14)$$

$$\frac{\Delta\rho_0}{\Delta_{\rho e,0}} = \frac{5}{6\alpha}\frac{F}{g}\frac{{z_v}^{-5/3}}{(0.9\alpha F)^{1/3}} \qquad (15)$$

$$T_0 = \frac{T_{e,0}}{1-\frac{\Delta\rho_0}{\Delta_{\rho e,0}}} \qquad (16)$$

Figure 5 plots the modeled plume height rise from both approaches. The results indicate that the WRAP approach is unable to capture the diurnal variation of the plume rise height. In other words, the WRAP modeled plume rise height shows no residual height during the nighttime. It is understood that physically, the fire emissions rise a finite, non-zero height during the nighttime. The 1-D WRF-Chem plume rise approach captures this physical trend quite well.

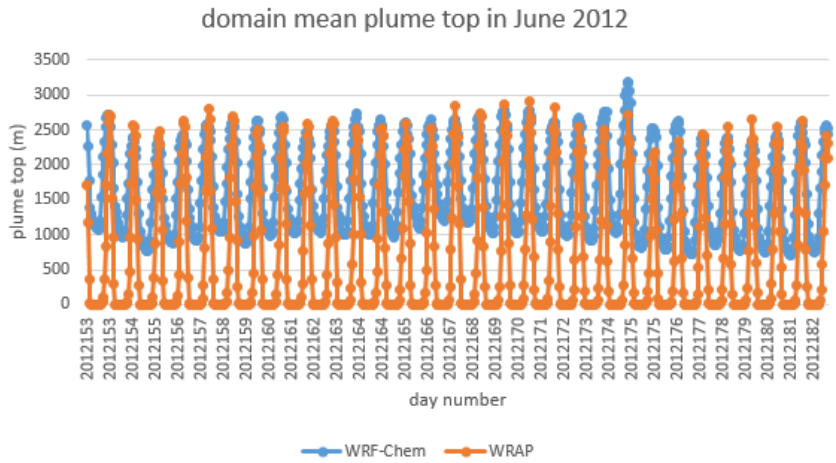

Figure 5: Diurnal variation of domain-average plume rise height using the WARP and 1-D WRF-Chem plume rise approaches in June 2012.

Simulation domain, episode and input fields

The WRF and CMAQ simulation period is selected to be April-Oct in 2012, 2013 and 2014.

The meteorological model, WRF

Domain setup

The WRF and CMAQ domains have sizes of 470×310 and 459×299 for 12-km domain, respectively. The geographic parameters and vertical layers for the domains are listed in Table 6 and Table 7, respectively.

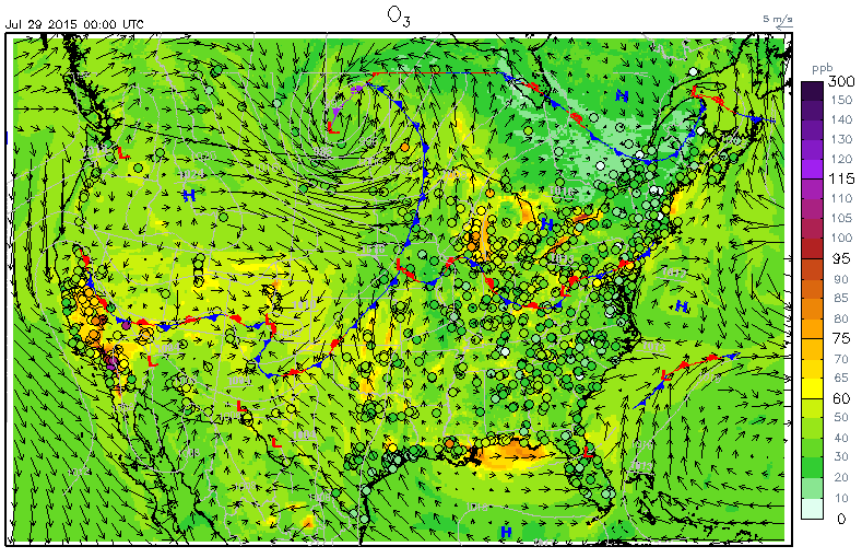

Figure 6: CMAQ used for the UH Air Quality Forecasting (AQF) System at University of Houston (http://spock.geosc.uh.edu).

Table 6: Projection Parameters and Domain Origin

First True Latitude (Alpha)	33°N
Second True Latitude (Beta)	45°N
Central Longitude (Gamma)	-97°W
Projection Origin	(31.55113°N, -98.13650°W)
12km WRF domain Lower Left Corner [x, y] (m)	[-1007980, -1739860]

Both WRF and CMAQ share the same vertical structure since no layer collapsing has been employed in MCIP. The vertical structure is listed in Table 7.

Table 7: Vertical layer structures of WRF and CMAQ used for the modeling

Layer	**AGL(m)**
1	15.85
2	55.48
3	101.18
4	175.06
5	271.50
6	401.34

7	606.83
8	943.06
9	1421.18
10	1966.39
11	3200.86
12	5167.92
13	7268.67
14	10062.33
15	13477.36

Input analysis data

We have evaluated existing analysis datasets and decided to use NCEP's (National Centers for Environmental Prediction) NARR (North American Regional Reanalysis) as input. The NARR data are based on an NCEP Eta 221 regional North American grid (Lambert Conformal) (see: http://www.nco.ncep.noaa.gov/pmb/docs/on388/tableb.html) at 29 pressure levels. Its horizontal resolution is 32-km and the frequency is 3-hourly. An alternative to NARR is the Eta-NAM analysis data. However, data frequency is reduced from every three hours to every six hours starting in 2013. Our validation tests showed it is not as good as NARR for WRF input, probably because of lower temporal resolution.

Major WRF configurations

Implemented WRF options are shown in Table 8 below. First guess and boundary conditions will be from NCEP NARR analyses. Grid nudging is turned on with the same NARR analysis data.

Table 8: WRF physics options

WRF Version	V3.6.1
Microphysics	Lin et al. Scheme
Long-wave Radiation	RRTMG
Short-wave Radiation	New Goddard scheme
Surface Layer Option	Monin-Obukhov with CB viscous sublayer scheme
Land-Surface Option	Unified Noah LSM
Urban Physics	None
Boundary Layer	YSU
Cumulus Cloud Option	Kain-Fritsch
FDDA	Grid and 1-hr observation-nudging

Grid Nudging

Data assimilation is an effective method which could enhance accuracy of air quality simulations. The effect of improved meteorological input fields using this technique on successful air quality simulations has been reported by various previous studies. Grid nudging technique is a simple, but

efficient, method of data assimilation that can improve atmospheric fields (Bowden et al., 2012). Rresearch has demonstrated the benefit of grid nudging to air quality modeling studies (Liu et al., 2012; Otte, 2008a, 2008b). The grid nudging method adds artificial tendency terms to the prognostic equations of variables to correct the original model values toward analysis values in initial data.

Emission processing using SMOKE

Emission modeling was performed with the Sparse Matrix Operator Kernel Emissions (SMOKE) model. The 2011 National Emission Inventory (2011 NEI) generated by the EPA (Souri et al., 2016; Diao et al., 2016a, 2016b) was used to estimate hourly emission rates from anthropogenic sources for the continental U.S. Emissions from natural sources were estimated with BEIS3 (Biogenic Emission Inventory System version 3; additional details at http://www.epa.gov/ttn/chief/conference/ei11/modeling/vukovich.pdf). Mobile emissions were processed with MOVES. Various surface NO_x emissions were prepared for inverse modeling. Again, in this project, we used the latest 2011 NEI emissions "as is", that is, without adjusting for possible emission changes. A brief summary of the emissions data used in this emissions modeling platform follows:

- 2011 platform v6.1 represents all platform sectors (area, nonroad, and so on) other than onroad mobile sources;
- For onroad mobile source emissions, the latest 2011 platform v6.2 based on the latest Motor Vehicle Emissions Simulator (MOVES) 2014 was used.

Table 9 lists sectors that we used to represent the year 2011 air pollutant emissions for this emission modeling system and notes on data preparation.

Table 9: Platform sectors for the 2011 NEI platform.

Platform Sector	Abbreviation	Description
EGU non-peaking units	Ptegu	2011 NEI point source EGUs determined to operate as non-peaking units. Hourly 2011 CEMS are not used since the year of modeling is 2012-2014.
EGU peaking units	ptegu_pk	Same as ptegu sector but limited to EGUs that are determined to operate as peaking units. Hourly 2011 CEMS are not used since the year of modeling is 2012-2014.
Point source oil and gas	pt_oilgas	2011NEIv1 point sources with oil and gas production emissions processes. Annual resolution.
Remaining non-EGU point	Ptnonipm	All 2011NEIv1 point source records not matched to the ptegu, ptegu_pk, and pt_oilgas sectors, except for offshore point sources that are in the "othpt" sector. Includes all aircraft emissions and some rail yard emissions. Annual resolution.
Agricultural	Ag	NH_3 emissions from 2011NEIv1 nonpoint livestock and fertilizer application, county and annual resolution.
Area fugitive dust	Afdust	PM_{10} and $PM_{2.5}$ from fugitive dust sources from the 2011NEIv1 nonpoint inventory including building construction, road construction, and agricultural dust, and road dust. County and annual resolution.

Nonpoint oil and gas	np_oilgas	2011NEIv1 nonpoint sources from oil and gas-related processes. County and annual resolution.
Residential Wood Combustion	Rwc	This is a new sector in 2011NEIv1. NEI nonpoint sources with Residential Wood Combustion (RWC) processes. County and annual resolution.
Class 1 & 2 CMV and locomotives	c1c2rail	Locomotives and primarily category 1 (C1) and category 2 (C2) commercial marine vessel (CMV) emissions sources from the 2011NEIv1 nonpoint inventory. Midwestern states' CMV emissions, including Class 3 sources, are from a separate year 2010 emissions inventory. County and annual resolution.
Commercial marine	c3marine	Category 3 (C3) CMV emissions projected to 2011 from year 2002 values. These emissions are not from the 2011NEIv1, but rather were developed for the rule called "Control of Emissions from New Marine Compression-Ignition Engines at or Above 30 Liters per Cylinder", usually described as the Emissions Control Area- International Maritime Organization (ECA-IMO) study: http://www.epa.gov/otaq/oceanvessels.htm. (EPA-420-F-10-041, August 2010). U.S. states-only emissions (zero in Midwest); see othpt sector for all non-U.S. emissions. Treated as point sources to reflect shipping lanes, annual resolution.
Remaining nonpoint	nonpt	2011NEIv1 nonpoint sources not otherwise removed from modeling or included in other platform sectors; county and annual resolution.
Nonroad	nonroad	2011NEIv1 nonroad equipment emissions developed with the National Mobile Inventory Model (NMIM) using NONROAD2008 version NR08a. NMIM was used for all states except California and Texas, which submitted their own emissions to the 2011NEIv1. County and monthly resolution.
Onroad RatePerDistance	Rateperdistance	EPA ran MOVES2014 for 2011 in emissions factor mode. The MOVES lookup tables include on-network (RatePerHour) to represent exhaust and most evaporative emissions during running, tirewear, and brakewear modes. These data include the reference county and reference fuel month assignments that EPA used for the MOVES simulation.
Onroad RatePerHour	Rateperhour	EPA ran MOVES2014 for 2011 in emissions factor mode. The MOVES lookup tables include off-network (RatePerDistance) that represents emissions from extended idling and APU operation. These data include the reference county and reference fuel month assignments that EPA used for the MOVES simulation.
Onroad RatePerVehicle	Ratepervehicle	EPA ran MOVES2014 for 2011 in emissions factor mode. The MOVES lookup tables include off-network starts/stops (RatePerVehicle) that represents emissions from start exhaust and most evaporative emissions that occurs off-network. These data include the reference county and reference fuel month assignments that EPA used for the MOVES simulation.

Onroad RatePerProfile	Rateperprofile	EPA ran MOVES2014 for 2011 in emissions factor mode. The MOVES lookup tables include off-network (RatePerProfile) that represents emissions from evaporative fuel vapor venting. These data include the reference county and reference fuel month assignments that EPA used for the MOVES simulation.
Non-US Point	Othpt	Point sources from Canada's 2006 inventory and Mexico's Phase III 2012 inventory, annual resolution. Mexico's inventory is year 2012 and grown from year 1999 (ERG, 2009; Wolf, 2009). Also includes all non-U.S. C3 CMV and U.S. offshore oil production, which are unchanged from the 2008 NEI point source annual emissions.
Non-US nonpoint and nonroad	Other	Annual year 2006 Canada (province resolution) and year 2012 (grown from 1999) Mexico Phase III (municipio resolution) nonpoint and nonroad mobile inventories.
Non-US onroad	Othon	Year 2006 Canada (province resolution) and year 2012 (grown from 1999) Mexico Phase III (municipio resolution) onroad mobile inventories, annual resolution.
Biogenic	Biog	No updates made (Stay constant)

As a QA/QC check, we provide area sector comparison of the two inventories below. Figure 7 shows area emissions from 2008 NEI and 2011 NEI over southeast Texas, as well as differences in percentage. The reduction is evident – the 2008 NEI large area emission in the DFW area (left corner) can hardly be seen in the 2011 NEI (in the middle). Intensity also decreased in the Houston area.

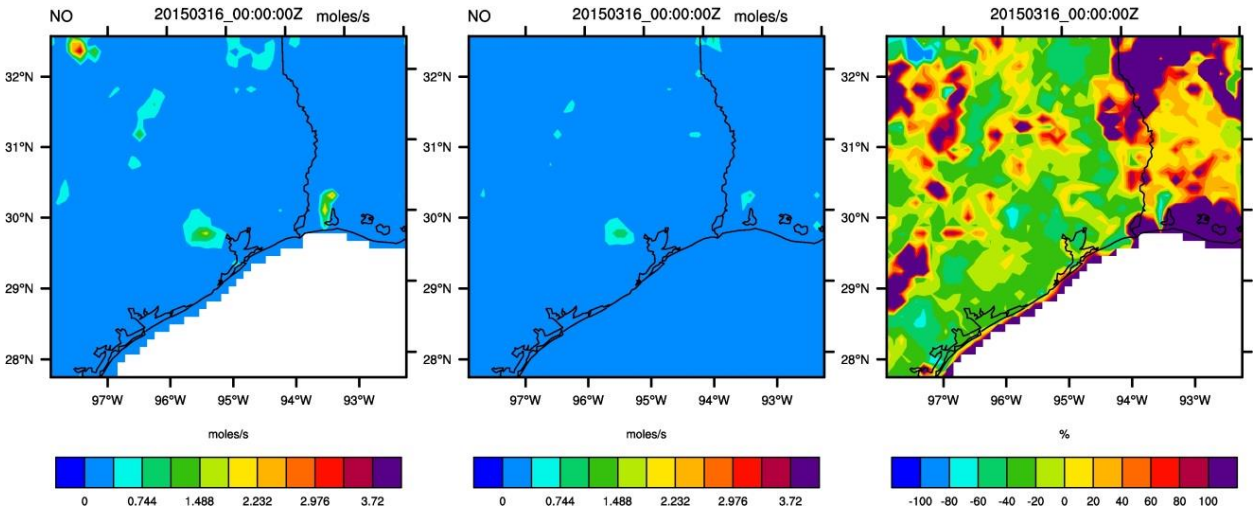

Figure 7: Area emissions. Left: 2008 NEI, center: 2011 NEI, and right: difference in percent.

The chemical transport model, CMAQ

Major CMAQ configurations are shown in Table 10. All of these options have been tested by the UH modeling group.

Table 10: Major CMAQ options

CMAQ version	V5.0.1
Chemical Mechanism	CB05 gas-phase mechanism with active chlorine chemistry, updated toluene mechanism, fifth-generation CMAQ aerosol mechanism with sea salt, aqueous/cloud chemistry
Lightning NOx emission	Included by using inline code
Horizontal advection	YAMO
Vertical advection	WRF omega formula
Horizontal mixing/diffusion	Multiscale (multiscale)
Vertical mixing/diffusion	Asymmetric Convective Model version 2
Chemistry solver	EBI optimized for the Carbon Bond-05 mechanism
Aerosol	AERO 5 for sea salt and thermodynamics
Cloud Option	ACM cloud processor for AERO5
IC/BC source	Default static profiles

Dynamic chemical boundary conditions

One of the drawbacks of the standard CMAQ model is the fact that it uses temporally static boundary conditions, implying that the concentrations of model species over the model grid cells do not exhibit any diurnal variation. This could potentially bias model-measurement comparisons, especially at grid cells near the model lateral and upper boundary. In order to mitigate this potential source of model-measurement error, we used input boundary conditions simulated by a global Chemical Transport Model (CTM). In this space, we ran the GEOS-Chem model (Bey et al., 2001) for the years of 2011 to 2014 to generate 3-D gridded species concentrations over a lateral grid ($2^o \times 2.5^o$ GEOS-Chem spatial resolution regridded for the new CMAQ chemical boundary conditions) over the continental U.S. An additional advantage of using GEOS-Chem is that it has 47 vertical profiles stretching from the surface to about 80 km, which makes it possible to provide vertical boundary conditions over a larger height. This could help simulate long-range transport of ozone from wildfires and capture stratospheric impact on surface ozone.

Model evaluation

Evaluation of model output in terms of chemistry and biomass burning impact

In this section, we evaluated the performance of CMAQ model output to various observations in different regions of U.S. Next, the impact of biomass burning on air quality was investigated. On average, there was one big fire in the U.S every month. The regions that our evaluation will be

focused on are depicted in Figure 8. We divided our simulation into spring (April-May), summer (June-August), and fall (September-October) seasons.

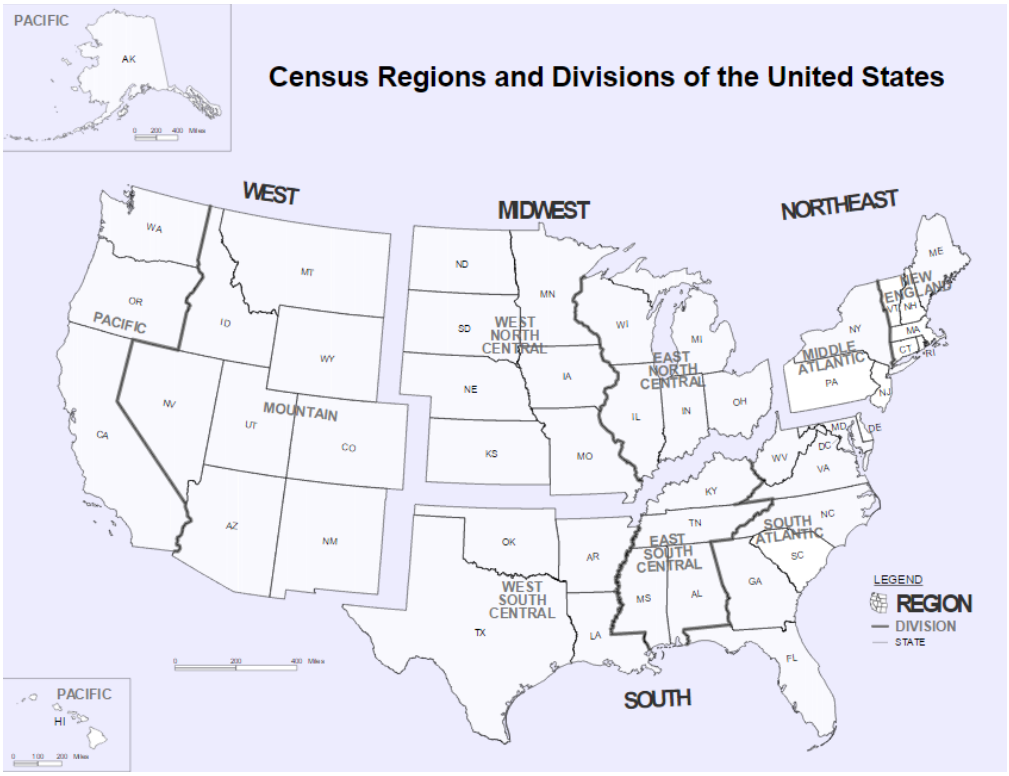

Figure 8: U.S. Census Bureau Regions and Divisions (http://www2.census.gov/geo/pdfs/maps-data/maps/reference/us_regdiv.pdf).

As indicated previously, we ran two simulation scenarios: one with biomass burning added in and the other without biomass burning emissions. In order to capture the impact of biomass burning on air quality, we investigated the difference of model output with biomass burning emissions and without considering them. This can be represented as:

Impact of biomass burning = CMAQ(2011 NEI +biomass) - CMAQ(2011 NEI)

We will focus on ozone, $PM_{2.5}$ and CO in this report.

Evaluation metrics

To evaluate performance of CMAQ simulations we used the following statistics. All are frequently used in the modeling community. Observational EPA AQS data, often referred to as "in situ" data, were used to validate model results.

Correlation (r) between model values and observed values

$$r = \frac{\sum_{t=1}^{n}[(x_t - \bar{x})(y_t - \bar{y})]}{\sqrt{\sum_{t=1}^{n}(x_t - \bar{x})^2 * \sum_{t=1}^{n}(y_t - \bar{y})^2}} \qquad (17)$$

n = number of data points (i.e., number of monitors), x = observed values, y = model values, values with an over bar indicate the mean.

Index of Agreement (IOA) between model values and observed values

$$IOA = 1 - \frac{\sum_{t=1}^{n} {e_t}^2}{\sum_{t=1}^{n}(|y_t - \bar{x}| + |x_t - \bar{x}|)^2} \quad (18)$$

n = number of data points, $e_t = y_t - x_t$, x = observed values, y = model values, values with an over bar indicate the mean.

Root Mean Square Error (RMSE)

$$RMSE = \sqrt{\frac{1}{n}\sum_{t=1}^{n} {e_t}^2} \quad (19)$$

n = number of data points, $e_t = y_t - x_t$, x = observed values, y = model values.

Mean Absolute Error (MAE)

$$MAE = \frac{1}{n}\sum_{t=1}^{n} |e_t| \quad (20)$$

n = number of data points, $e_t = y_t - x_t$, x = observed values, y = model values.

Mean Bias (MB)

$$MB = \frac{1}{n}\sum_{t=1}^{n} e_t \quad (21)$$

n = number of data points, $e_t = y_t - x_t$, x = observed values, y = model values.

Model-measurement evaluation

Ozone model-measurement comparisons and biomass burning impacts for 2012

The contour maps which contrast CMAQ model results for 12-hr average ozone concentrations against in-situ data for the ozone season of 2012 are plotted in Figures 9-15. The model maps which report absolute concentrations include the impact of biomass emissions, and the difference maps represent the difference between the biomass emissions and non-biomass emissions case, unless stated otherwise.

A comparison for the month of April 2012 is plotted in Figure 9, which includes the impact of biomass emissions. Broadly, the model does a good job of capturing the ozone hotspots over the western Mountain region. An increase of 0.5-1 ppb is predicted across the eastern U.S. due to biomass burning.

The model-measurement comparison for the month of May, 2012 is plotted in Figure 10. In-situ data show several hotspots having ozone concentrations exceeding 70 ppb over the western mountain region extending into southern California. Additionally, there are a couple of hotspots over Ohio and Pennsylvania in the northeast with ozone concentrations around 60 ppb. The model does a good job of capturing these hotspots. The biomass impact plot indicates that a change of

~0.5-1 ppb is predicted all across the U.S. except for the western coast states of California, Oregon and Washington. Also, a change of 1-2 ppb is predicted across northern Mexico.

Figure 11 plots the model-measurement comparison for June 2012. There are several 60-70 ppb hotspots in the Western Mountain, Midwest, East North Central and Northeastern Regions, which the model captures quite well. However, it is unable to capture the hotspots higher than 70 ppb which are observed in Central California. A broadly similar story is told by the comparison for July 2012 in Figure 12. The impact plots indicate that biomass fires added ~ 1 ppb of ozone in northern Mexico in June, and more than 3 ppb in southern Canada, with a 1 ppb impact extending over a large region there.

In the comparison for August 2012 in Figure 13, hotspots are seen in the Western Mountains and California, reproduced quite well by the model. The forest fires in Idaho and California added 1-3 ppb ozone in these areas, with a 1-ppb impact crossing state borders.

In the comparison for September 2012 in Figure 14, it is noticed that the measured ozone concentrations on average were low (30-40 ppb) across the continental U.S., except for California. Surprisingly, the model over-predicts most of the low ozone across the country but under-predicts the high ozone in California.

The October 2012 comparison in Figure 15 indicates low ozone concentrations again across the country except for a few places in California and the Western Mountain regions. The model captures both spatial trends quite well.

Time series comparisons for the state of Texas are plotted in Figures 16-18. The plots indicate that the comparisons for the state of Texas are very similar in spring and fall, with a bit more over-prediction in summer. Overall, the model-measurement comparison demonstrates a very good correlation across all seasons, indicating that the model is able to capture the spatio-temporal trends of the in-situ data.

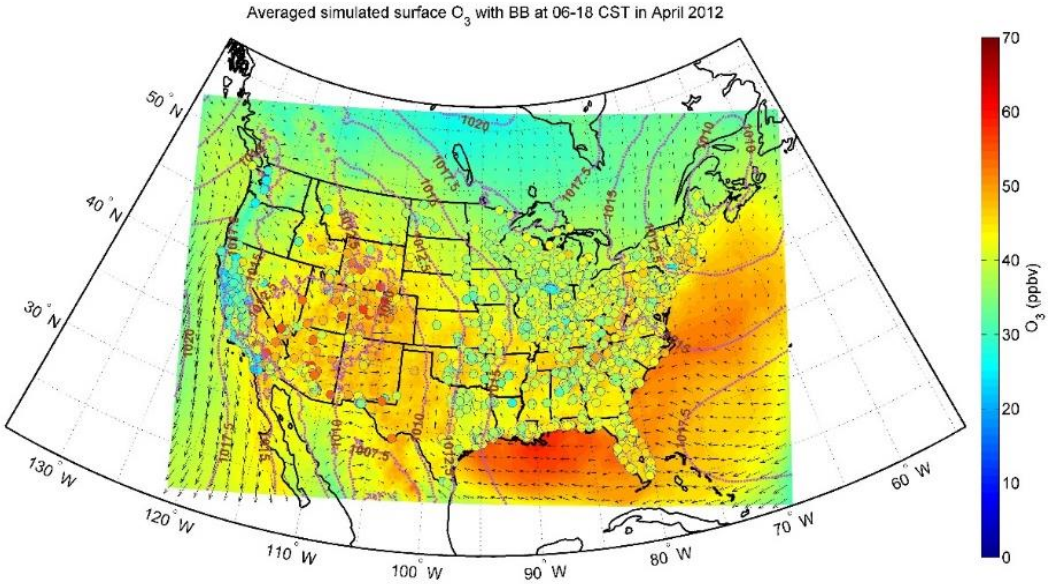

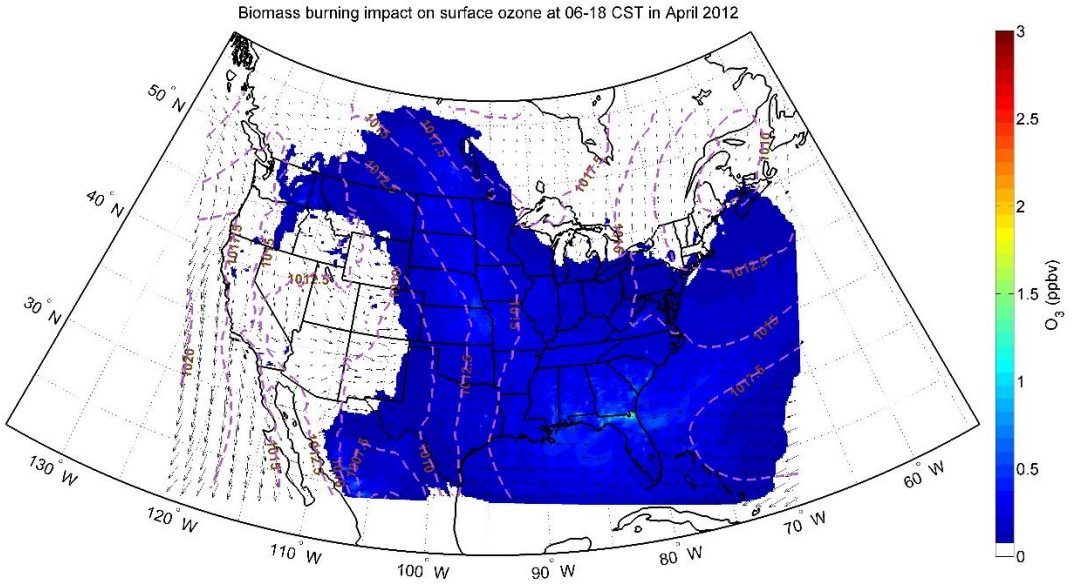

Figure 9: Ozone model-measurement comparison and biomass burning impacts for the month of April, 2012. Top panel plots the ozone concentrations with biomass burning emissions included. In-situ data are represented by circles in the top panel. The bottom panel plots the differences between the biomass case and the non-biomass one.

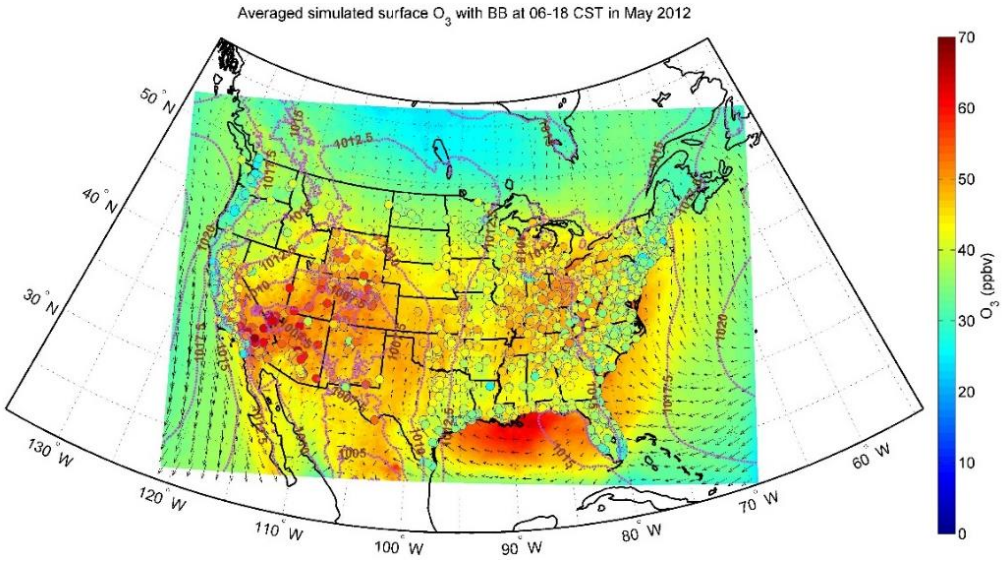

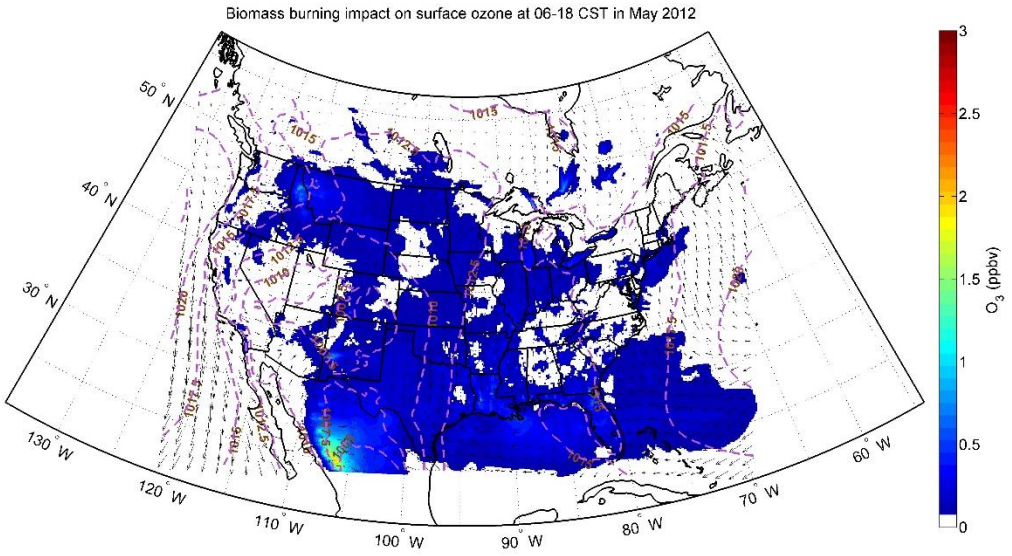

Figure 10: Ozone model-measurement comparison and biomass burning impacts for the month of May, 2012. Top panel plots the ozone concentrations with biomass burning emissions included. In-situ data are represented by circles in the top panel. The bottom panel plots the differences between the biomass case and the non-biomass one.

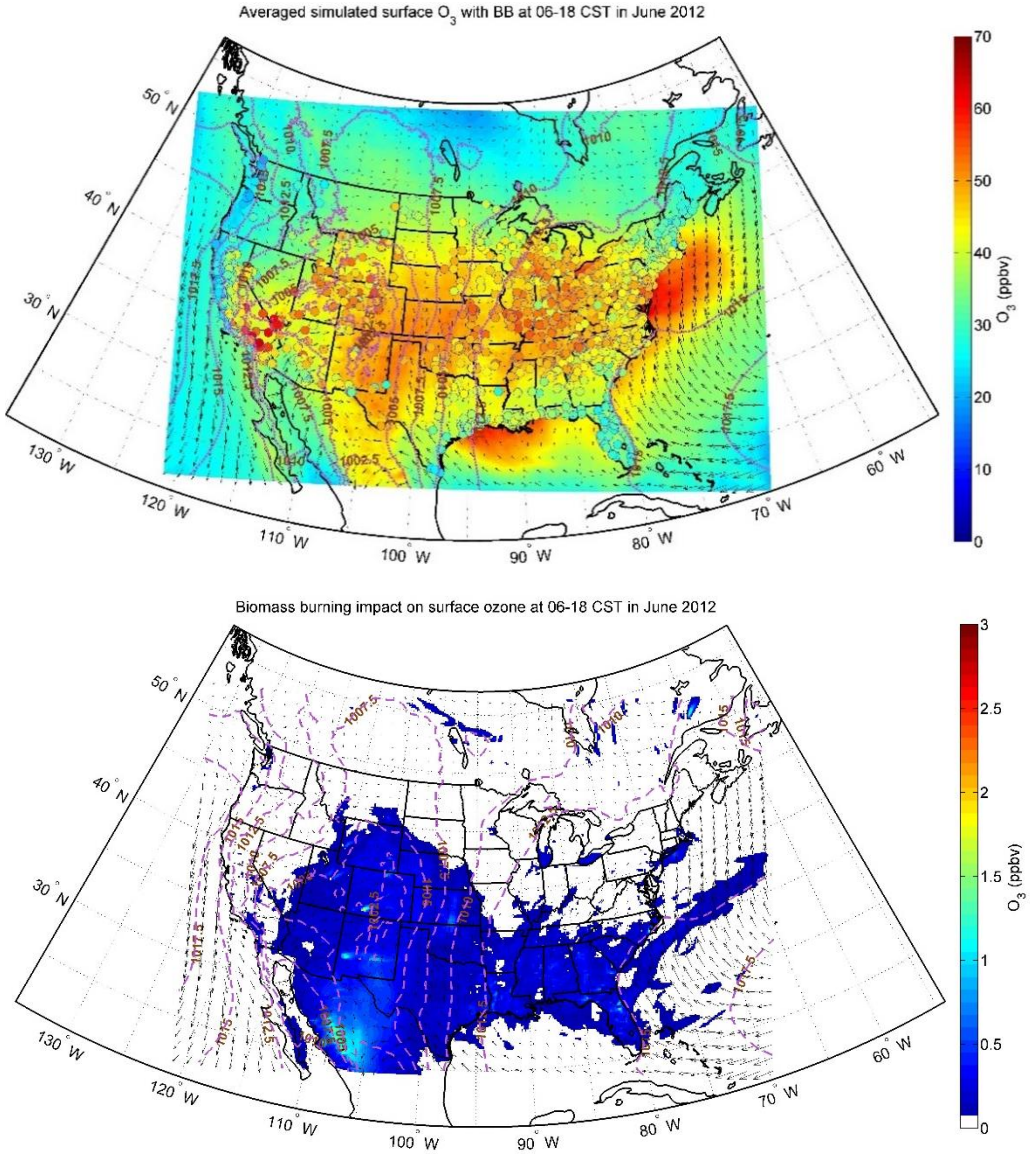

Figure 11: Ozone model-measurement comparison and biomass burning impacts for the month of June, 2012. Top panel plots the ozone concentrations with biomass burning emissions included. In-situ data are represented by circles in the top panel. The bottom panel plots the differences between the biomass case and the non-biomass one.

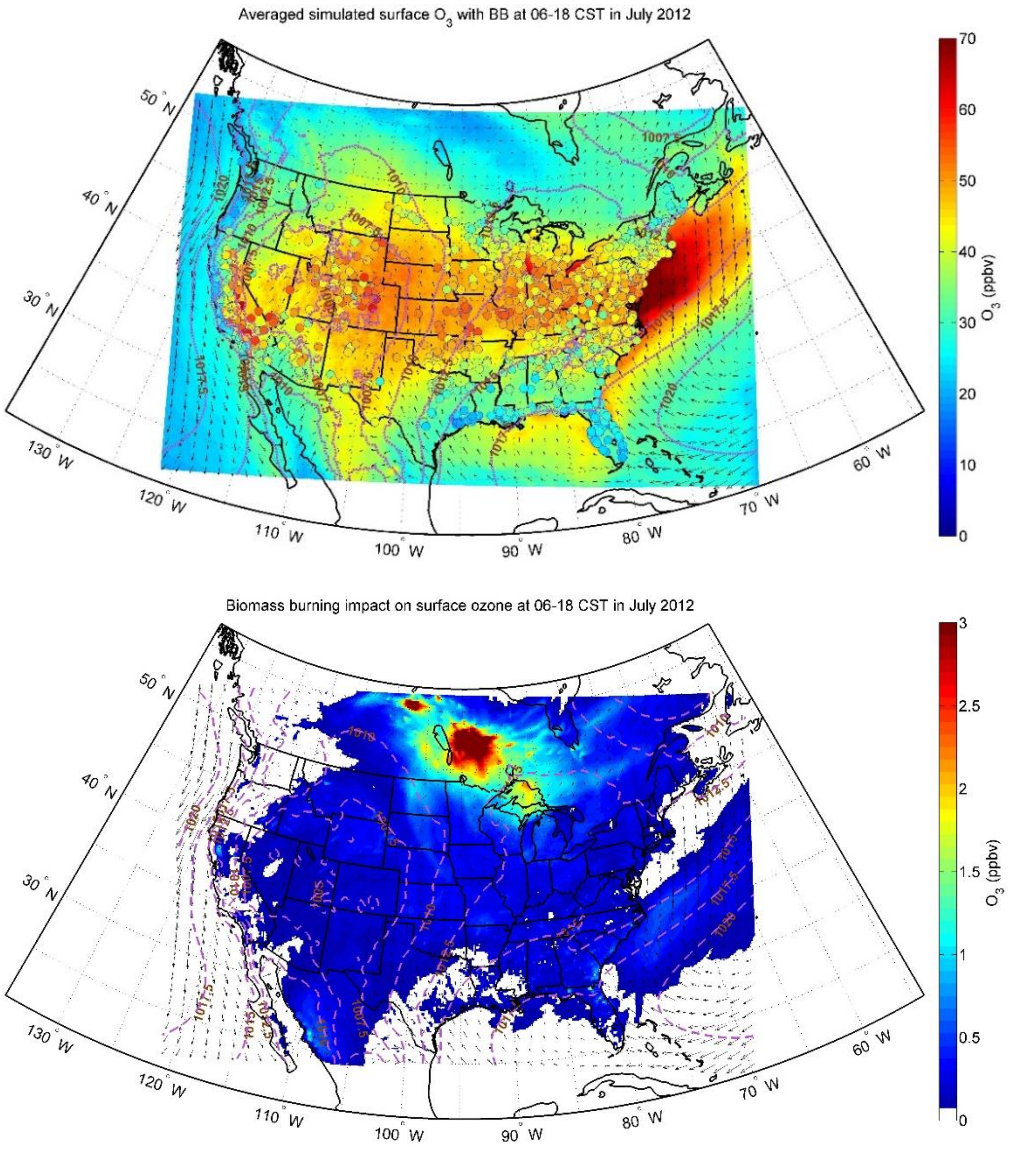

Figure 12: Ozone model-measurement comparison and biomass burning impacts for the month of July, 2012. Top panel plots the ozone concentrations with biomass burning emissions included. In-situ data are represented by circles in the top panel. The bottom panel plots the differences between the biomass case and the non-biomass one.

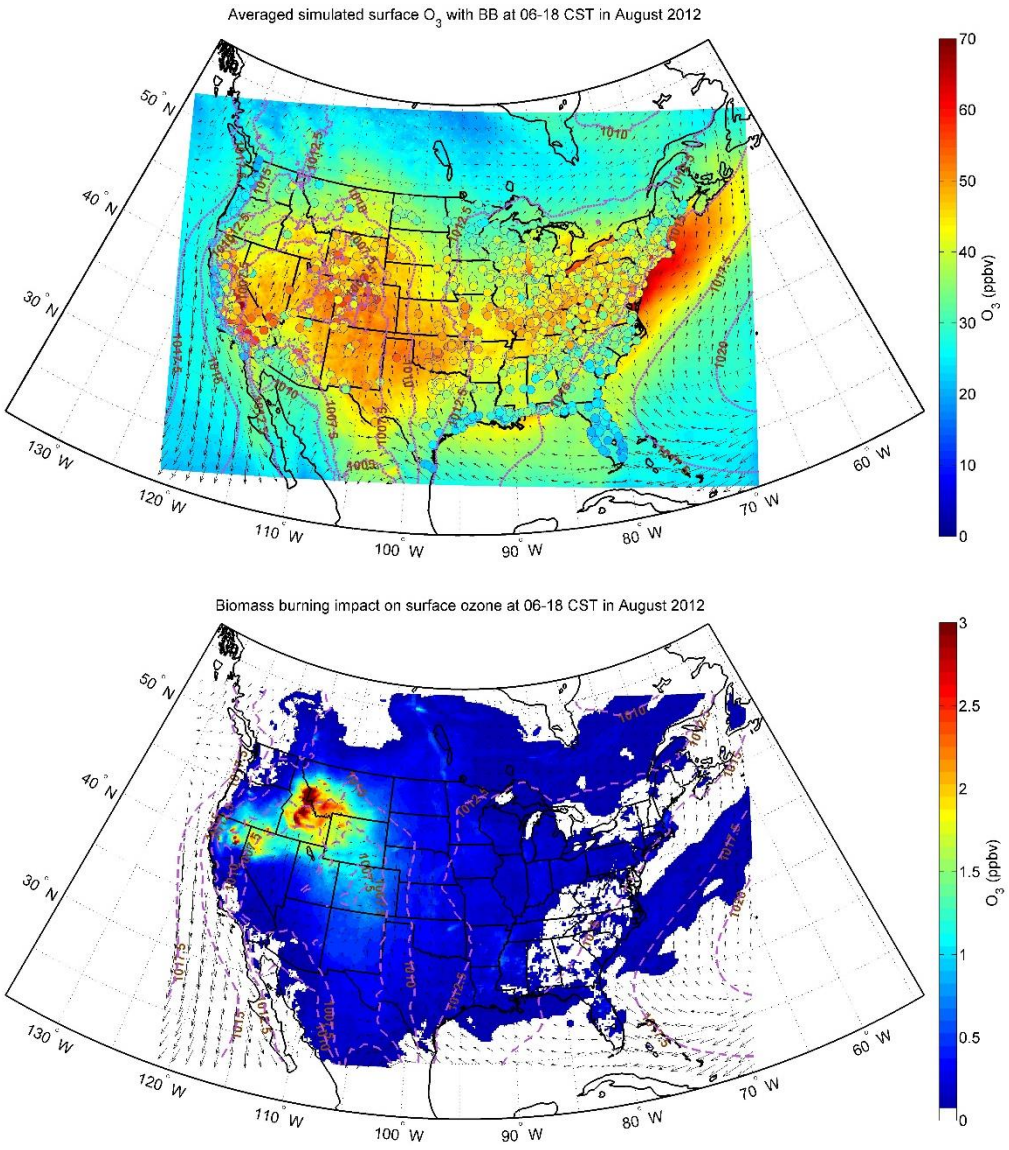

Figure 13: Ozone model-measurement comparison and biomass burning impacts for the month of August, 2012. Top panel plots the ozone concentrations with biomass burning emissions included. In-situ data are represented by circles in the top panel. The bottom panel plots the differences between the biomass case and the non-biomass one.

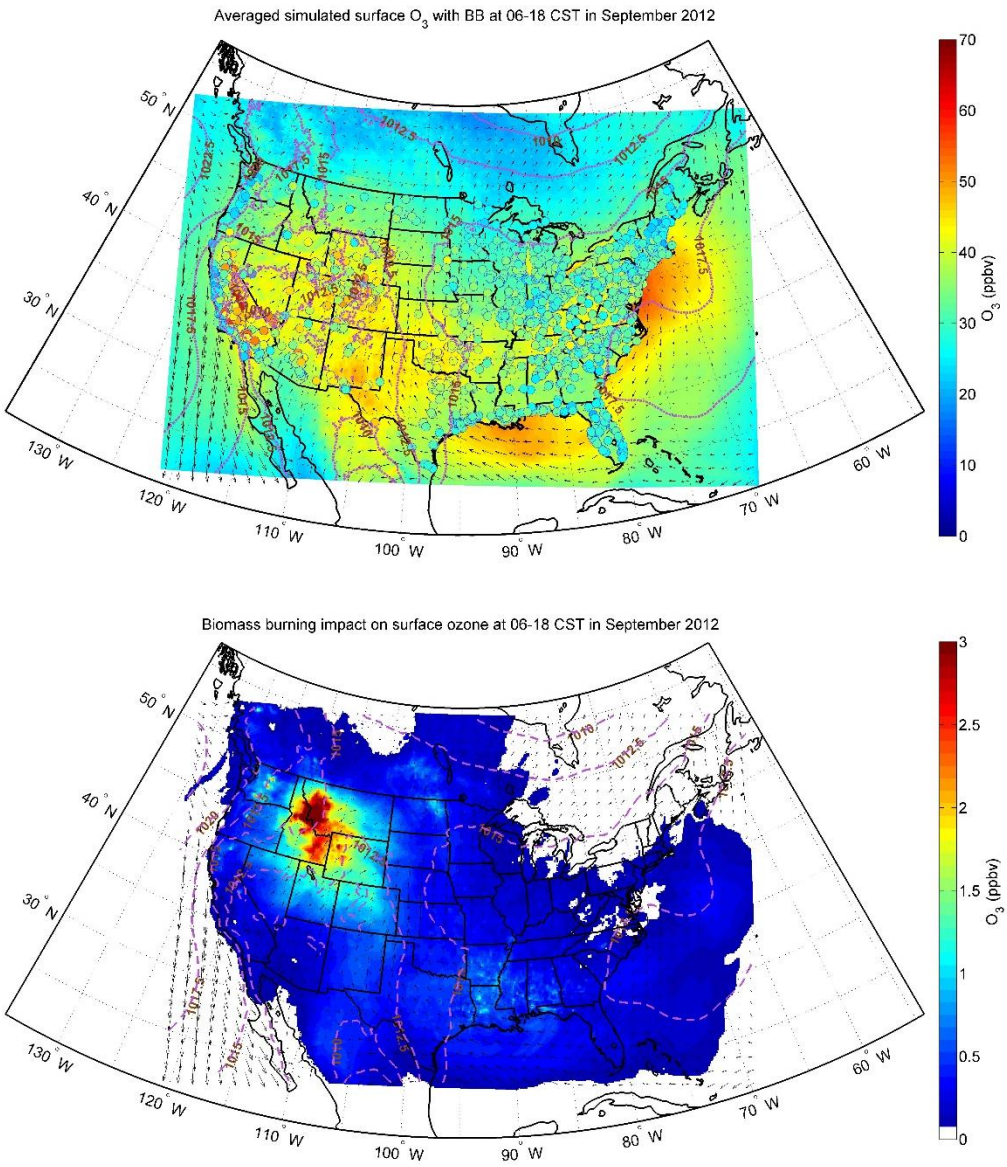

Figure 14: Ozone model-measurement comparison and biomass burning impacts for the month of September, 2012. Top panel plots the ozone concentrations with biomass burning emissions included. In-situ data are represented by circles in the top panel. The bottom panel plots the differences between the biomass case and the non-biomass one.

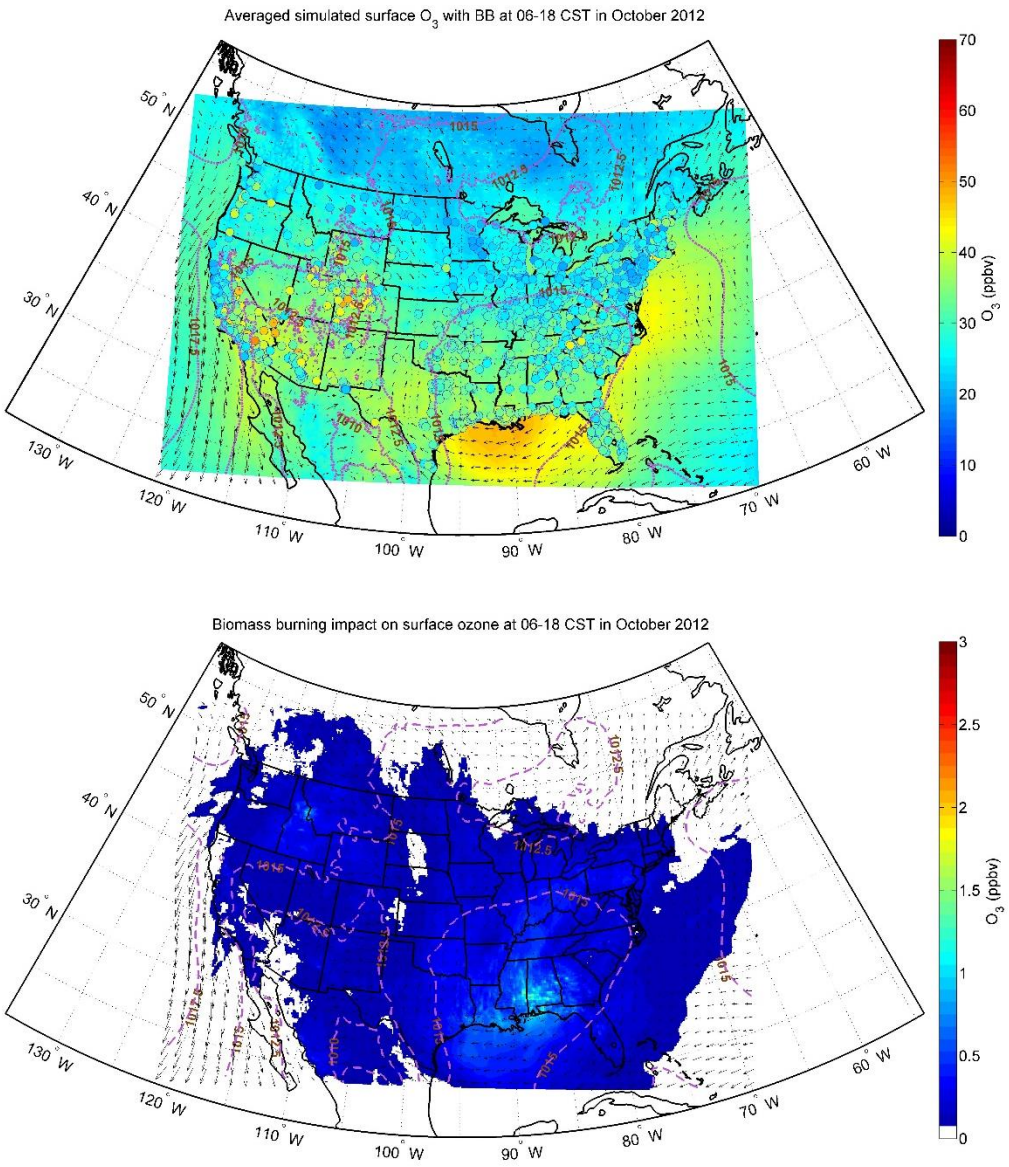

Figure 15: Ozone model-measurement comparison and biomass burning impacts for the month of October, 2012. Top panel plots the ozone concentrations with biomass burning emissions included. In-situ data are represented by circles in the top panel. The bottom panel plots the differences between the biomass case and the non-biomass one.

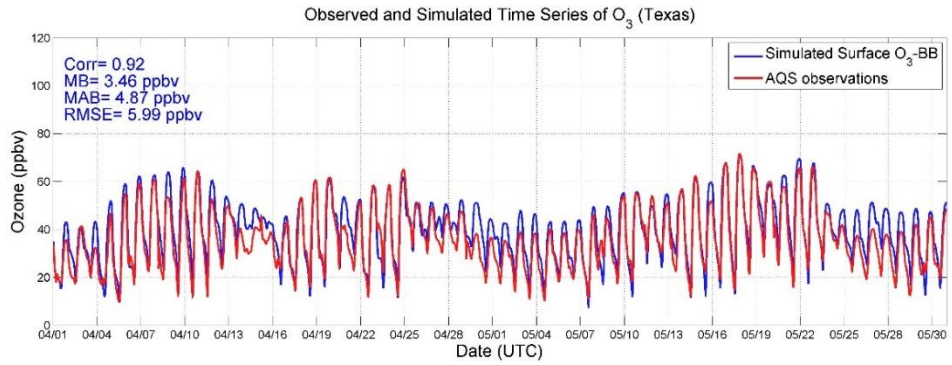

Figure 16: Ozone time series for model-measurement comparison during spring 2012 for the state of Texas.

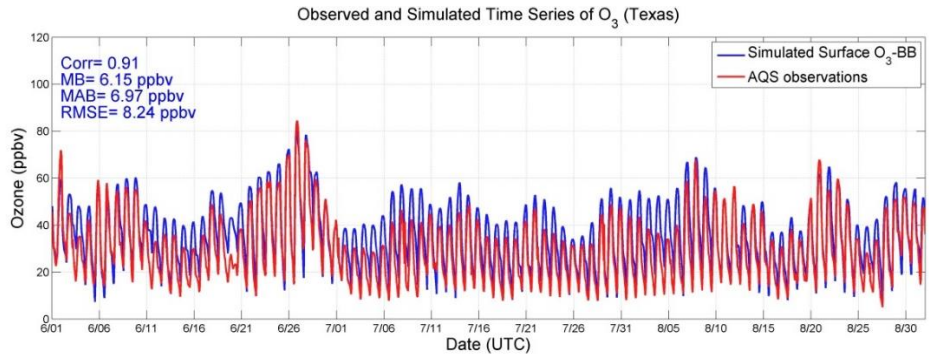

Figure 17: Ozone time series for model-measurement comparison during summer 2012 for the state of Texas.

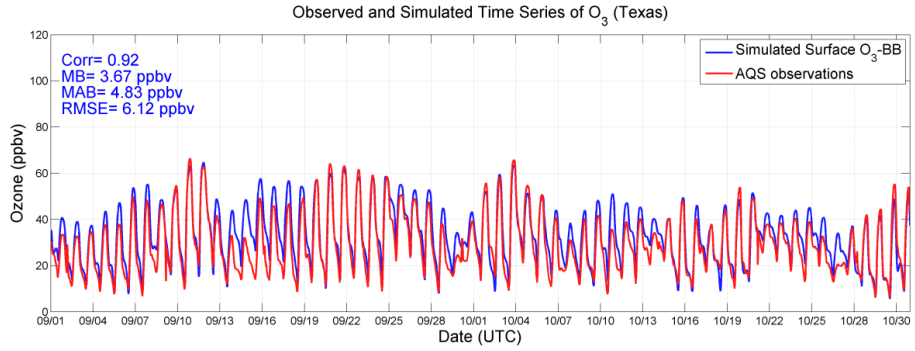

Figure 18: Ozone time series for model-measurement comparison during fall 2012 for the state of Texas.

PM2.5 model-measurement comparisons and biomass burning impacts for 2012

The $PM_{2.5}$ concentrations reported here are daily/episide averages. Figure 19 plots the CMAQ output contrasted with in-situ data for the month of April 2012. The in-situ data indicate concentrations of 10-12 $\mu g\ m^{-3}$ all across the eastern U.S., including southeastern Texas. Additionally, there are a couple of places in Georgia, New Mexico and California where the in-situ $PM_{2.5}$ concentration is greater than 20 $\mu g\ m^{-3}$. The model underpredicts in most of these places but is broadly able to capture the spatial vaiations across the eastern U.S. However, it is unable to capture the extreme events that result in $PM_{2.5}$ concentrations greater than 20 $\mu g\ m^{-3}$. Biomass burning caused changes of 1 $\mu g\ m^{-3}$ across the southeastern U.S. for this month.

The model-measurement comparison for the month of May, 2012 is plotted in Figure 20. In-situ data indicate several hotspots in Indiana, Arkansas, Texas, Louisiana and California, with concentrations ranging from 14-20 $\mu g\ m^{-3}$. The model predictions in these regions range from 10-12 $\mu g\ m^{-3}$, indicating a significant underprediction. Biomass burning caused a 1 $\mu g\ m^{-3}$ change across the southeast, and also in certain parts of northern Mexico and Idaho.

Similar trends are seen in the model-measurement comparison for the months of June, July and August 2012 as plotted in Figures 21, 22 and 23 respectively; although it must be noted that the in-situ concentrations over the eastern U.S. for July are 4-6 $\mu g\ m^{-3}$ higher than the other months. Figures 24 and 25 plot comparisons for the fall months of September and October. In addition to elevated concentrations over the eastern U.S., the in-situ data also report high concentrations over the states of Idaho and Washington, possibly attributed to forest fires. Although the model is unable to capture the magnitudes (resulting in underprediction), it is still able to reproduce the spatial trends. Biomass emissions changed $PM_{2.5}$ concentrations by 1 $\mu g\ m^{-3}$ across a significant portion of the southern U.S. in June; while those in July changed $PM_{2.5}$ concentrations by ~ 1 $\mu g\ m^{-3}$ across the eastern half of the U.S., with larger impacts of 5-10 $\mu g\ m^{-3}$ predicted in southeastern Canada. The August impact indicated a 1 $\mu g\ m^{-3}$ change across the western half of the U.S., with larger impacts up to 10 $\mu g\ m^{-3}$ predicted at the border of Idaho and Wyoming. Similar results are predicted for September 2012. The October predictions show changes of 1 $\mu g\ m^{-3}$ across most of the eastern half of the U.S. and in Idaho and Wyoming, with larger impacts of ~ 4 $\mu g\ m^{-3}$ in Louisiana and Mississipi.

The time series comparison for the state of Texas in spring, summer and fall is plotted in Figures 26, 27 and 28 respectively. Each of the figures shows a relatively poorer correlation, with fall being the best at 0.48 (note: the performance of $PM_{2.5}$ in the chemical transport model is generally worse than that of ozone). The significant underprediction for spring and summer is evident in the negative mean biases.

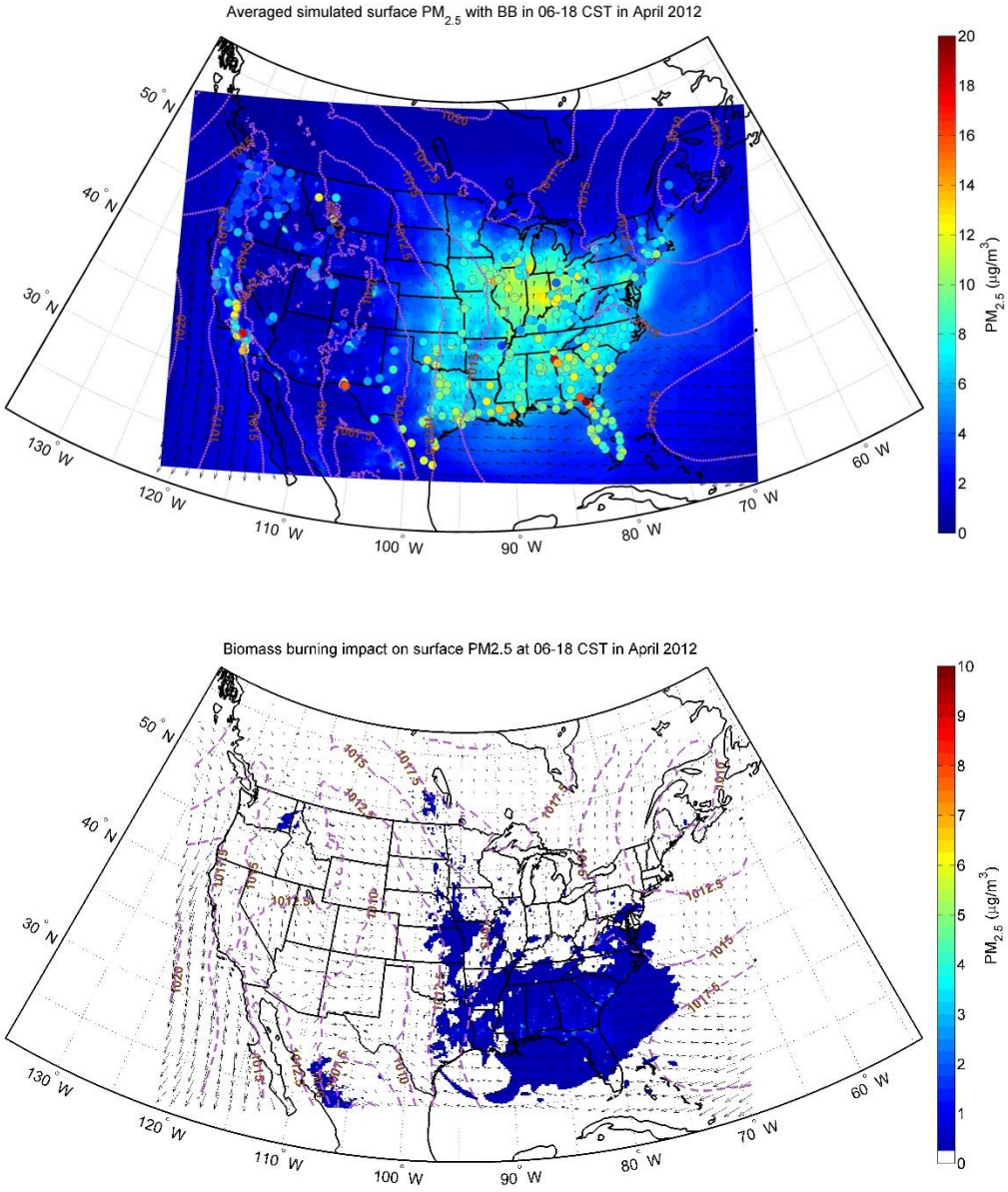

Figure 19: $PM_{2.5}$ model-measurement comparison and biomass burning impacts for the month of April, 2012. Top panel plots the ozone concentrations with biomass burning emissions included. In-situ data are represented by circles in the top panel. The bottom panel plots the differences between the biomass case and the non-biomass one.

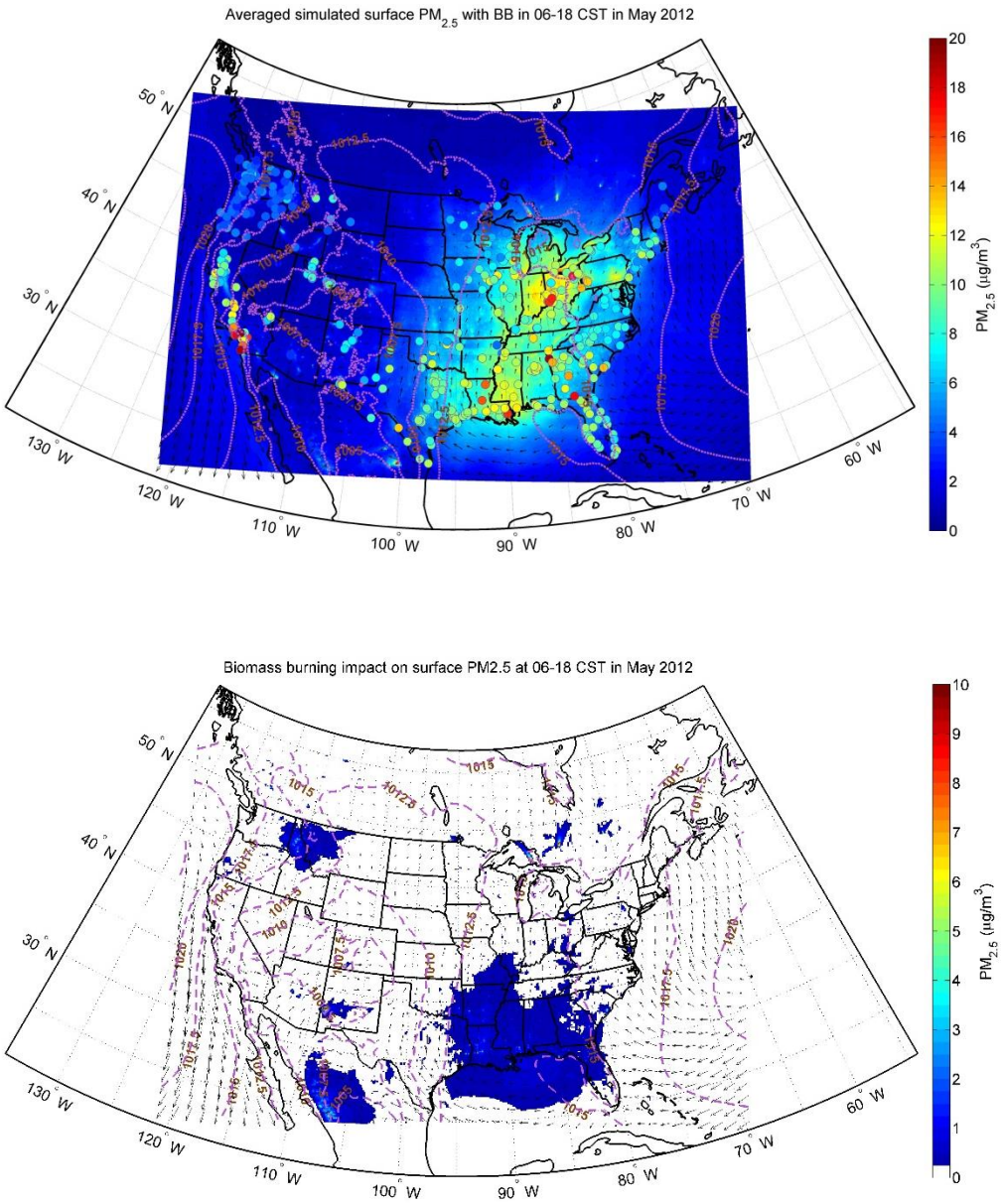

Figure 20: $PM_{2.5}$ model-measurement comparison and biomass burning impacts for the month of May, 2012. Top panel plots the ozone concentrations with biomass burning emissions included. In-situ data are represented by circles in the top panel. The bottom panel plots the differences between the biomass case and the non-biomass one.

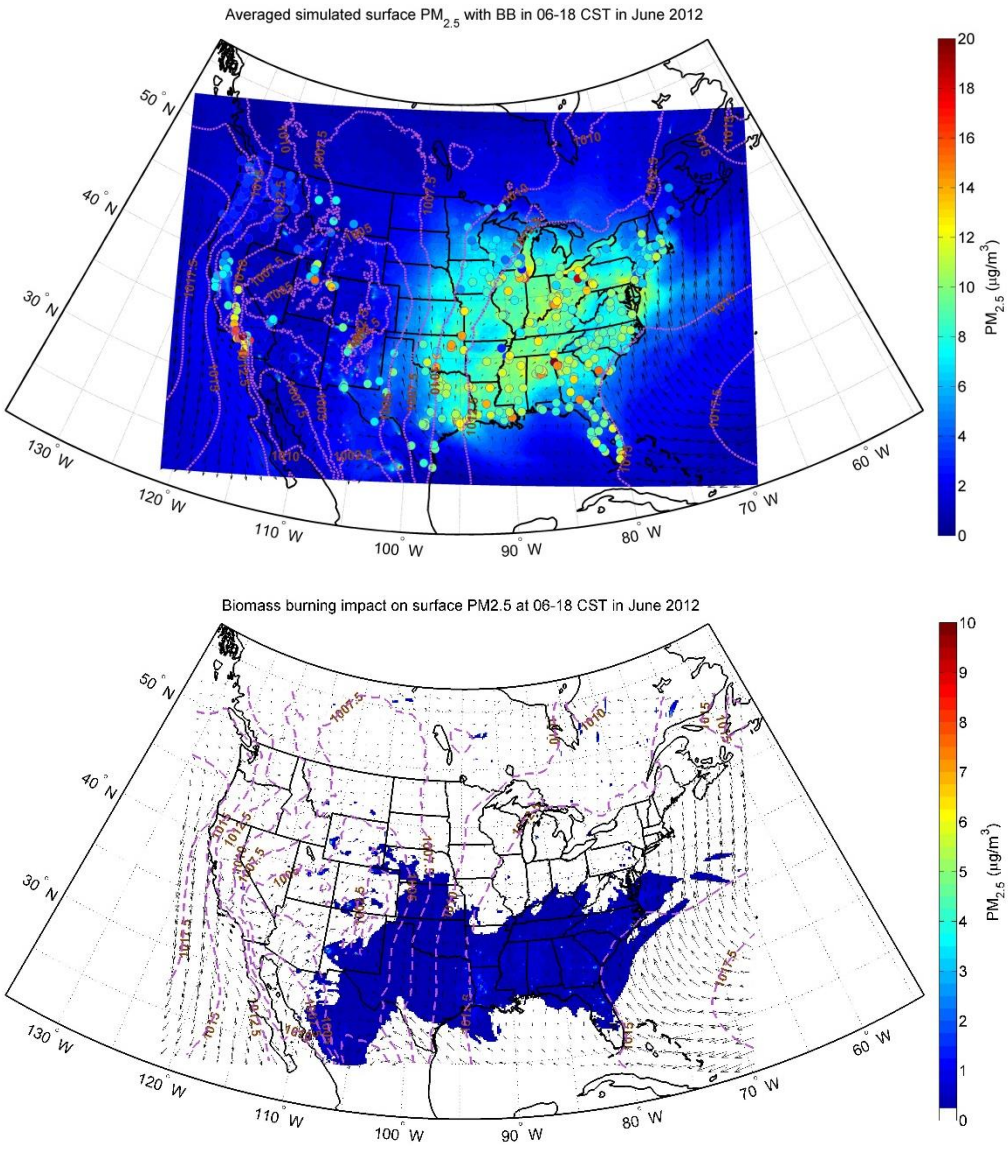

Figure 21: $PM_{2.5}$ model-measurement comparison and biomass burning impacts for the month of June, 2012. Top panel plots the ozone concentrations with biomass burning emissions included. In-situ data are represented by circles in the top panel. The bottom panel plots the differences between the biomass case and the non-biomass one.

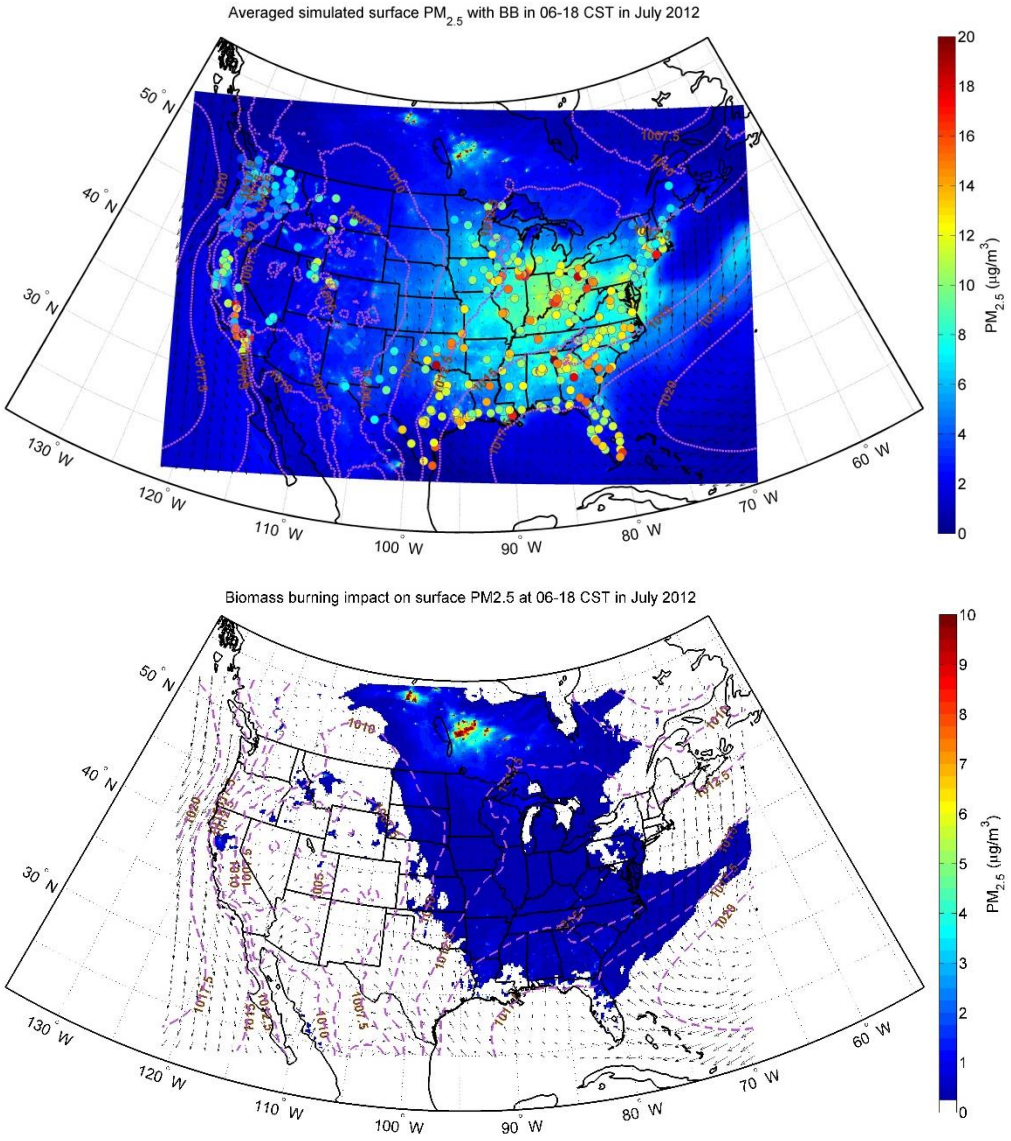

Figure 22: $PM_{2.5}$ model-measurement comparison and biomass burning impacts for the month of July, 2012. Top panel plots the ozone concentrations with biomass burning emissions included. In-situ data are represented by circles in the top panel. The bottom panel plots the differences between the biomass case and the non-biomass one.

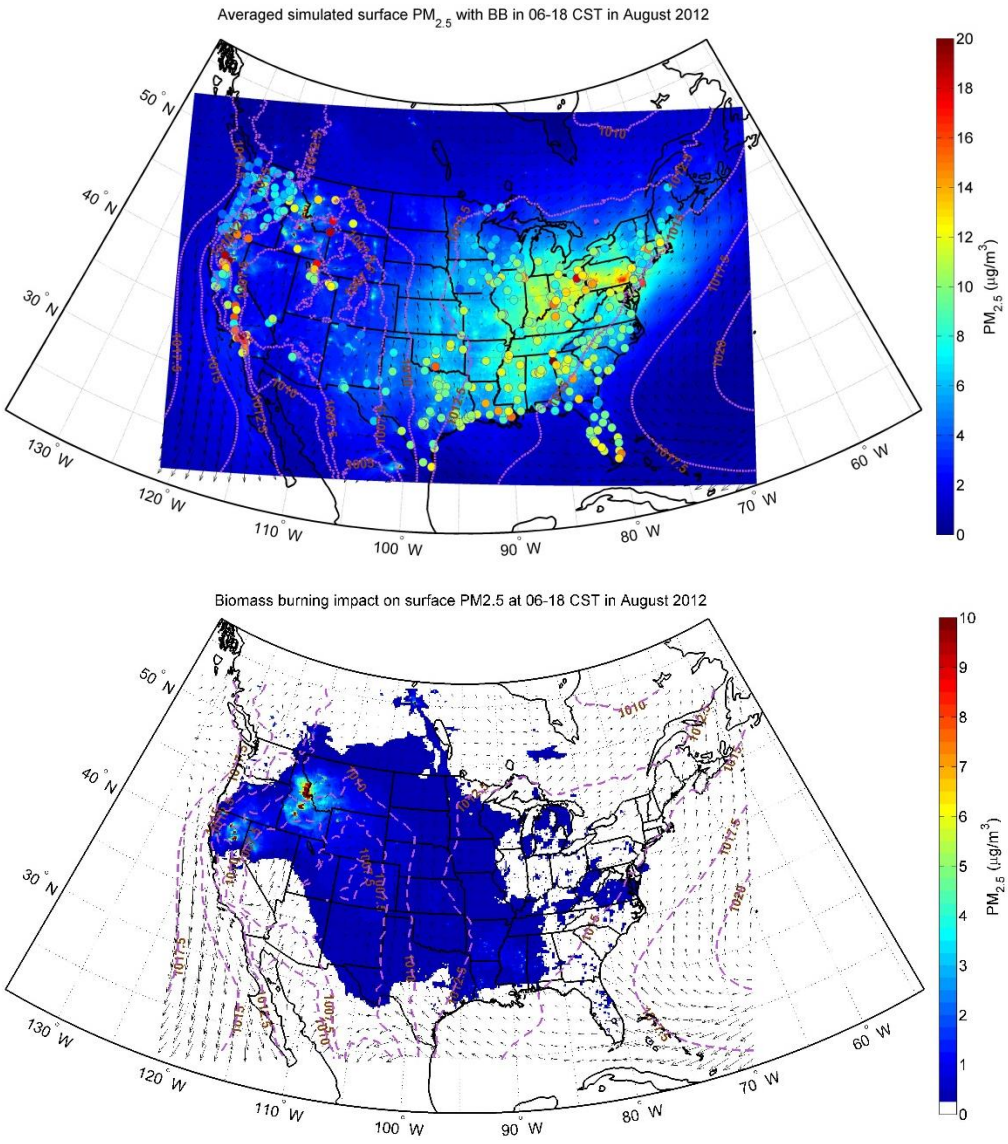

Figure 23: $PM_{2.5}$ model-measurement comparison and biomass burning impacts for the month of August, 2012. Top panel plots the ozone concentrations with biomass burning emissions included. In-situ data are represented by circles in the top panel. The bottom panel plots the differences between the biomass case and the non-biomass one.

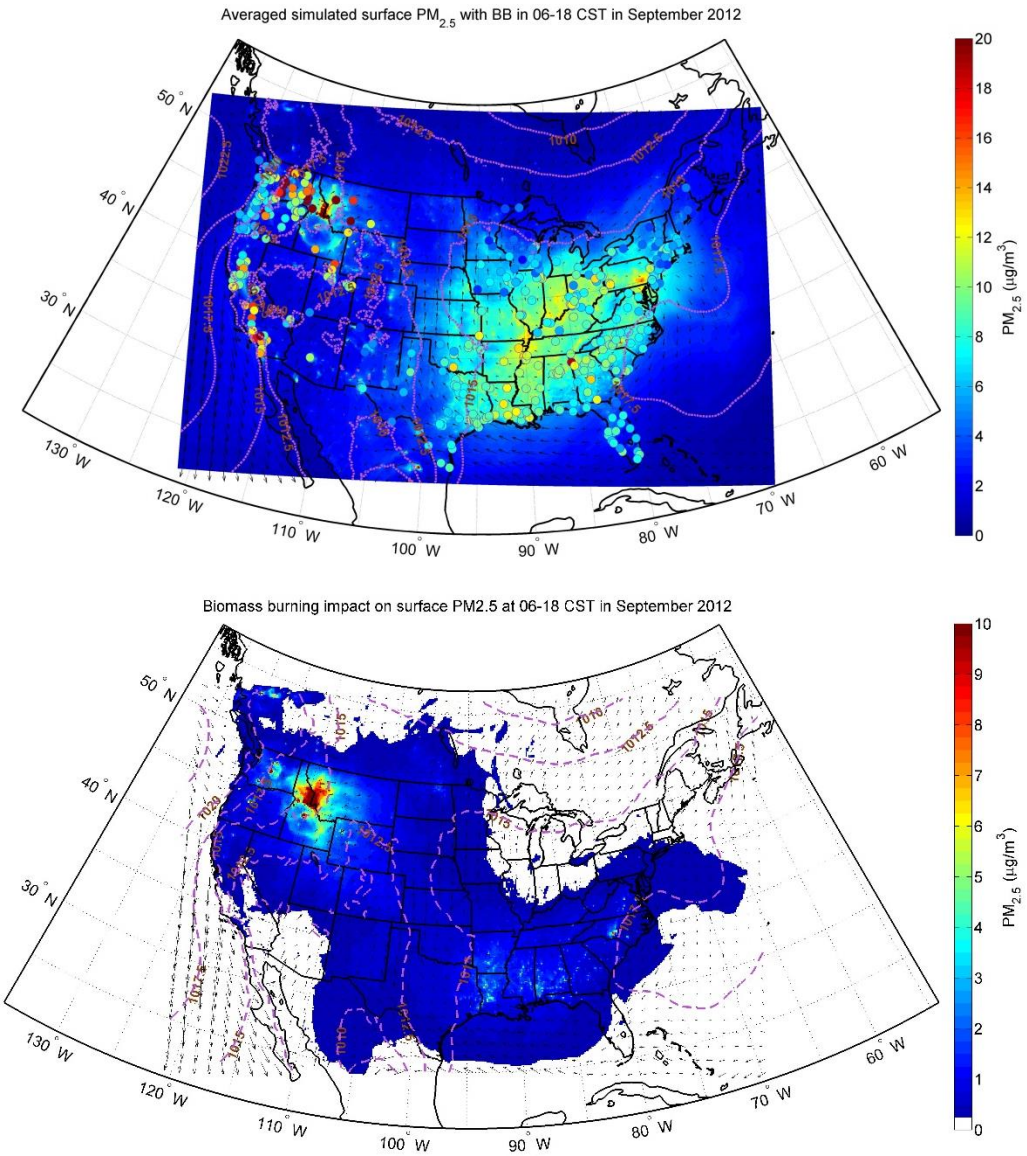

Figure 24: $PM_{2.5}$ model-measurement comparison and biomass burning impacts for the month of September, 2012. Top panel plots the ozone concentrations with biomass burning emissions included. In-situ data are represented by circles in the top panel. The bottom panel plots the differences between the biomass case and the non-biomass one.

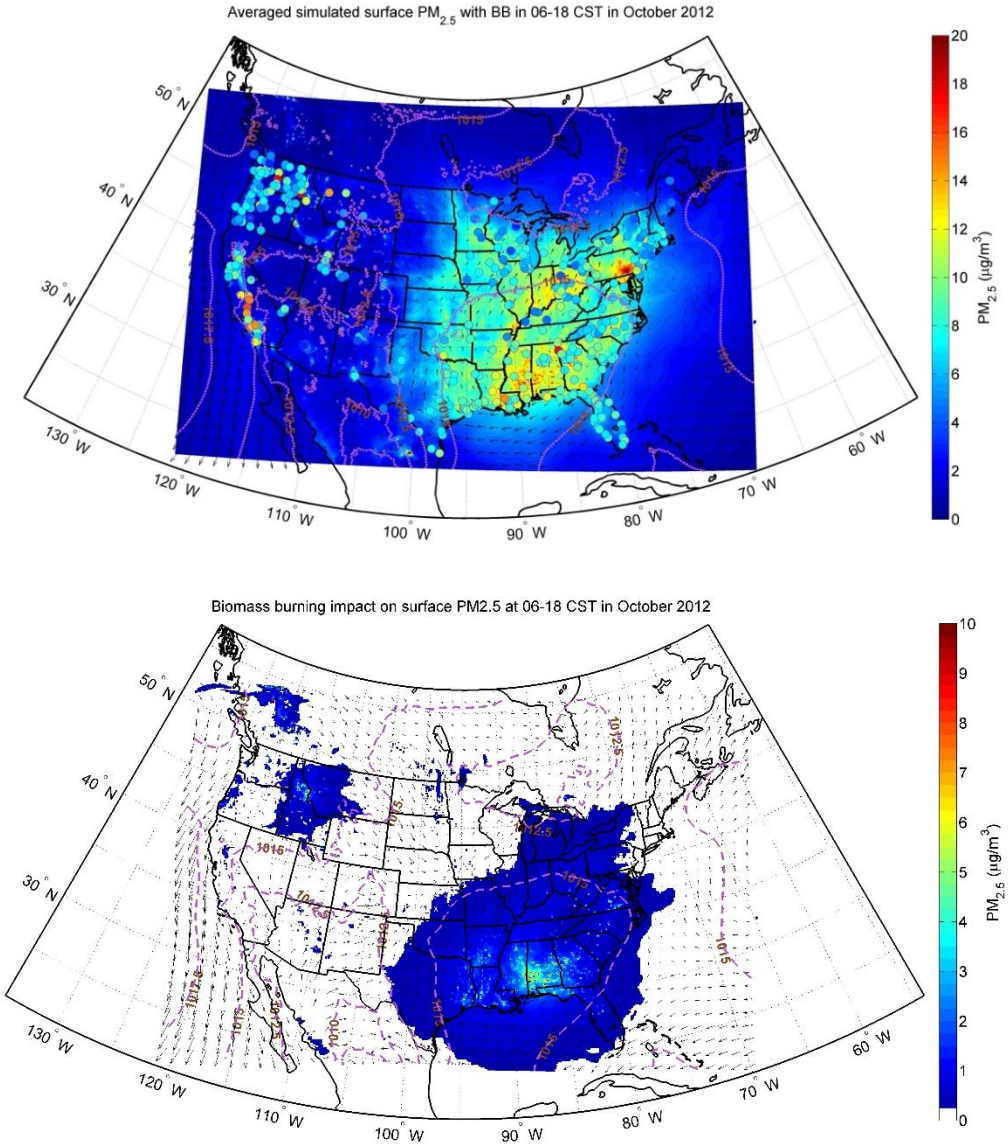

Figure 25: $PM_{2.5}$ model-measurement comparison and biomass burning impacts for the month of October, 2012. Top panel plots the ozone concentrations with biomass burning emissions included. In-situ data are represented by circles in the top panel. The bottom panel plots the differences between the biomass case and the non-biomass one.

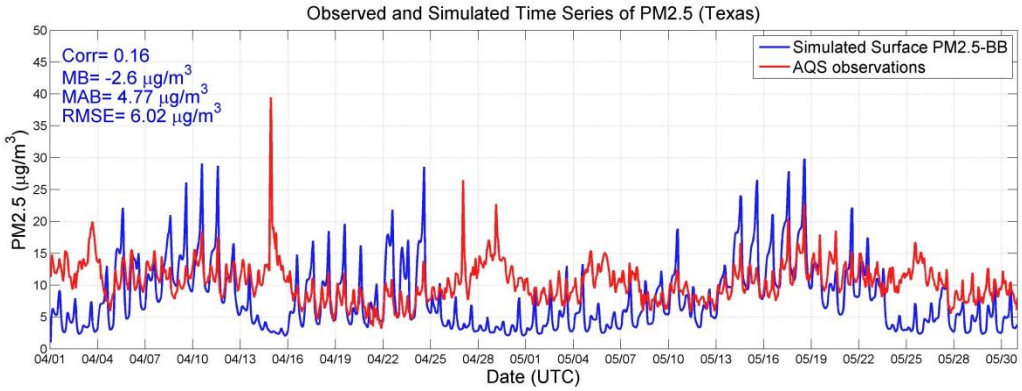

Figure 26: $PM_{2.5}$ time series for model-measurement comparison during spring 2012 for the state of Texas.

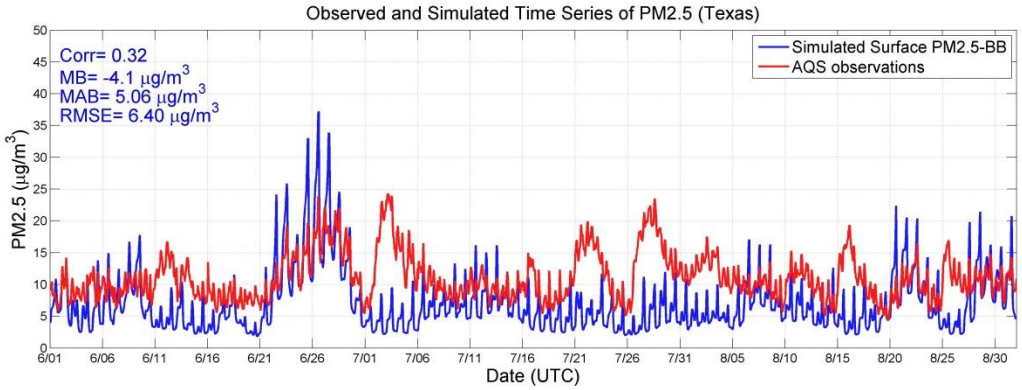

Figure 27: $PM_{2.5}$ time series for model-measurement comparison during summer 2012 for the state of Texas.

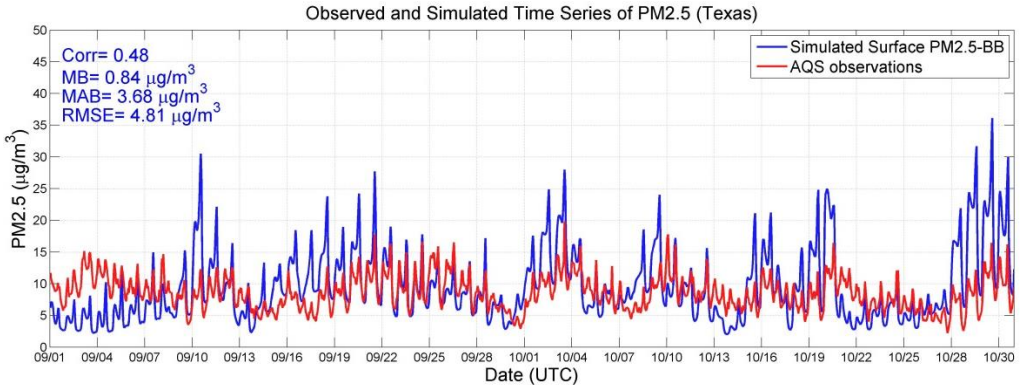

Figure 28: $PM_{2.5}$ time series for model-measurement comparison during fall 2012 for the state of Texas.

CO biomass burning impacts for 2012

This section describes the biomass burning impacts for CO, which is known to be a tracer for biomass burning. We highlight only the impacts, not the model-measurement contrasts because of the significant uncertainty in CO measurements across the AQS network. A CO impact of less than 5 ppb is predicted across most of the eastern U.S. across all seasons. Additionally, there are a couple of specific hotspots. For example in April (Figure 29), hotspots with point impacts of 10-20 ppb are predicted in Louisiana, Georgia, Florida, South Carolina and West Virginia. The impacts for May 2012 are plotted in Figure 30, which shows a 5-10 ppb enhancement is predicted in Idaho, and a 10-20 ppb change in northern Mexico. Figure 31 plots the changes for June, which shows couple of point fires in Louisiana, Georgia, Florida and New Mexico with 10-15 ppb increases. The predicted changes for July 2012 (Figure 32) indicate a significant impact of 25-30 ppb in southern Canada. In August 2012 (Figure 33), large fires in California, Idaho and Wyoming added 30 ppb CO into the region. The fire impacts in Idaho and Wyoming continued in September (Figure 34), but the impacts of the California fires seem to be a bit mitigated. However, there were fire events in the southern states of Arkansas, Louisiana, Alabama, Georgia and South Carolina, which added 10-20 ppb CO and intensified in regional impact in October as indicated in Figure 35.

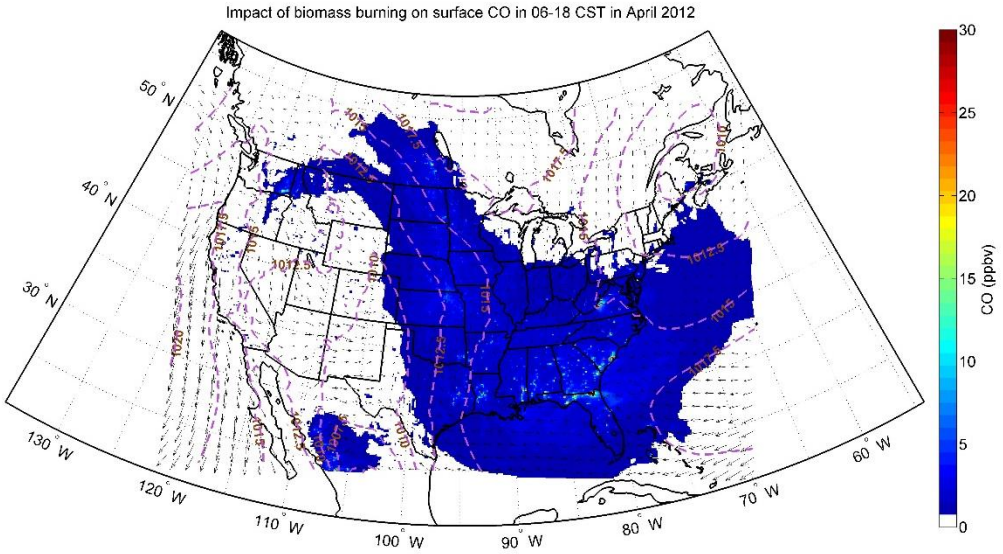

Figure 29: Effect of biomass burning on CO concentrations in April, 2012.

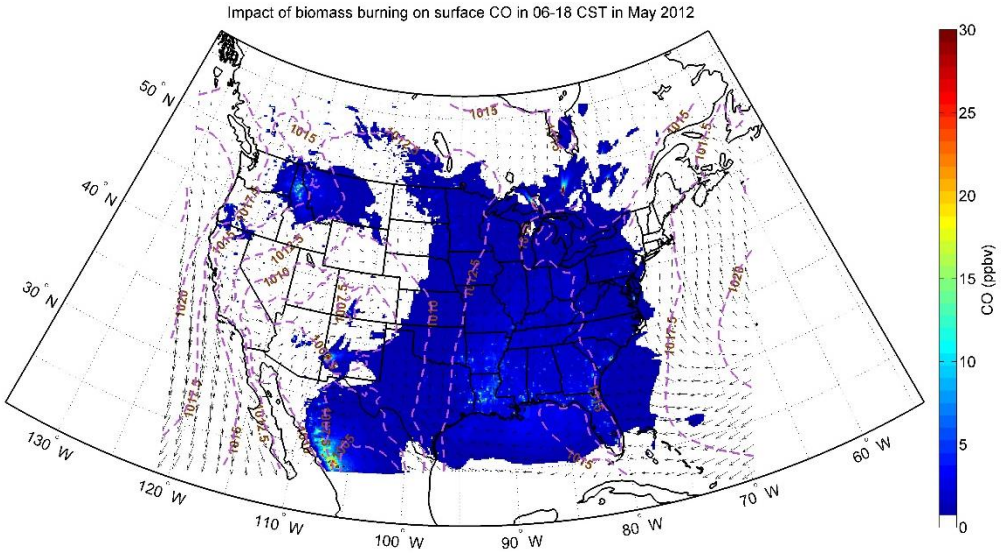

Figure 30: Effect of biomass burning on CO concentrations in May, 2012.

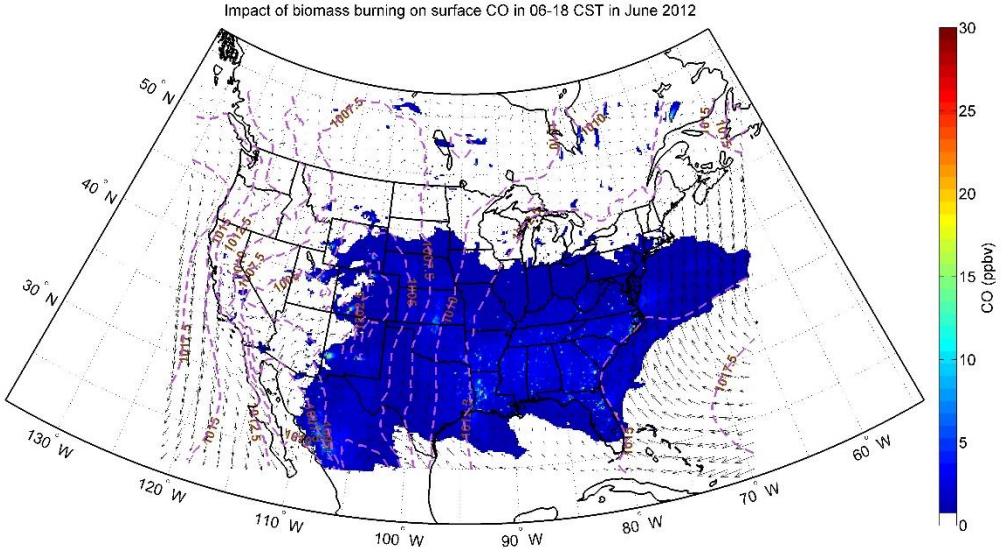

Figure 31: Effect of biomass burning on CO concentrations in June, 2012.

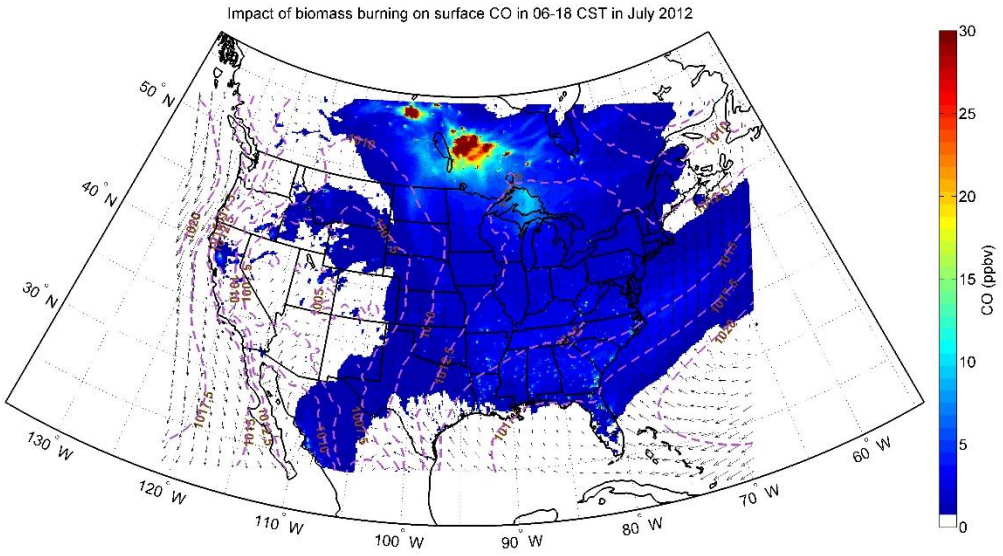

Figure 32: Effect of biomass burning on CO concentrations in July, 2012.

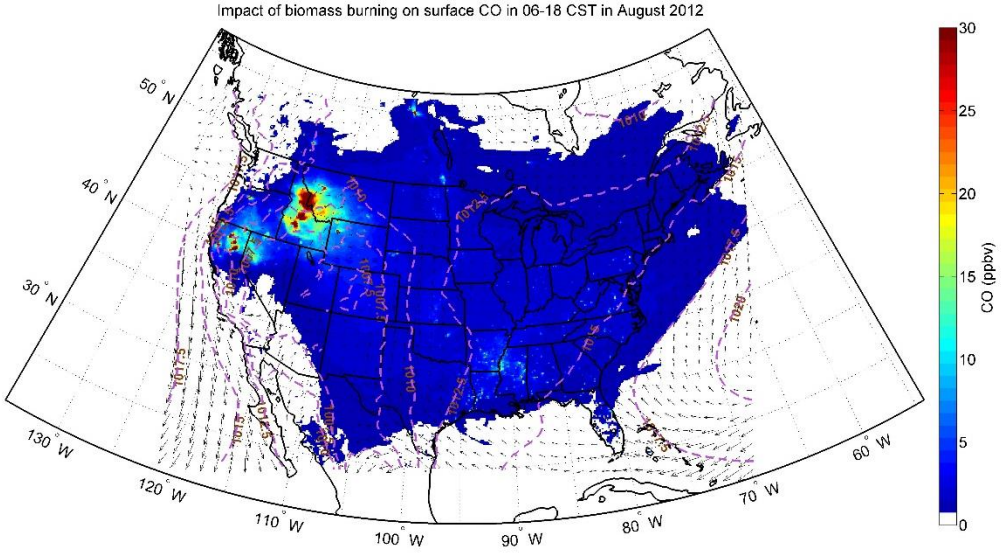

Figure 33: Effect of biomass burning on CO concentrations in August, 2012.

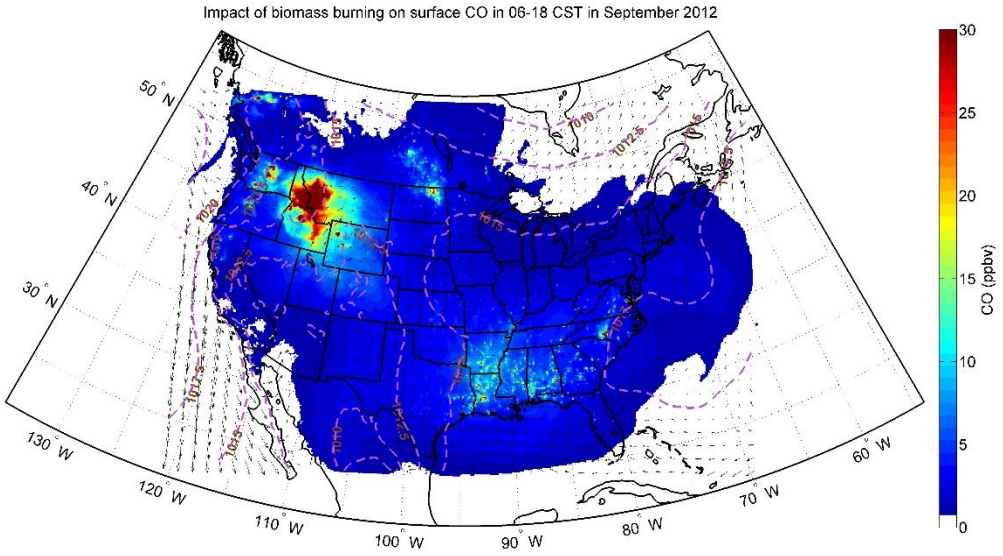

Figure 34: Effect of biomass burning on CO concentrations in September, 2012.

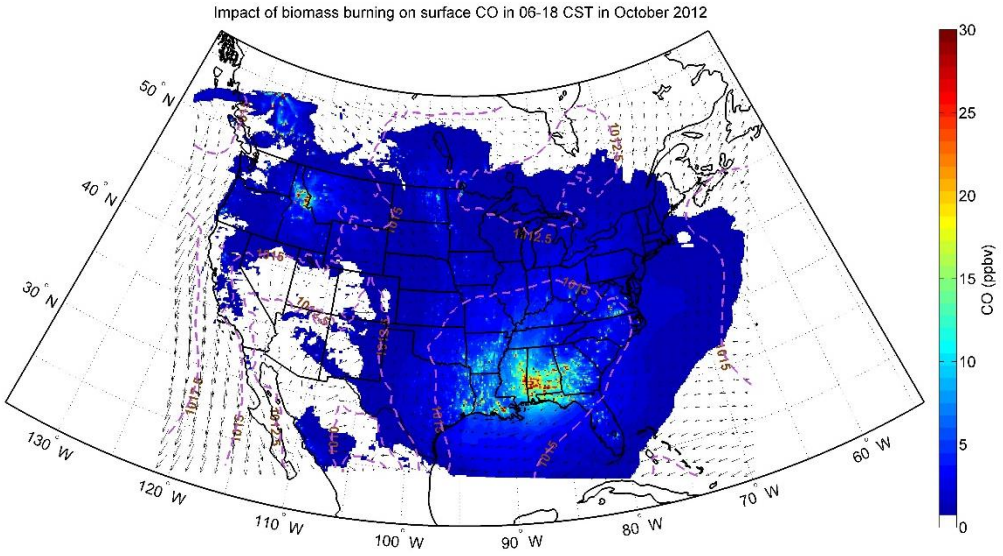

Figure 35: Effect of biomass burning on CO concentrations in October, 2012.

Ozone model-measurement comparisons and biomass burning impacts for 2013

The model-measurement comparisons and impacts of biomass burning for the ozone season in 2013 are plotted in Figures 36-42. In the comparison for April in Figure 36, in-situ data indicate there are hotspots in the Western Mountain region crossing 60 ppb, which the model is unable to capture. The biomass impact map in the bottom panel of the figure indicates an impact of less than 1 ppb across the eastern U.S. and some parts of California. Additionally, there is ~1 ppb impact at the border of Georgia and Florida.

The evaluation for the month of May, 2013 is indicated in Figure 37. The model is unable to capture the 60-70 ppb hotspots in the Western Mountain region and California. Interestingly, the

ozone concentrations over the eastern U.S. are quite low, around 35-40 ppb; and the model usually under-predicts these by 5-10 ppb. The biomass impacts contour plot in the bottom panel reveals that biomass burning had an impact of less than 1 ppb across the entire continental U.S., with a 1 ppb change at the border of Georgia and Florida, and over northern Mexico.

The comparison for June 2013 is plotted in Figure 38. The model is unable to capture the hotspots over the Western Mountain region and California, but does a reasonably good job of capturing the lower concentrations of 30-40 ppb over the eastern U.S. The biomass impact contour map in the bottom panel indicates wildfire impacts of 1-3 ppb in northern Mexico and southeastern Canada, with 1 ppb impacts being predicted in Florida, New Mexico and Colorado.

Figure 39 plots the modeling for the month of July, 2013. The model performs reasonably well in capturing the hotspots in the Western Mountain Region but still under-predicts in California. It reasonably captures the low ozone concentrations over the eastern U.S. The biomass impacts in the bottom panel indicate 1-3 ppb impacts in southeastern Canada, with 1 ppb impacts seen in Oklahoma and Kansas.

The comparisons and impacts for the month of August are plotted in Figure 40. The model captures the high ozone on the Western Mountain area and the lower concentrations in the eastern U.S. reasonably well, but under-predicts in California. The biomass impacts in the bottom panel indicate changes of ~ 2 ppb in Idaho and northern California, with 1 ppb impacts predicted for Louisiana, Arkansas and Georgia.

Figure 41 plots the comparisons and impacts for the month of September, 2013. Ozone concentrations across the continental U.S. are typically low except for some hotspots in the Western Mountain region and California. The model under-predicts these hotspots but over-predicts the low concentrations over the eastern U.S. The biomass impacts plot indicates an impact of ~ 0.5 ppb across the continental U.S., with an impact of ~ 1ppb in Alabama, Arkansas, Louisiana, and eastern Texas. Additionally, there is a 2-3 ppb impact in northeastern California.

Figure 42 plots the model evaluation and impact for October 2013. Ozone concentrations were typically low during this month, with the exceptions being a couple of places in California and the Western Mountain region. The model was capable of capturing the low concentrations over the eastern U.S. but under-predicted the hotspots in the Western Mountain region and California. The biomass impact plot shows that forest fires raised ozone over the continental U.S. by less than 1 ppb, while a 1 ppb impact was predicted over Alabama, Georgia, Idaho, Wyoming and southern Canada.

Figures 43-45 plot the time-series of the model-measurement comparisons for the state of Texas for the spring, summer and fall respectively. The comparisons show a good correlation in spring (0.81), but excellent correlation in summer and fall (0.93 and 0.92 respectively). These numbers indicate that the model performs quite well in reproducing the spatio-temporal trends of the in-situ data. However, the model tends to over-predict more than what it did in 2012.

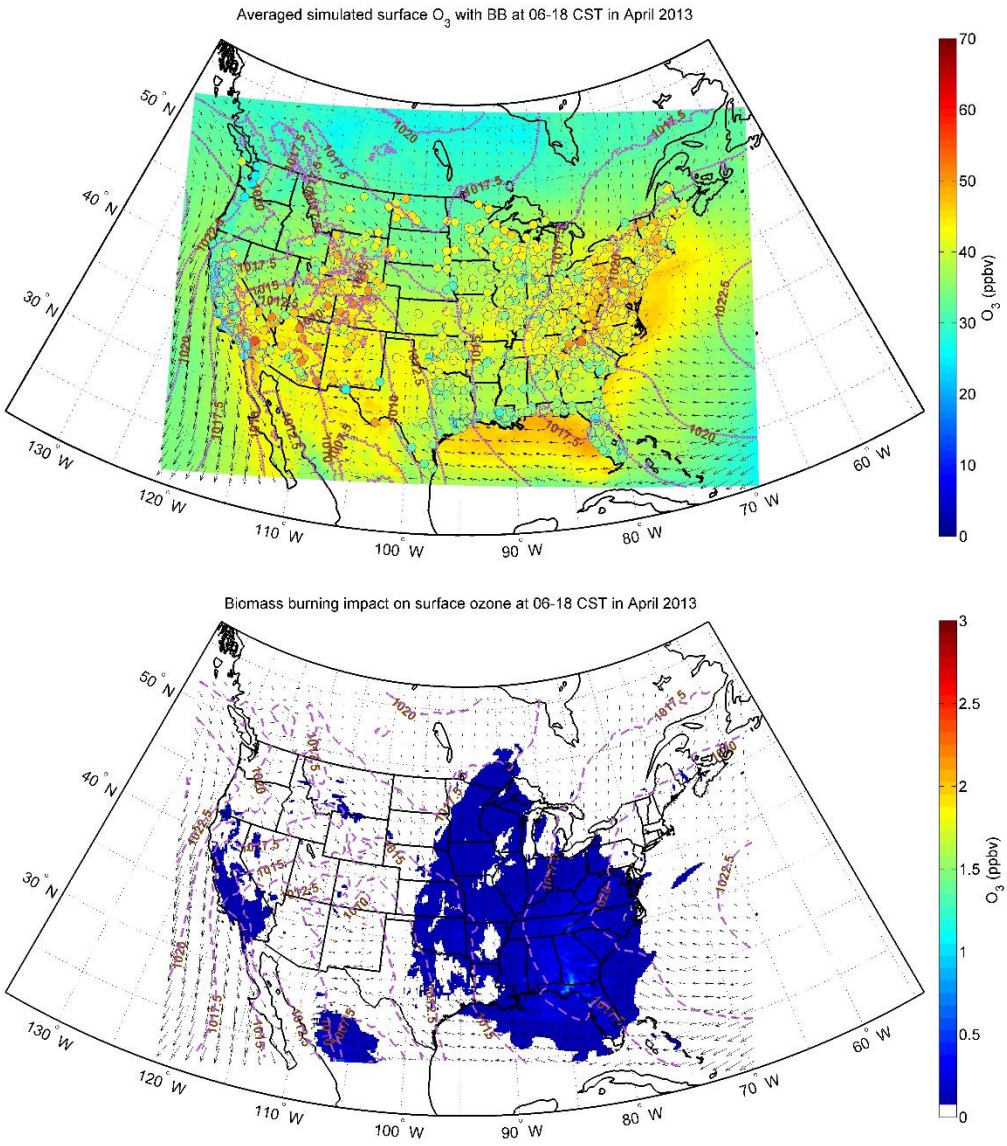

Figure 36: Ozone model-measurement comparison and biomass burning impacts for the month of April, 2013. Top panel plots the ozone concentrations with biomass burning emissions included. In-situ data are represented by circles in the top panel. The bottom panel plots the differences between the biomass case and the non-biomass one.

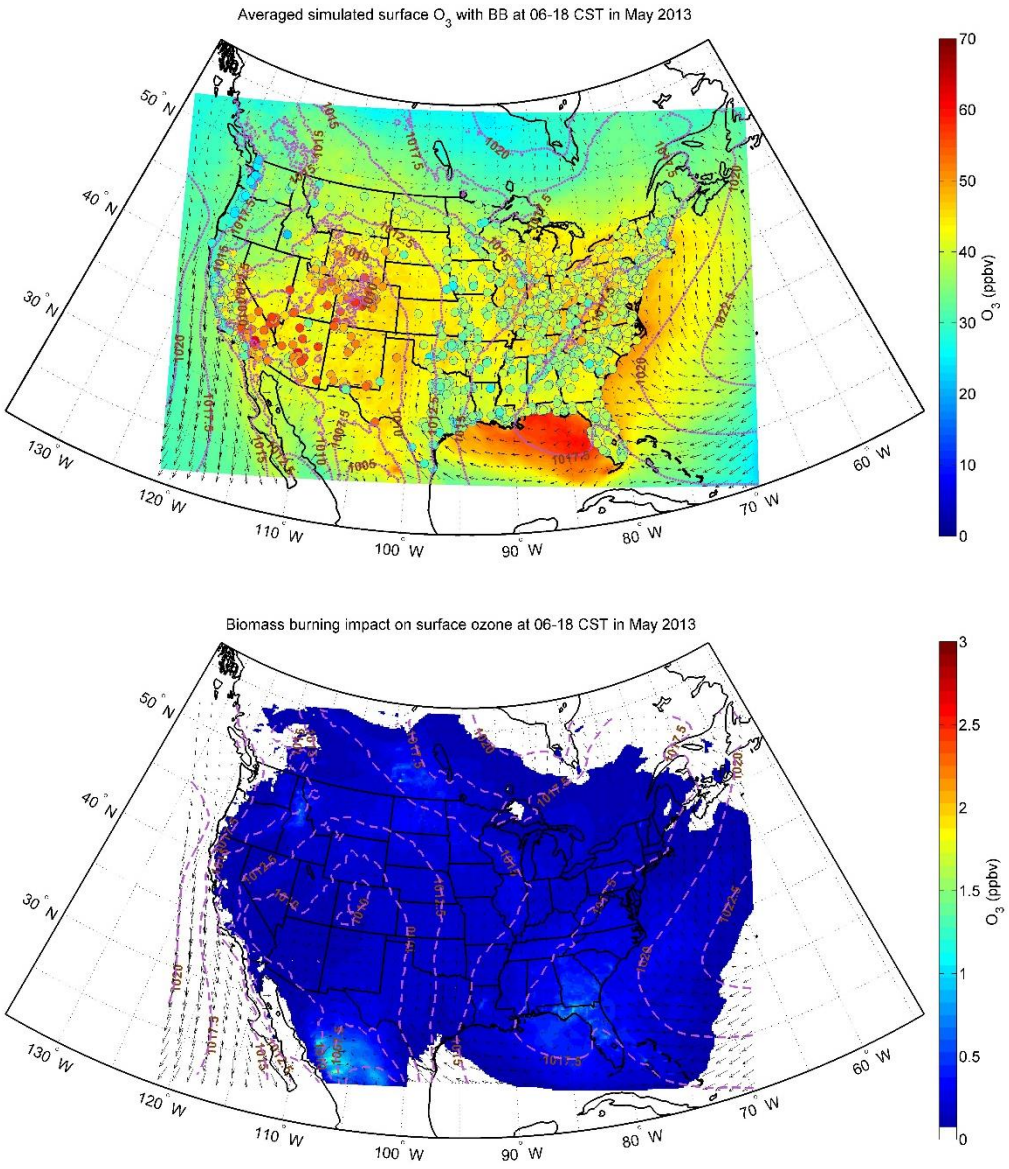

Figure 37: Ozone model-measurement comparison and biomass burning impacts for the month of May, 2013. Top panel plots the ozone concentrations with biomass burning emissions included. In-situ data are represented by circles in the top panel. The bottom panel plots the differences between the biomass case and the non-biomass one.

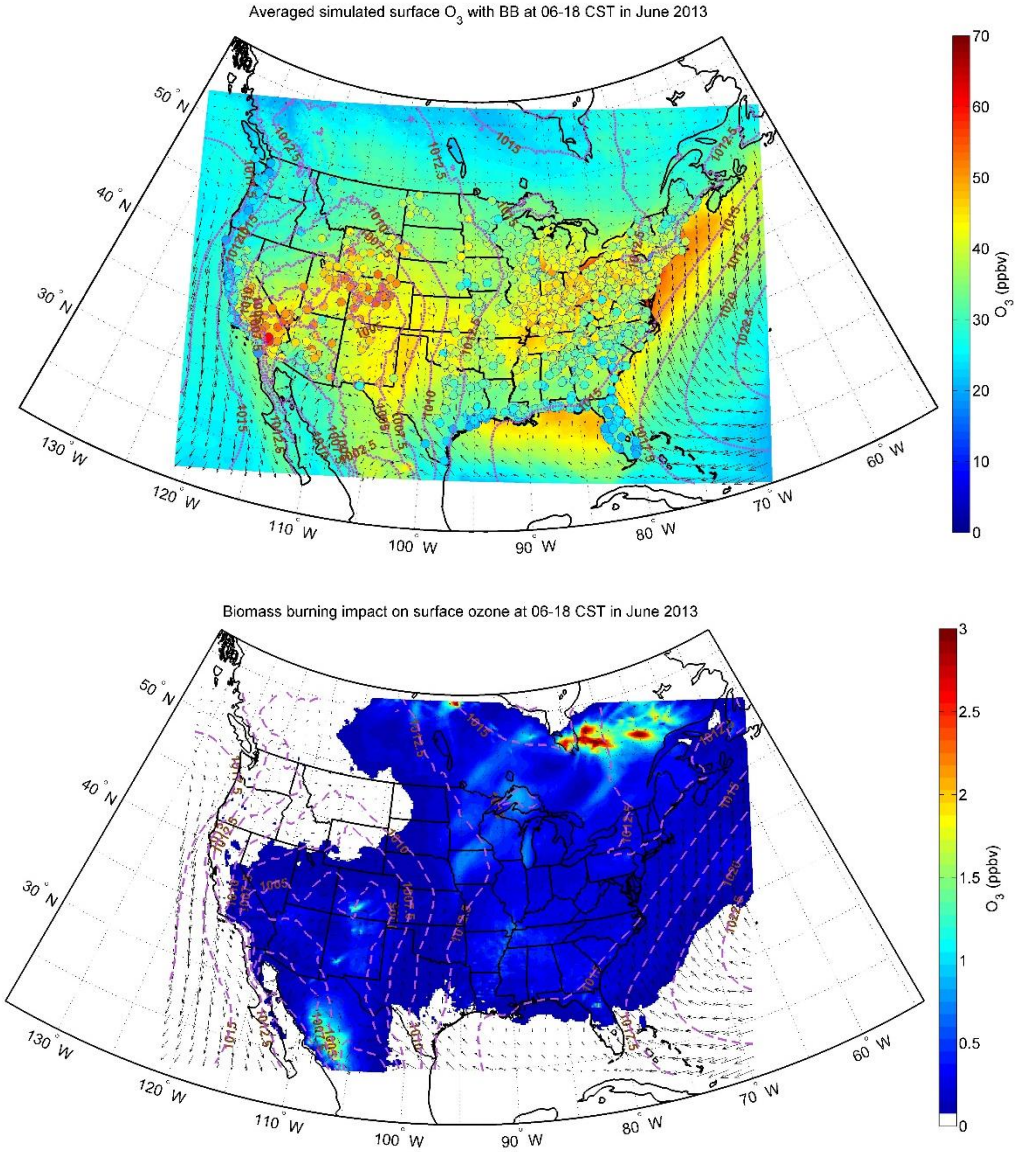

Figure 38: Ozone model-measurement comparison and biomass burning impacts for the month of June, 2013. Top panel plots the ozone concentrations with biomass burning emissions included. In-situ data are represented by circles in the top panel. The bottom panel plots the differences between the biomass case and the non-biomass one.

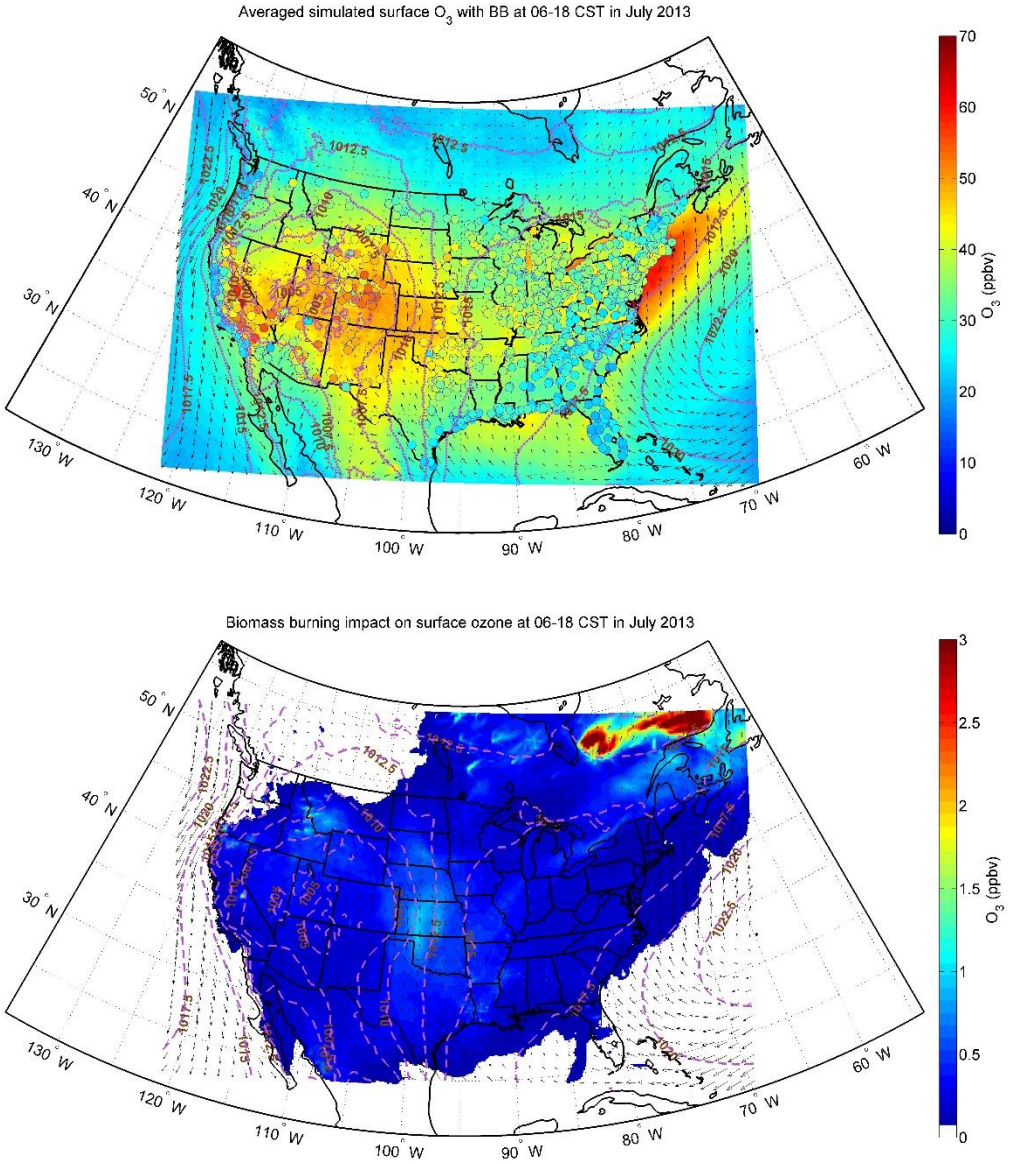

Figure 39: Ozone model-measurement comparison and biomass burning impacts for the month of July, 2013. Top panel plots the ozone concentrations with biomass burning emissions included. In-situ data are represented by circles in the top panel. The bottom panel plots the differences between the biomass case and the non-biomass one.

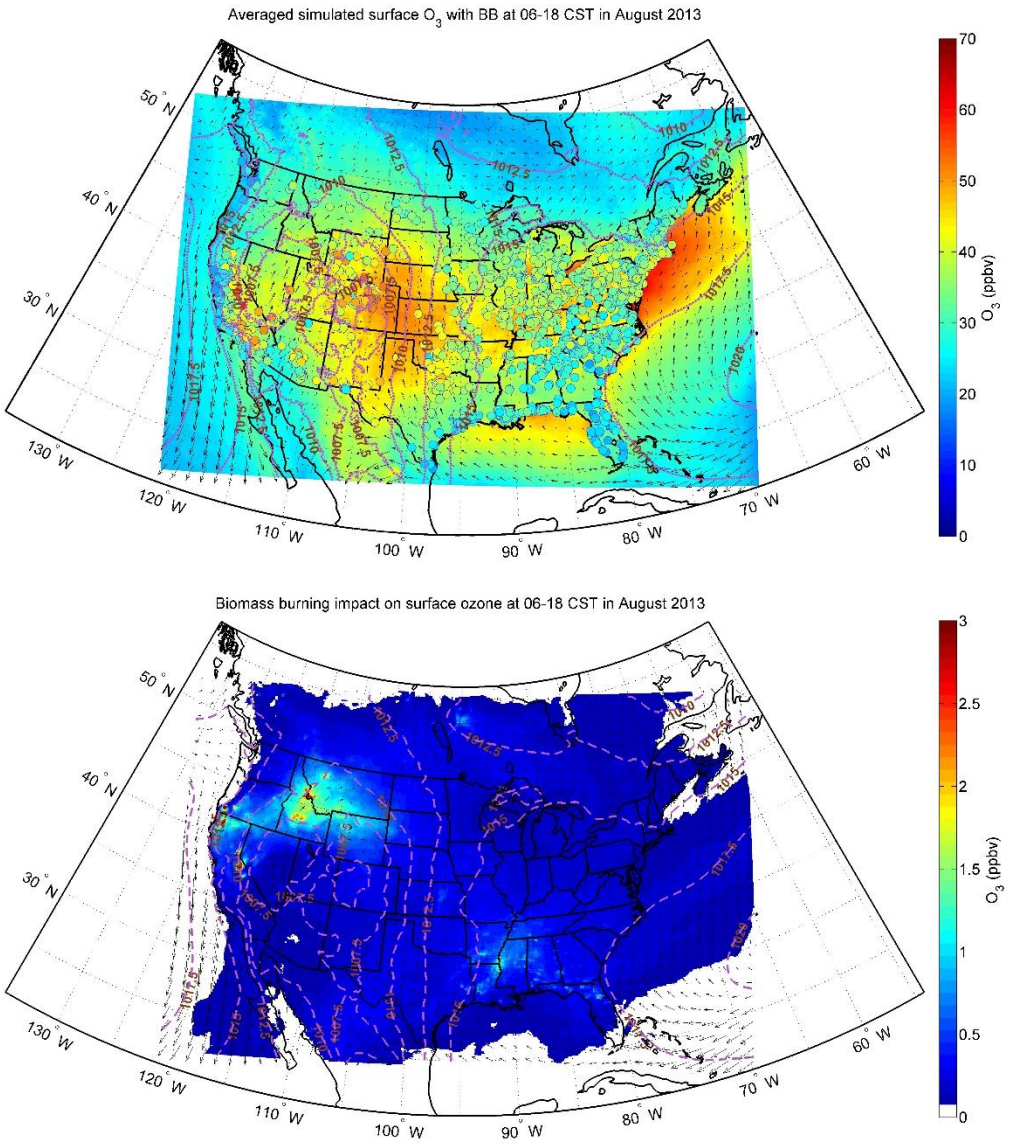

Figure 40: Ozone model-measurement comparison and biomass burning impacts for the month of August, 2013. Top panel plots the ozone concentrations with biomass burning emissions included. In-situ data are represented by circles in the top panel. The bottom panel plots the differences between the biomass case and the non-biomass one.

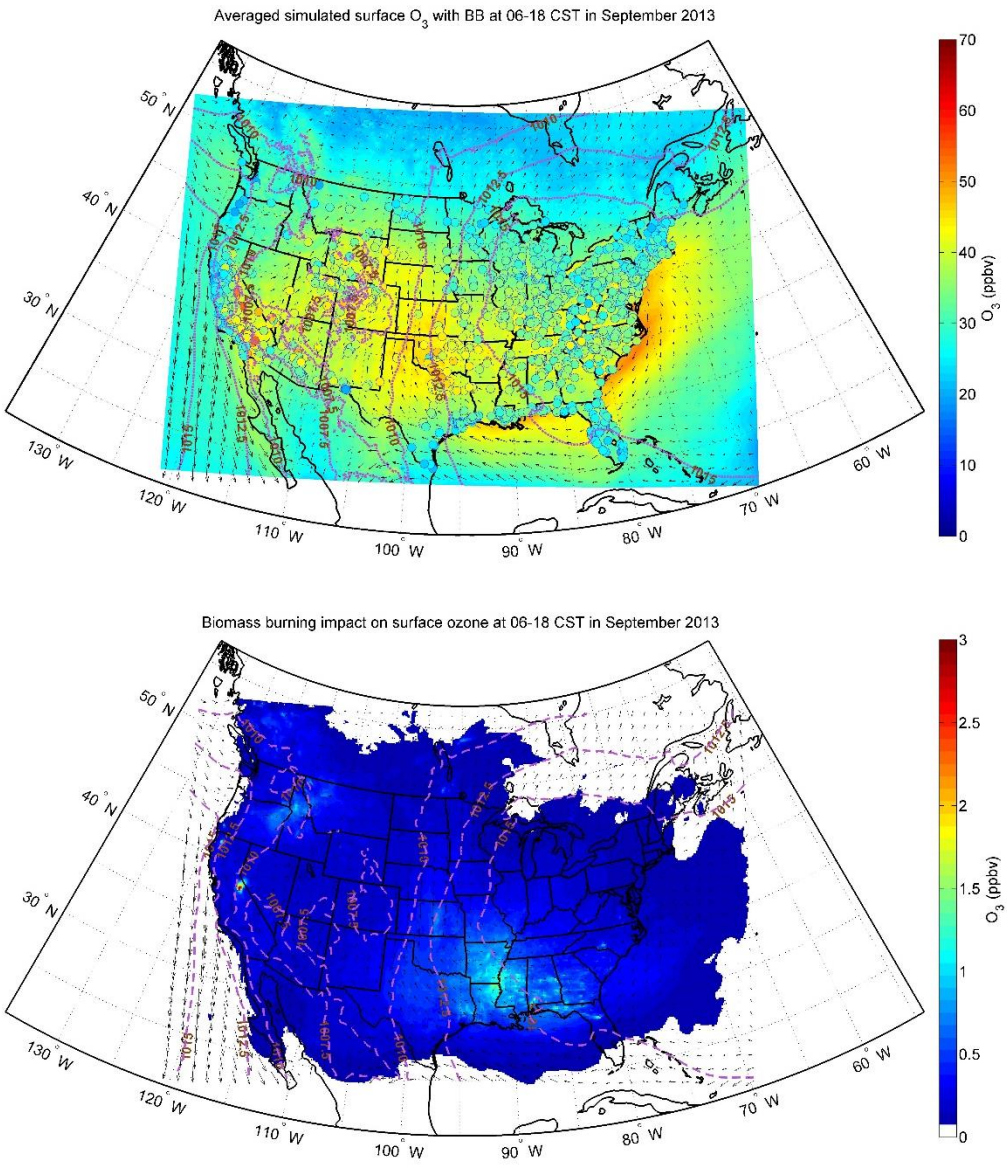

Figure 41: Ozone model-measurement comparison and biomass burning impacts for the month of September, 2013. Top panel plots the ozone concentrations with biomass burning emissions included. In-situ data are represented by circles in the top panel. The bottom panel plots the differences between the biomass case and the non-biomass one.

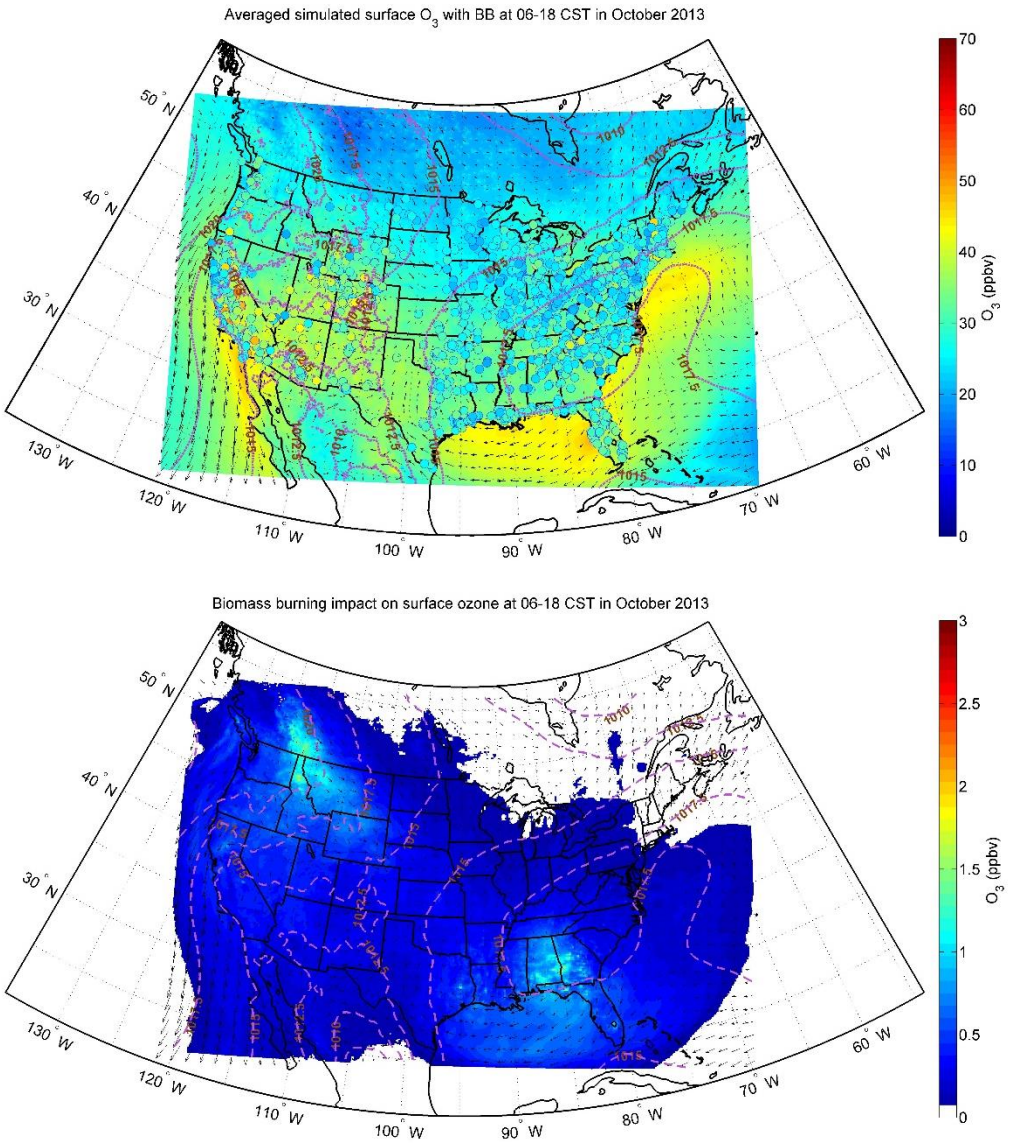

Figure 42: Ozone model-measurement comparison and biomass burning impacts for the month of October, 2013. Top panel plots the ozone concentrations with biomass burning emissions included. In-situ data are represented by circles in the top panel. The bottom panel plots the differences between the biomass case and the non-biomass one.

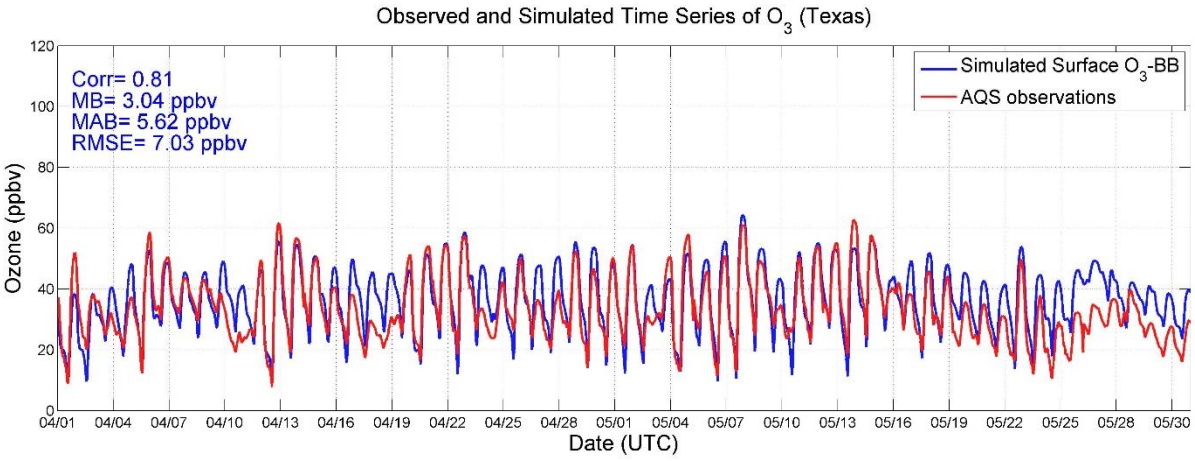

Figure 43: Ozone time series for model-measurement comparison during spring 2013 for the state of Texas.

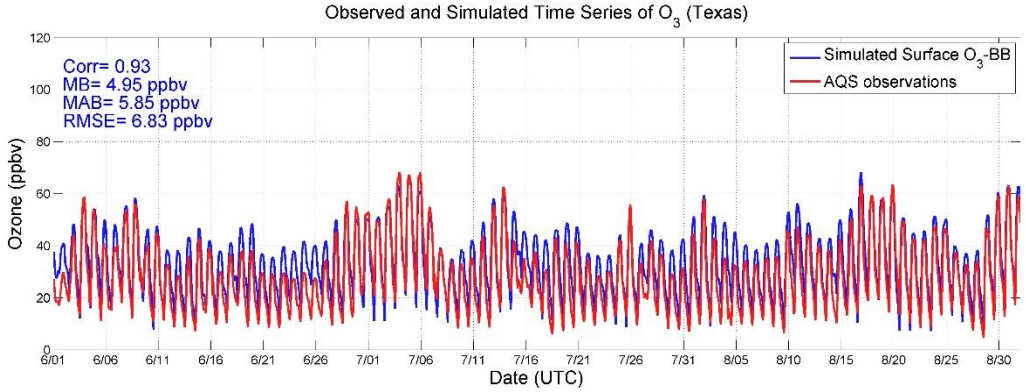

Figure 44: Ozone time series for model-measurement comparison during summer 2013 for the state of Texas.

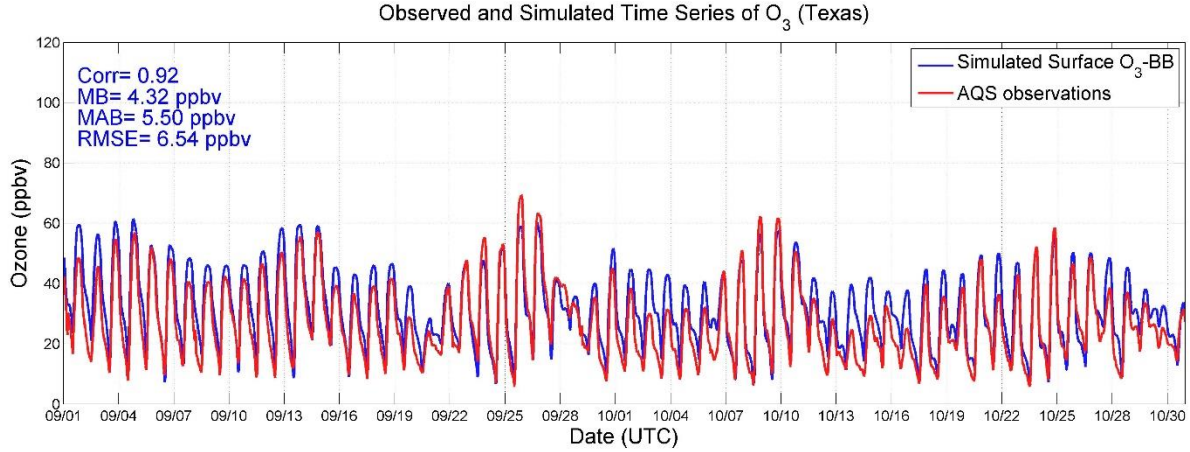

Figure 45: Ozone time series for model-measurement comparison during fall 2013 for the state of Texas.

$PM_{2.5}$ model-measurement comparisons and biomass burning impacts for 2013

The model-measurement comparisons and impacts of biomass burning emissions over the continental U.S. is plotted in Figure 46-52. Broadly, the in-situ data show concentrations of 8-10 $\mu g\ m^{-3}$ over the eastern U.S. which the model does a reasonably good job at capturing. However, it still under-predicts in Texas and at several places in California, and also in Washington as we move towards the fall months. However, the biomass impacts show different spatial trends. The plot in the bottom panel of Figure 46 indicates that the fires roughly caused a change of 1 $\mu g\ m^{-3}$ in Georgia, Alabama, eastern Texas and southern Oklahoma in April 2013. A similar story is revealed for May 2013 in Figure 47. However, the biomass fires cause a change of 1 $\mu g\ m^{-3}$ in Georgia, South Carolina, Alabama, Louisiana and almost entire Florida, in addition to northern Mexico, western Idaho and eastern Washington. Figure 48 and 49 indicate that in June and July 2013, biomass fires in southeastern Canada elevated $PM_{2.5}$ concentrations there by 5-10 $\mu g\ m^{-3}$. In Figure 50, biomass burning impacts of around 1 $\mu g\ m^{-3}$ are seen over Georgia, Alabama and Louisiana, some places in the Mid-West, as well as Idaho, Wyoming and California. In September 2013 (Figure 51), biomass impacts of 1 $\mu g\ m^{-3}$ are predicted over a significant part of the eastern U.S., along with California, Idaho, Wyoming and southwestern Canada. In Figure 52 for October 2013, elevated $PM_{2.5}$ in-situ concentrations are seen over the eastern U.S., which the model is unable to reproduce. Similarly, it is unable to capture the west coast hotspots. The bottom panel plot indicates that biomass fires in October changed $PM_{2.5}$ by 1 $\mu g\ m^{-3}$ in most of the eastern U.S. and the Mid-West, Idaho, Wyoming, Washington, California and Oregon. In addition, changes of 5-10 $\mu g\ m^{-3}$ were also predicted in eastern Texas, Louisiana, Alabama, Georgia, Idaho and southwestern Canada.

The time-series for the state of Texas are plotted in Figures 53-54 for the spring and fall seasons, respectively. The summer correlation was relatively poorer so we chose to not include it in this report. A significant under-prediction is seen for spring, which narrows down in the fall. However, the model exhibits poor correlation in both seasons.

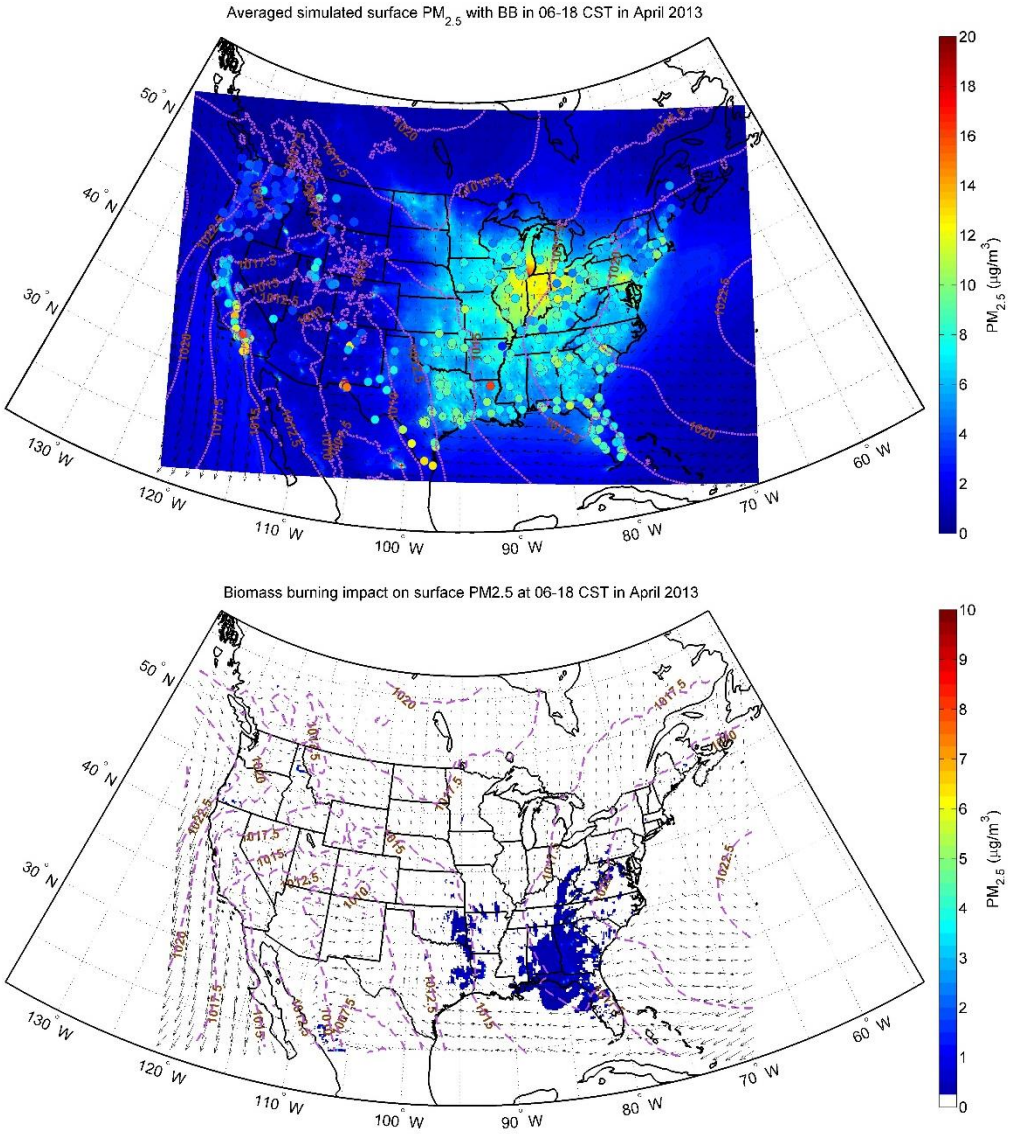

Figure 46: $PM_{2.5}$ model-measurement comparison and biomass burning impacts for the month of April, 2013. Top panel plots the ozone concentrations with biomass burning emissions included. In-situ data are represented by circles in the top panel. The bottom panel plots the differences between the biomass case and the non-biomass one.

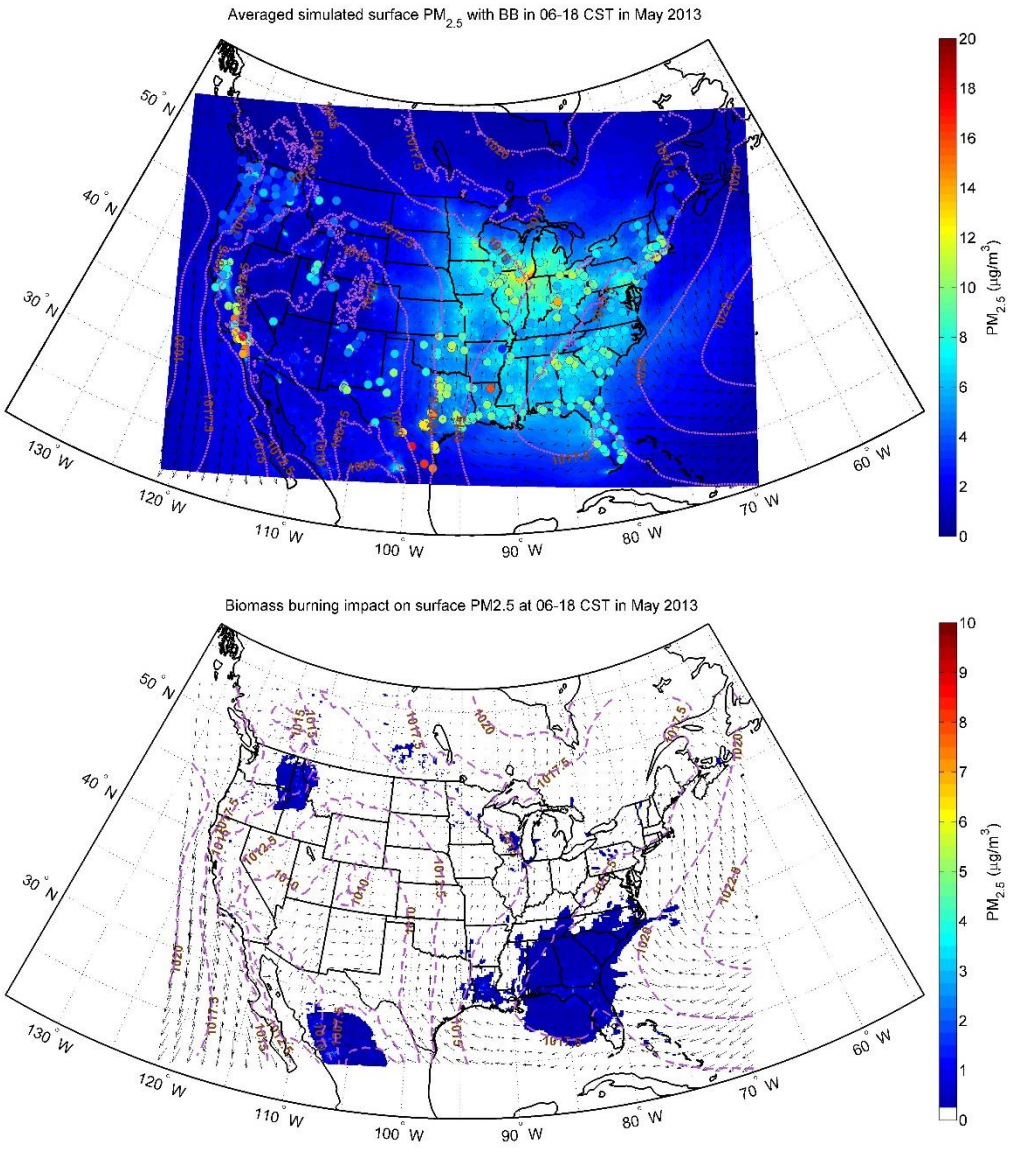

Figure 47: $PM_{2.5}$ model-measurement comparison and biomass burning impacts for the month of May, 2013. Top panel plots the ozone concentrations with biomass burning emissions included. In-situ data are represented by circles in the top panel. The bottom panel plots the differences between the biomass case and the non-biomass one.

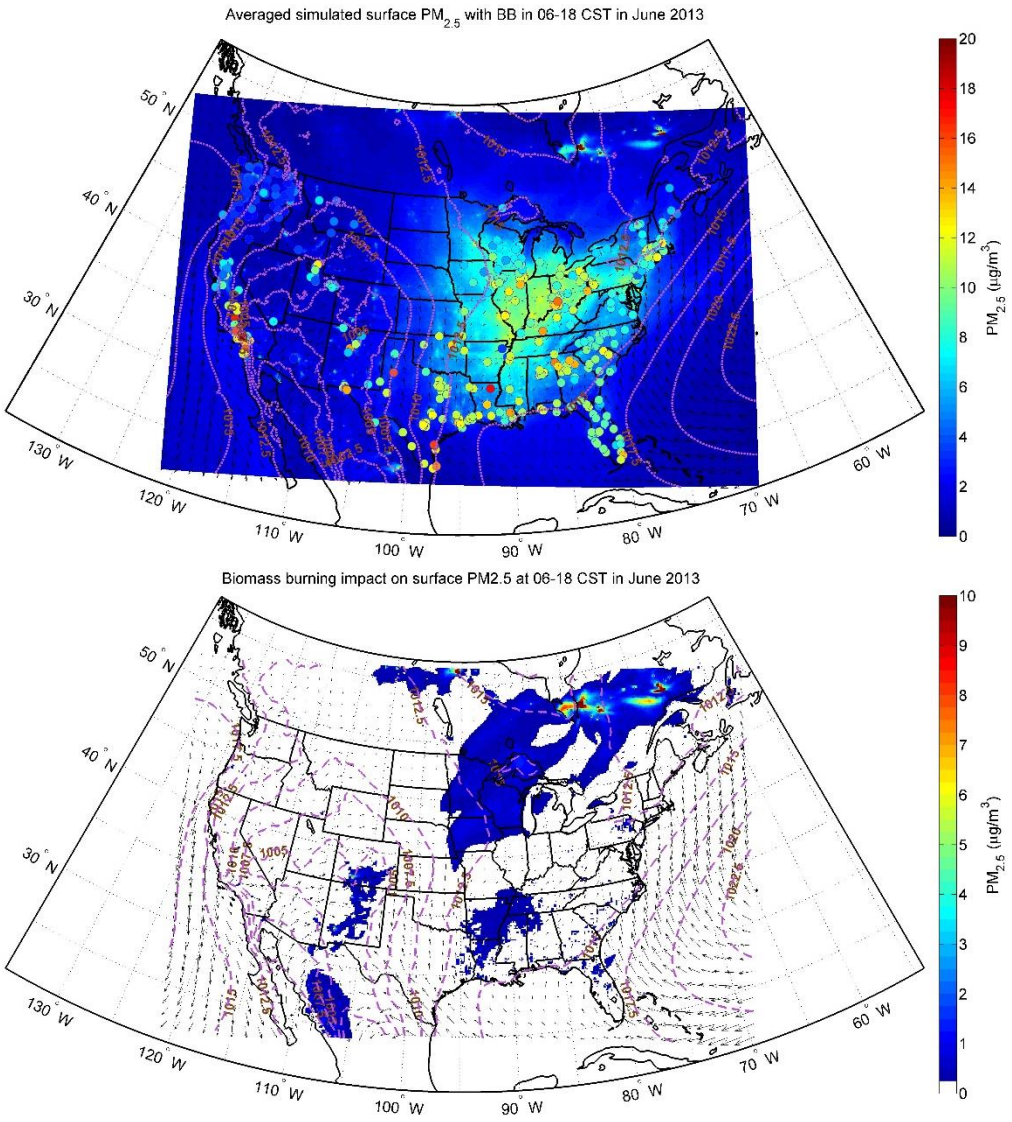

Figure 48: $PM_{2.5}$ model-measurement comparison and biomass burning impacts for the month of June, 2013. Top panel plots the ozone concentrations with biomass burning emissions included. In-situ data are represented by circles in the top panel. The bottom panel plots the differences between the biomass case and the non-biomass one.

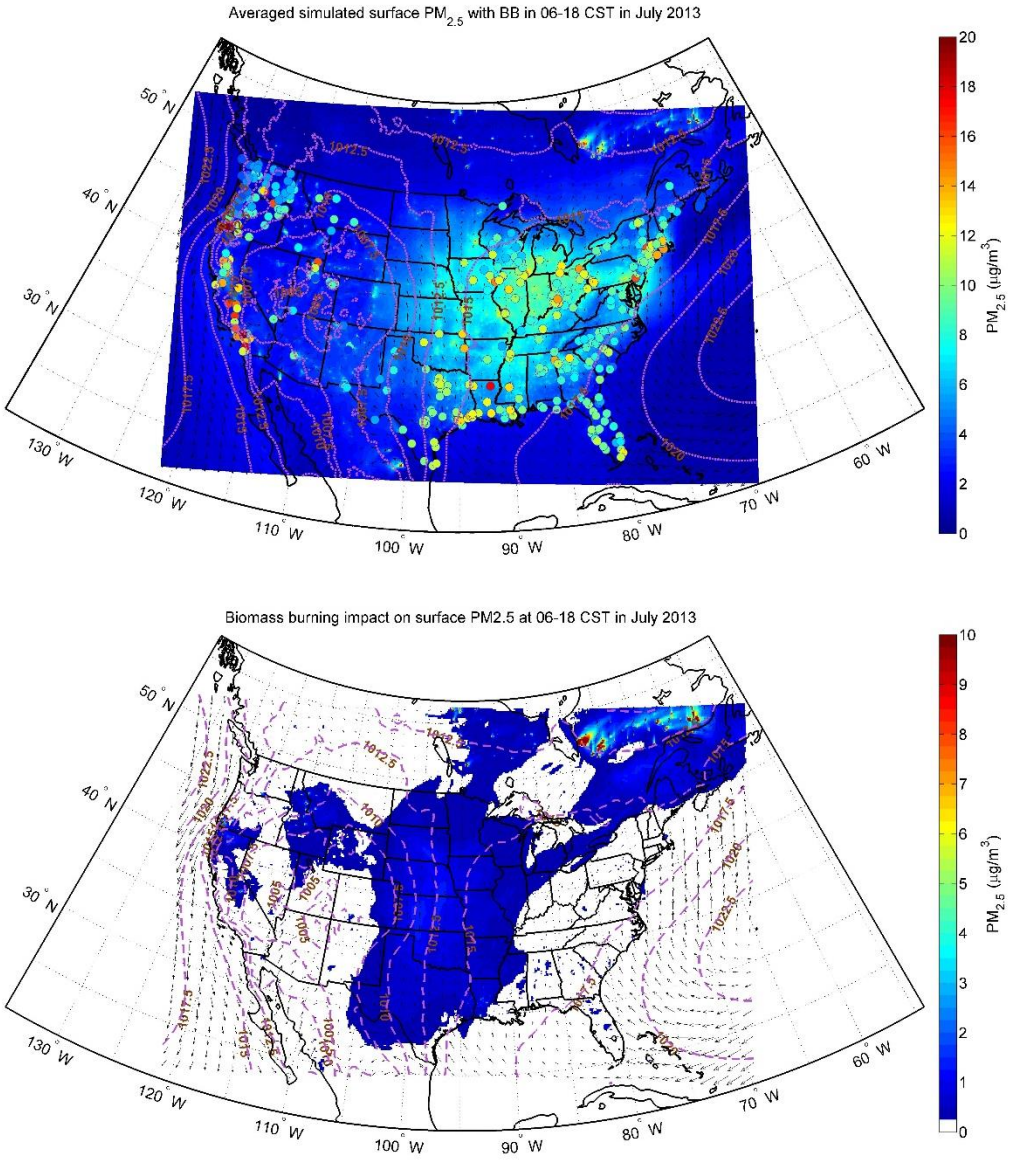

Figure 49: $PM_{2.5}$ model-measurement comparison and biomass burning impacts for the month of July, 2013. Top panel plots the ozone concentrations with biomass burning emissions included. In-situ data are represented by circles in the top panel. The bottom panel plots the differences between the biomass case and the non-biomass one.

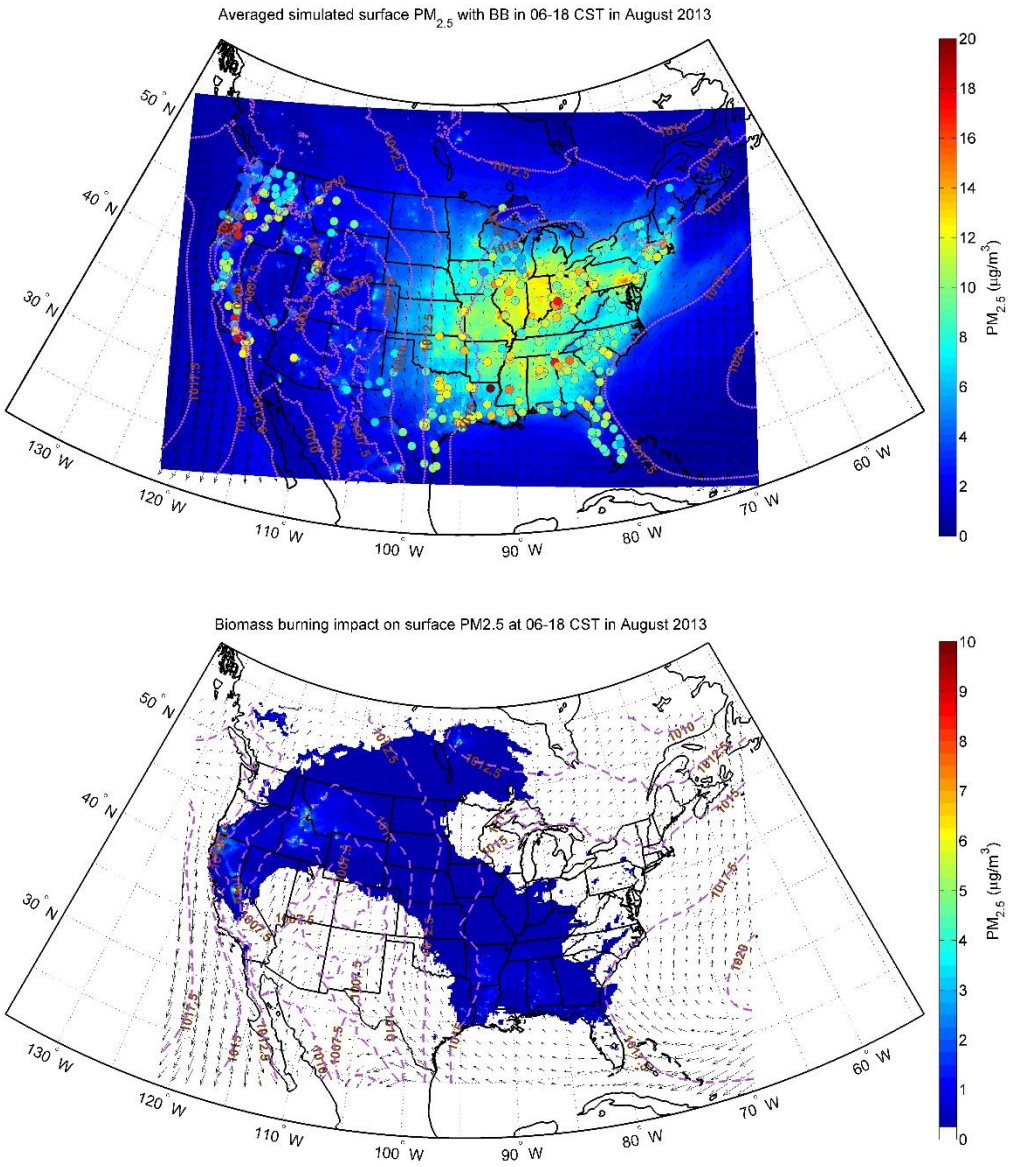

Figure 50: $PM_{2.5}$ model-measurement comparison and biomass burning impacts for the month of August, 2013. Top panel plots the ozone concentrations with biomass burning emissions included. In-situ data are represented by circles in the top panel. The bottom panel plots the differences between the biomass case and the non-biomass one.

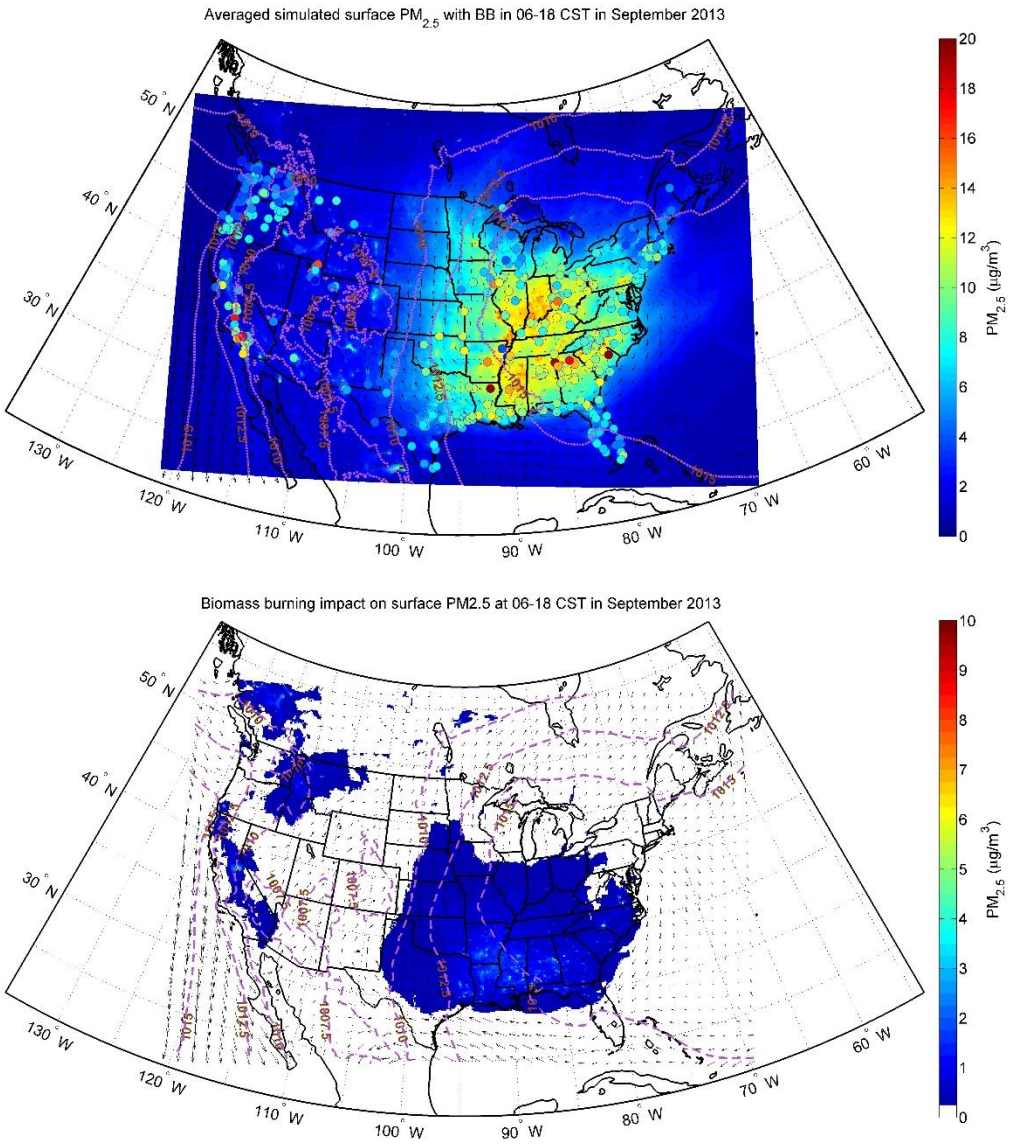

Figure 51: $PM_{2.5}$ model-measurement comparison and biomass burning impacts for the month of September, 2013. Top panel plots the ozone concentrations with biomass burning emissions included. In-situ data are represented by circles in the top panel. The bottom panel plots the differences between the biomass case and the non-biomass one.

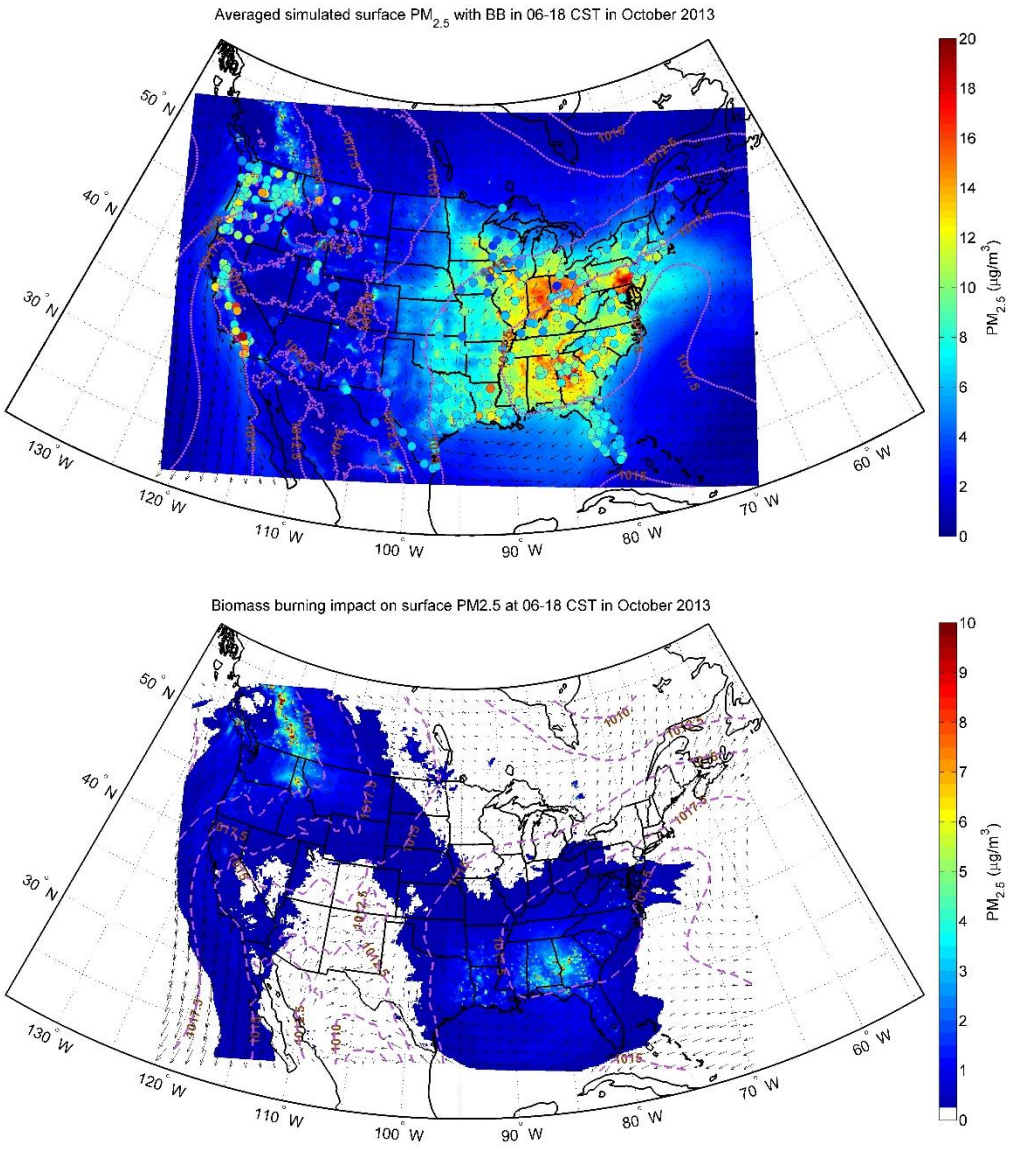

Figure 52: $PM_{2.5}$ model-measurement comparison and biomass burning impacts for the month of October, 2013. Top panel plots the ozone concentrations with biomass burning emissions included. In-situ data are represented by circles in the top panel. The bottom panel plots the differences between the biomass case and the non-biomass one.

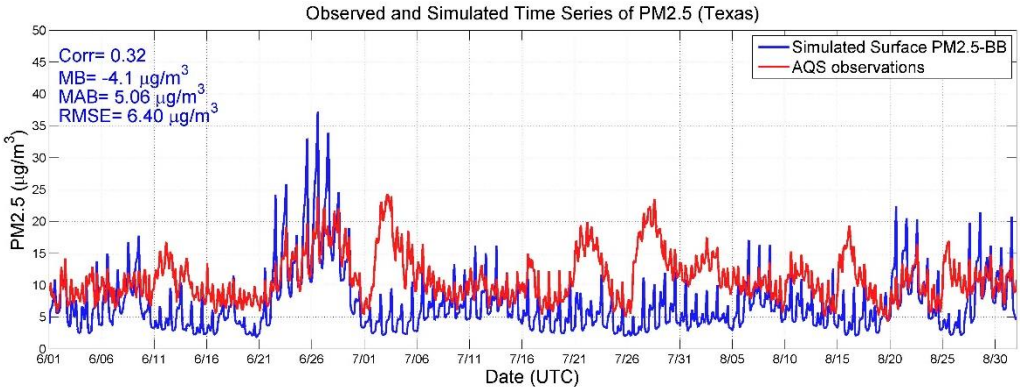

Figure 53: $PM_{2.5}$ time series for model-measurement comparison during summer 2013 for the state of Texas.

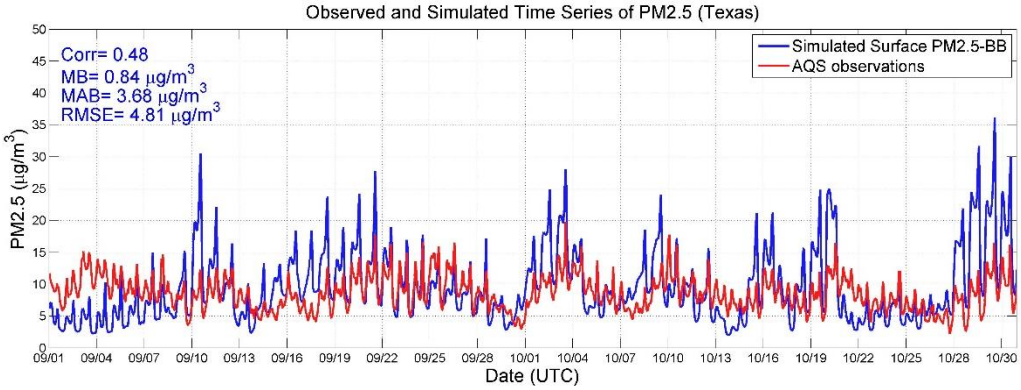

Figure 54: $PM_{2.5}$ time series for model-measurement comparison during fall 2013 for the state of Texas.

CO biomass burning impacts for 2013

The CO impacts of biomass burning for the months of April-October 2013 are plotted in Figures 55-61. An impact of around 5 ppb is predicted along a large part of the eastern U.S. in April, as indicated in Figure 55. Some regions along the Midwest also experience similar impacts. The predictions for May 2013 in Figure 56 indicate a 5 ppb impact across the east and Midwest, as well as northern Mexico, Idaho, Washington and Wyoming. For the month of June in Figure 57, an increase of 5 ppb is predicted across the entire eastern half of the U.S., along with some parts of California and Mexico. Also, fire hotspots of 15-30 ppb are predicted across southeastern Canada. For July 2013 (Figure 58), a 5 ppb increase is predicted across the east and Midwest, along with hotspots of 15-30 ppb in southeastern Canada. An impact of 5 ppb is predicted across almost the entire continental U.S. for August and September in Figures 59 and 60 respectively. In August, there were small fire events in east Texas, Louisiana, Arkansas, Alabama and Mississippi, adding ~ 10 ppb of CO. Additionally, there were larger events in northern California and Idaho adding up to 25 ppb into these regions. In September 2013, forest fires in Texas, Louisiana, Arkansas, Alabama and Mississippi and Georgia resulted in a 10 ppb difference. Biomass fires in October 2013 added 15-25 ppb of CO on Georgia, Alabama, northern Idaho and southeastern

Canada, and 15 ppb in northern California, Mississippi, Louisiana, eastern Texas and southern Arkansas.

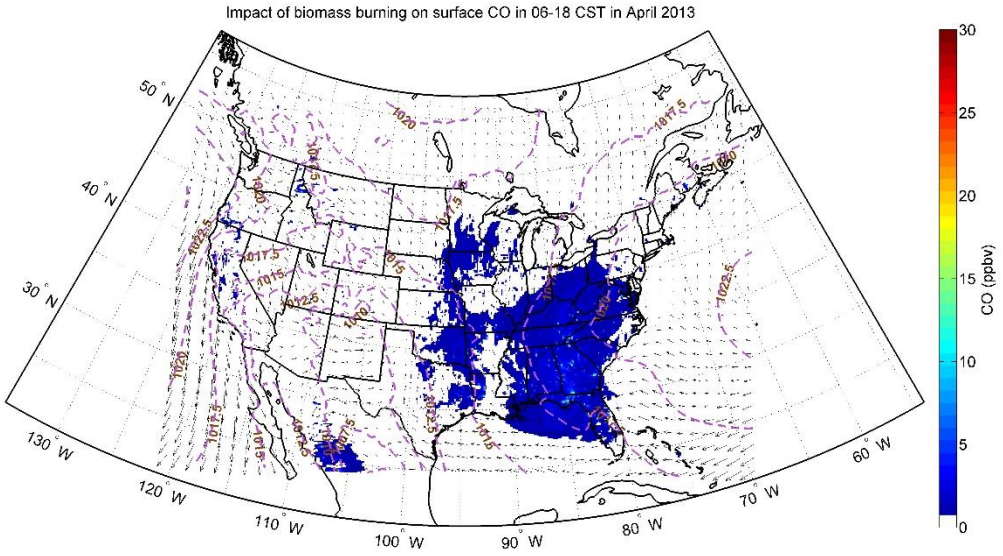

Figure 55: Effect of biomass burning on CO concentrations in April, 2013.

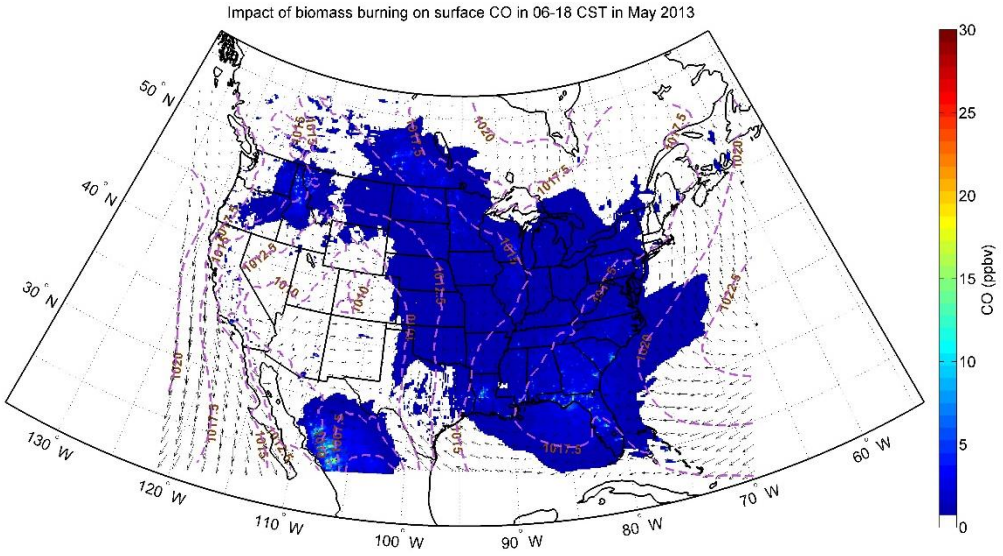

Figure 56: Effect of biomass burning on CO concentrations in May, 2013.

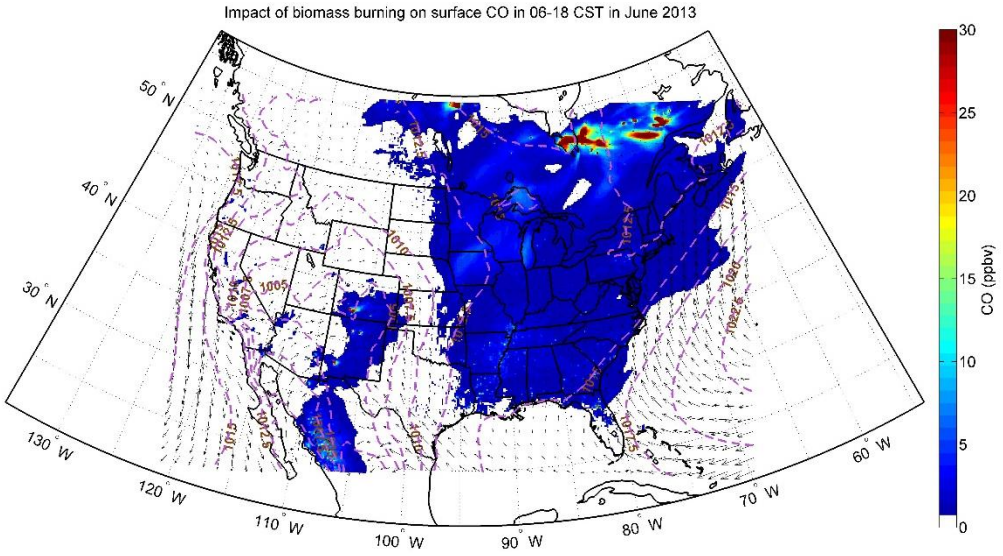

Figure 57: Effect of biomass burning on CO concentrations in June, 2013.

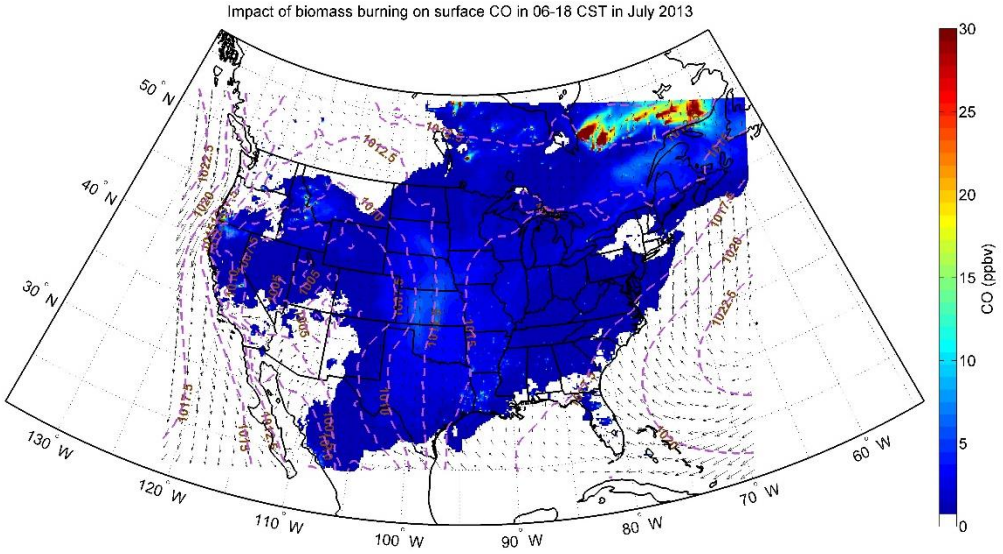

Figure 58: Effect of biomass burning on CO concentrations in July, 2013.

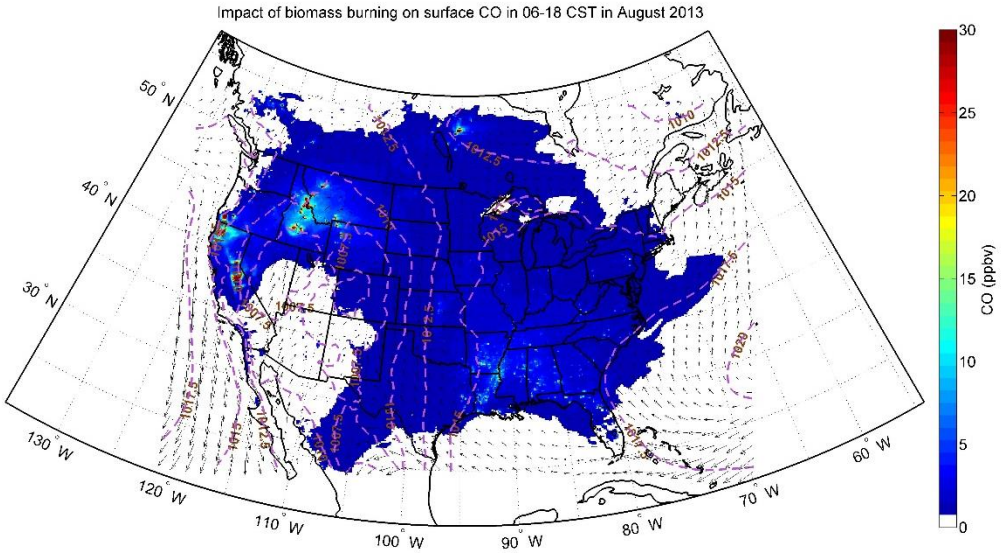

Figure 59: Effect of biomass burning on CO concentrations in August, 2013.

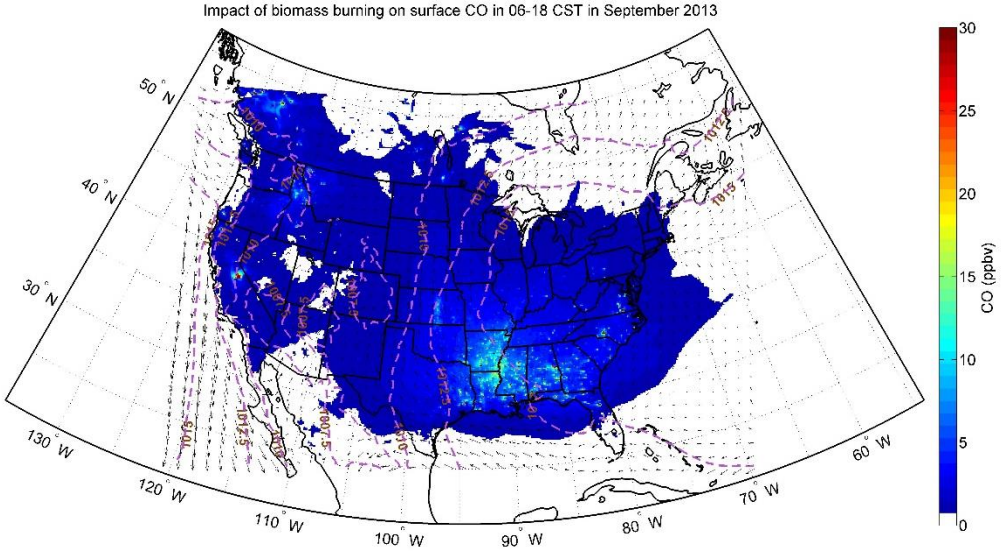

Figure 60: Effect of biomass burning on CO concentrations in September, 2013.

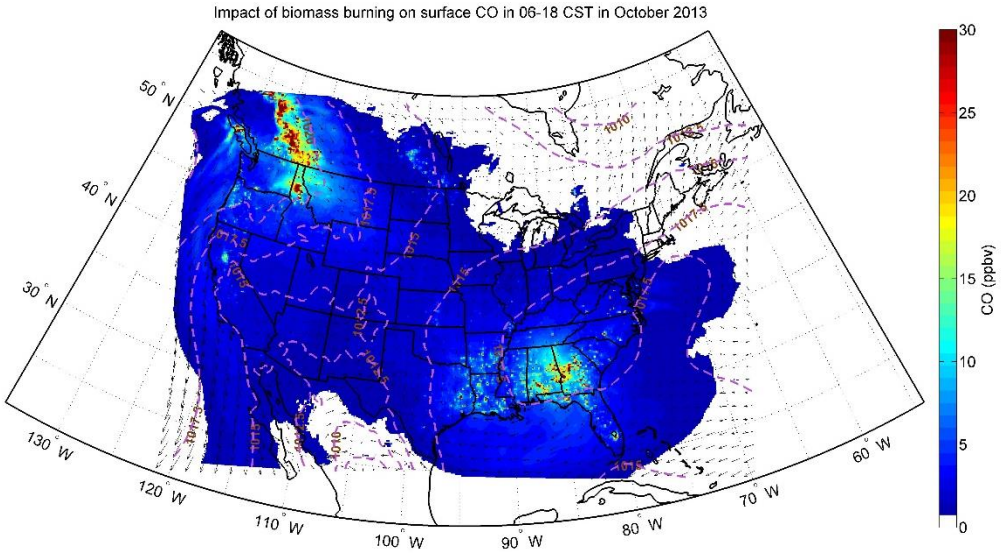

Figure 61: Effect of biomass burning on CO concentrations in October, 2013.

Ozone model-measurement comparisons and biomass burning impacts for 2014

Contour maps highlighting the comparisons and impacts due to biomass burning for the year 2014 are potted in Figures 62-68. Figure 62 plots the results for the month of April. The top panel indicates that there are several hotspots of ozone concentrations 60-70 ppb over the Western Mountain Region and in California, which are under-predicted by the model. In-situ concentrations over the eastern U.S. are quite low, ranging between 35-40 ppb and captured quite well by the model. The ozone impacts slide in the bottom panel shows that in April, biomass events caused less than 0.5 ppb of ozone change across most of the continental U.S. However, there were 1-2 ppb changes in some places such as Georgia, South Carolina, Florida and Kansas.

Comparisons and impacts for May 2014 are plotted in Figure 63, indicating in-situ hotspots of 60-70 ppb over the Western Mountain region and over California. While the model can reasonably capture the trends over the Western Mountain region, it still under-predicts in California. In-situ concentrations of ozone over the east coast range between 40-50 ppb; the model under-predicts these by 5-10 ppb. The impacts indicate less than a 0.5 ppb impact over most regions of the continental U.S., although there were 1 ppb effects in Georgia, Florida, Alabama, North and South Carolina, northern Mexico and southwestern Canada.

Figure 64 plots the impacts and comparison for June 2014. The in-situ data indicate hotspots over the Western Mountain region and California. The model is able to reasonably capture the Western Mountain hotspots but under-predicts in California. Lower ozone in-situ concentrations, ranging from 30-40 ppb are observed over the eastern U.S. The model over-predicts here quite significantly, by 10-20 ppb. The ozone impact plot in the bottom panel indicates changes of less than 0.5 ppb across the entire continental U.S.

Figure 65 depicts the results for July, 2014. In-situ concentrations were surprisingly low during this month except for California. The model reproduced the low concentrations reasonably well but under-predicted in California. The impacts of biomass burning were less than 0.5 ppb over the continental U.S. although there was a 1-2 ppb impact in southeastern Oregon, northwestern Nevada and southern Idaho.

Figure 66 plots the model-measurement contrasts and biomass impacts for the month of August in 2014. In-situ data show hotspots of 60-70 ppb in the Western Mountain region and in California. The model reasonably reproduced the Western Mountain hotspots but under-predicted in California. Ozone concentrations over the eastern U.S. were quite low during this month, ranging from 30-35 ppb. The model significantly over-predicted these numbers by 10-20 ppb. The impacts plot in the bottom panel reveals a less than 0.5 ppb increase across the continental U.S., with 1-3 ppb changes occurring in western California, central Oregon, Idaho, southwestern Canada and southern Georgia.

Figure 67 plots the model-measurement comparisons and biomass burning impacts for September, 2014. Ozone concentrations for this month were typically low across the continental U.S., except for a few hotspots in California. The model over-predicted most of these but under-predicted in California. The impact plot in the bottom panel indicates that biomass burning caused changes of less than half a ppb over the continental U.S.

In-situ data for October 2014 (Figure 68) showed low ozone concentrations all across the U.S. While these were over-predicted by the model over the western half, the model was actually able to capture the trends over the eastern U.S. reasonably well. An impact of less than 0.5 ppb due to biomass emissions was predicted over almost the entire continental U.S., although there were 1 ppb changes over Georgia, Alabama and Mississippi.

The time-series comparison for 2014 is plotted in Figures 69, 70 and 71 for the spring, summer and fall, respectively. The best correlation is predicted for summer (0.93), but the model-measurement error is quite high, indicating an over-prediction issue. The lowest model error is reported for spring.

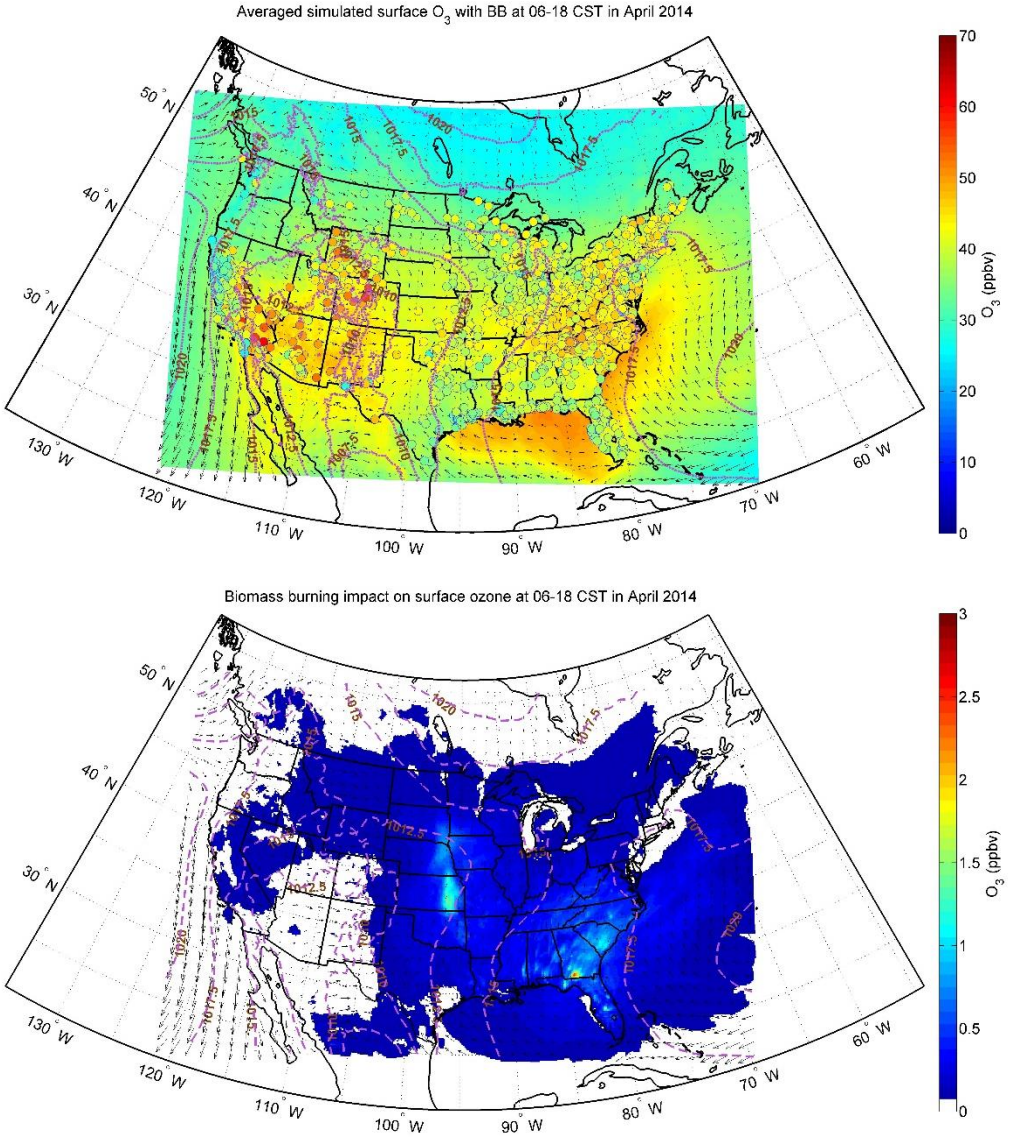

Figure 62: Ozone model-measurement comparison and biomass burning impacts for the month of April, 2014. Top panel plots the ozone concentrations with biomass burning emissions included. In-situ data are represented by circles in the top panel. The bottom panel plots the differences between the biomass case and the non-biomass one.

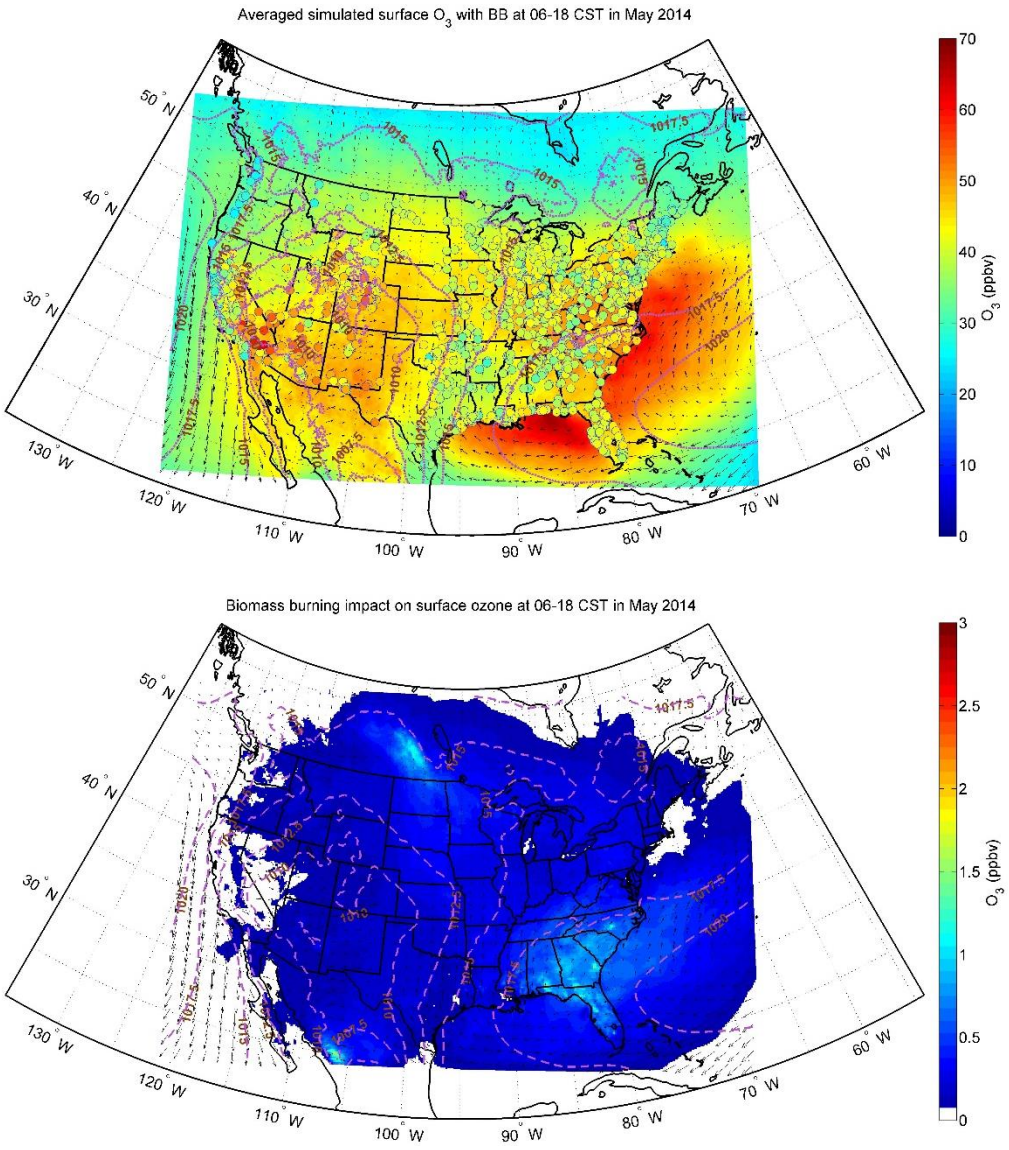

Figure 63: Ozone model-measurement comparison and biomass burning impacts for the month of May, 2014. Top panel plots the ozone concentrations with biomass burning emissions included. In-situ data are represented by circles in the top panel. The bottom panel plots the differences between the biomass case and the non-biomass one.

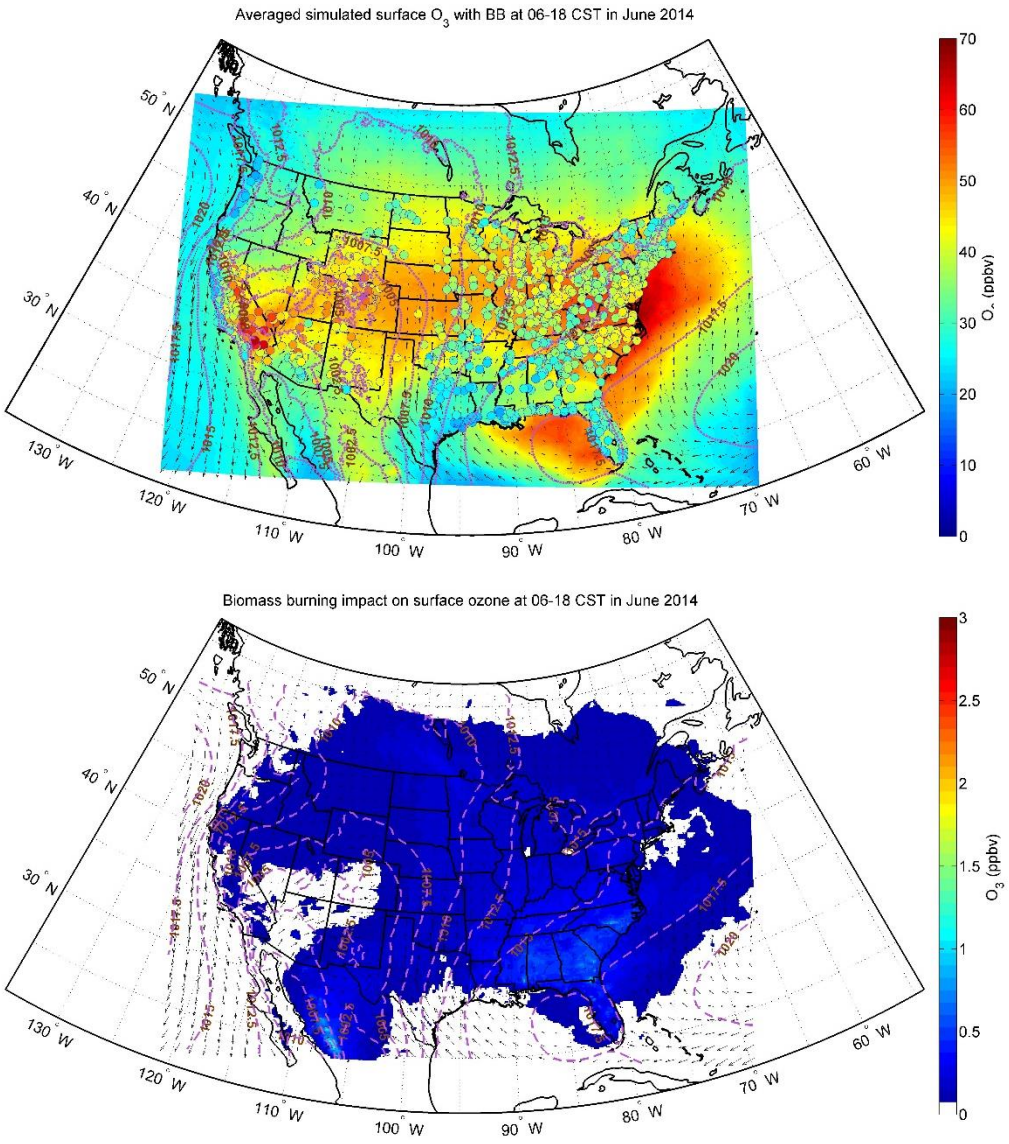

Figure 64: Ozone model-measurement comparison and biomass burning impacts for the month of June, 2014. Top panel plots the ozone concentrations with biomass burning emissions included. In-situ data are represented by circles in the top panel. The bottom panel plots the differences between the biomass case and the non-biomass one.

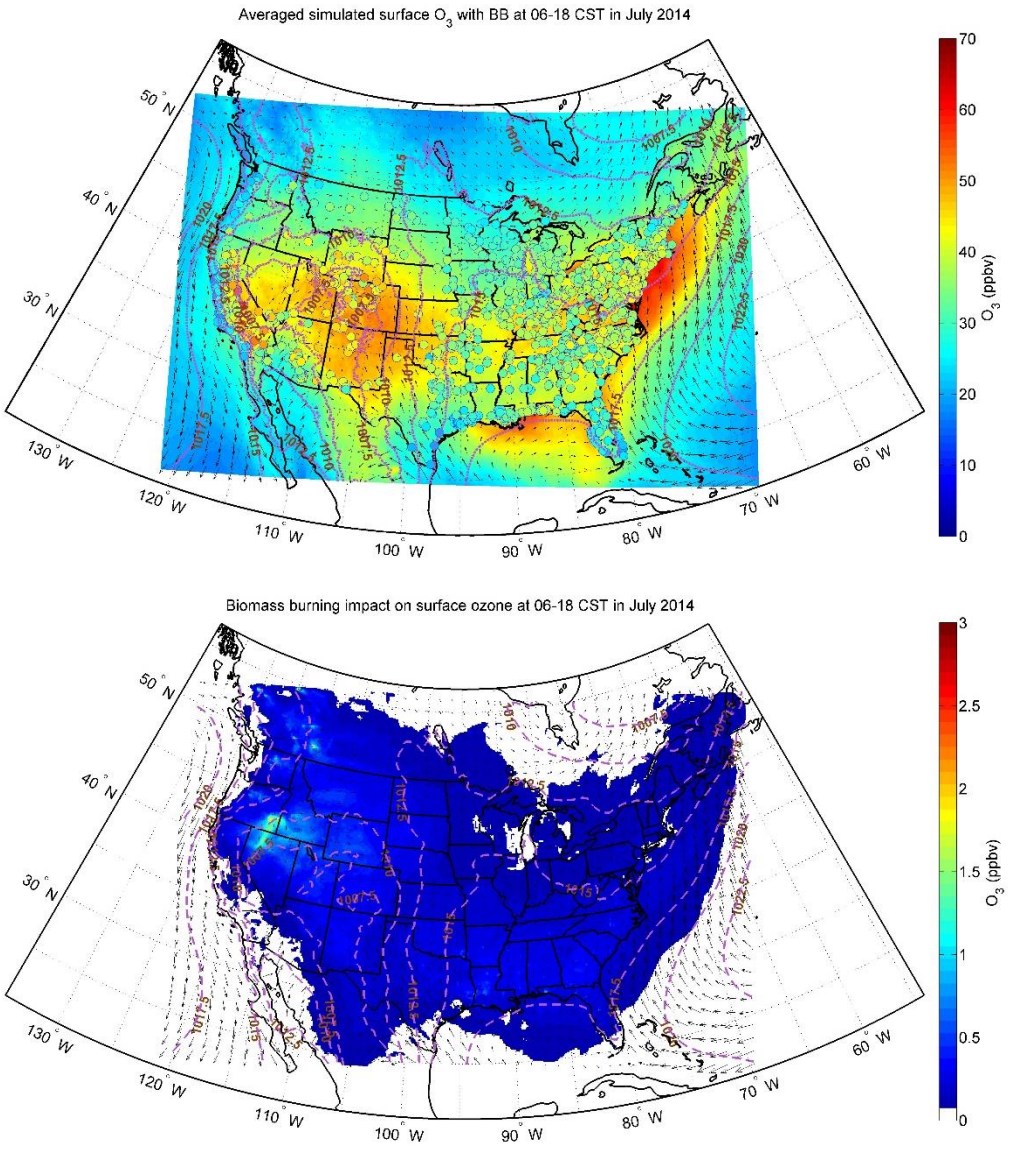

Figure 65: Ozone model-measurement comparison and biomass burning impacts for the month of July, 2014. Top panel plots the ozone concentrations with biomass burning emissions included. In-situ data are represented by circles in the top panel. The bottom panel plots the differences between the biomass case and the non-biomass one.

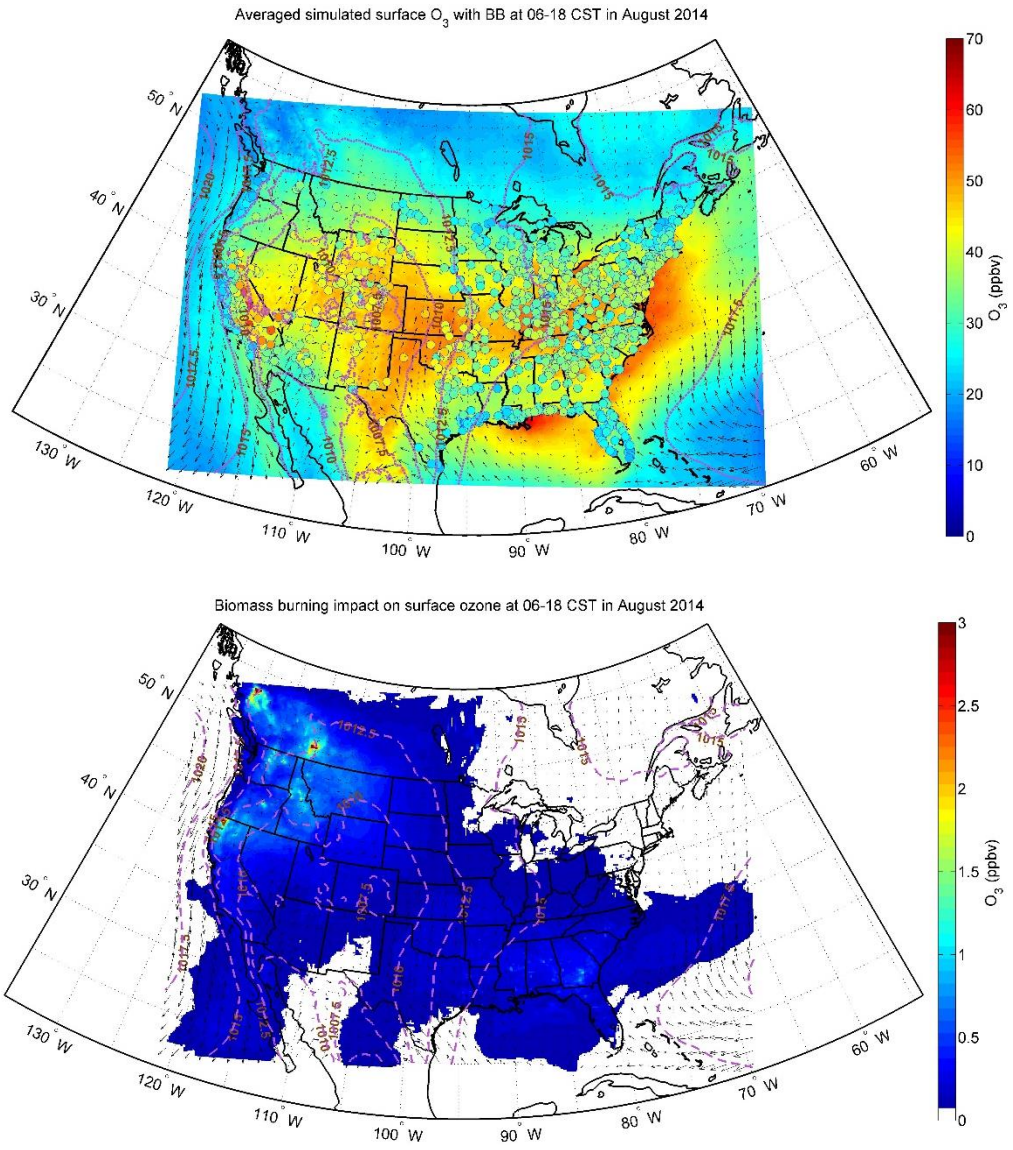

Figure 66: Ozone model-measurement comparison and biomass burning impacts for the month of August, 2014. Top panel plots the ozone concentrations with biomass burning emissions included. In-situ data are represented by circles in the top panel. The bottom panel plots the differences between the biomass case and the non-biomass one.

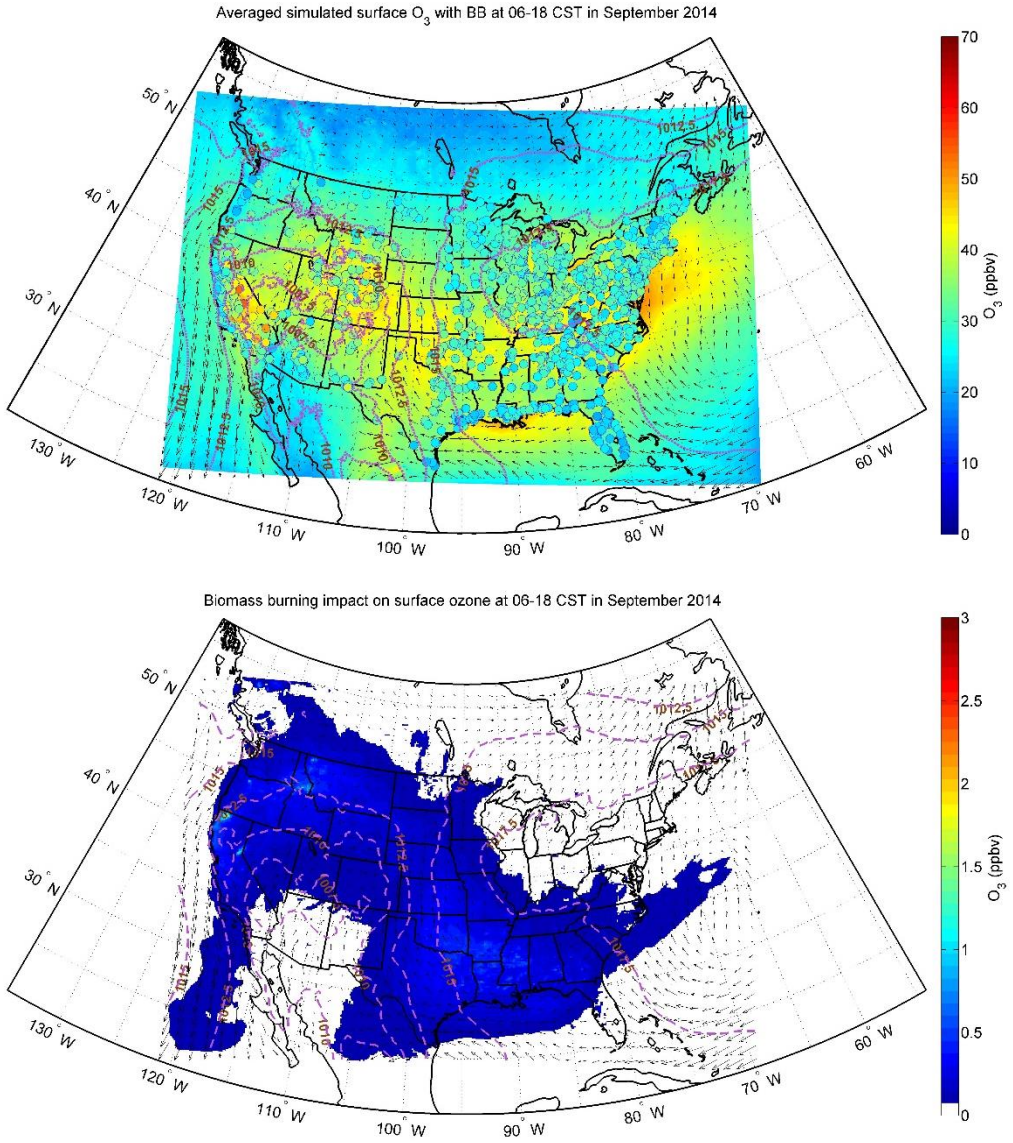

Figure 67: Ozone model-measurement comparison and biomass burning impacts for the month of September, 2014. Top panel plots the ozone concentrations with biomass burning emissions included. In-situ data are represented by circles in the top panel. The bottom panel plots the differences between the biomass case and the non-biomass one.

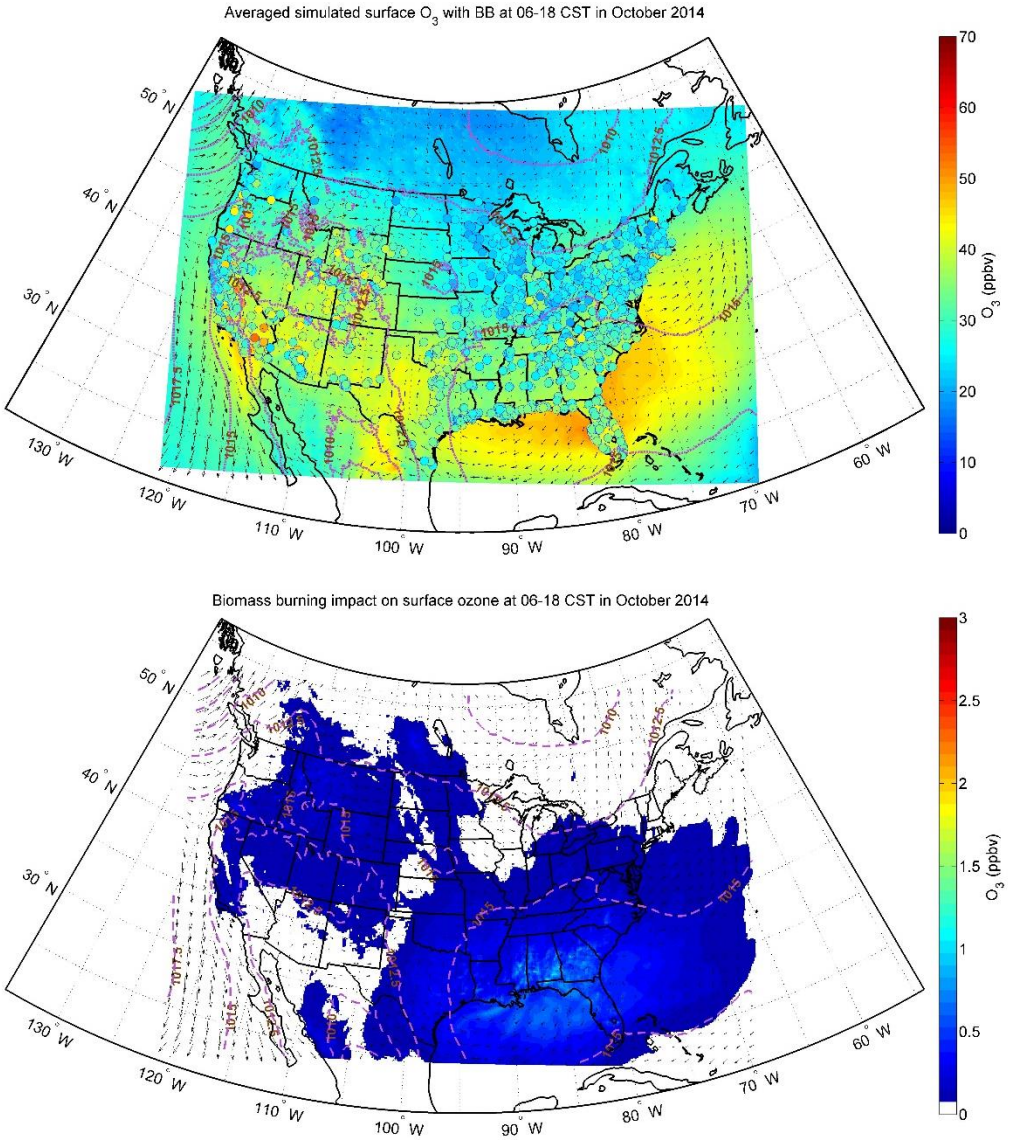

Figure 68: Ozone model-measurement comparison and biomass burning impacts for the month of October, 2014. Top panel plots the ozone concentrations with biomass burning emissions included. In-situ data are represented by circles in the top panel. The bottom panel plots the differences between the biomass case and the non-biomass one.

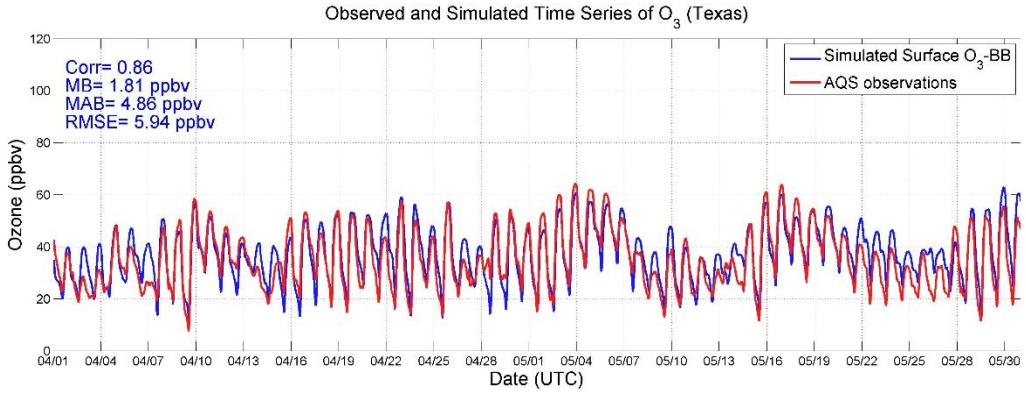

Figure 69: Ozone time series for model-measurement comparison during spring 2014 for the state of Texas

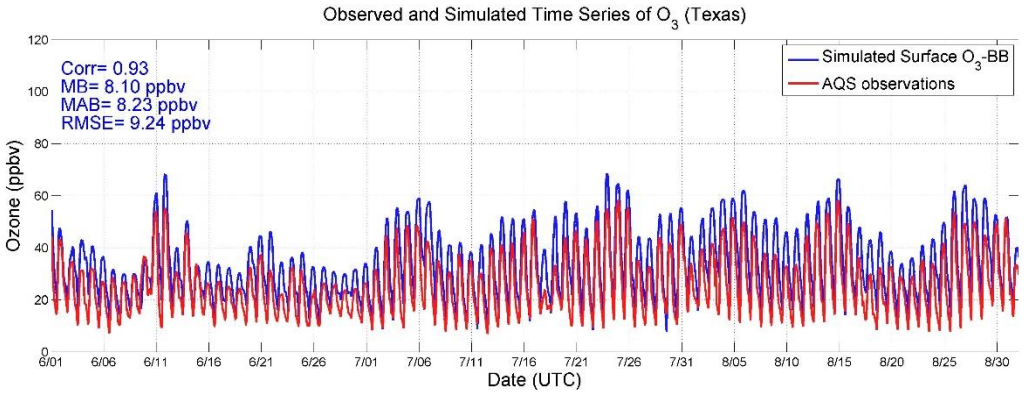

.

Figure 70: Ozone time series for model-measurement comparison during summer 2014 for the state of Texas.

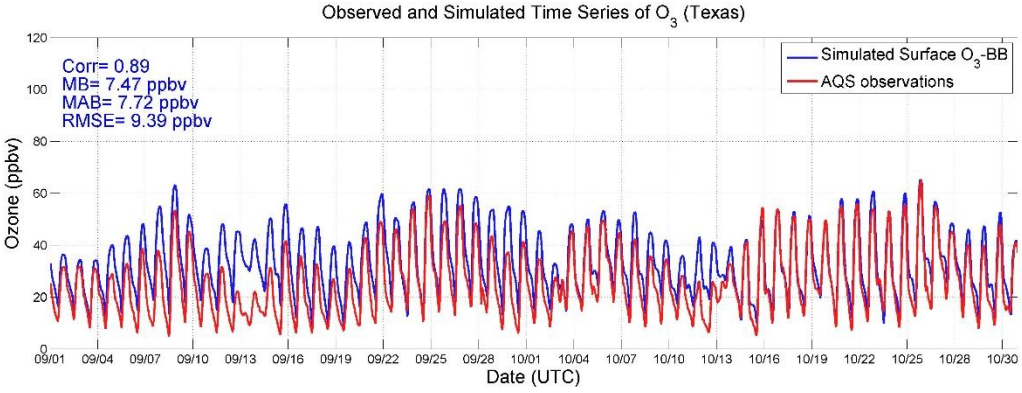

Figure 71: Ozone time series for model-measurement comparison during fall 2014 for the state of Texas.

PM2.5 model-measurement comparisons and biomass impacts for 2014

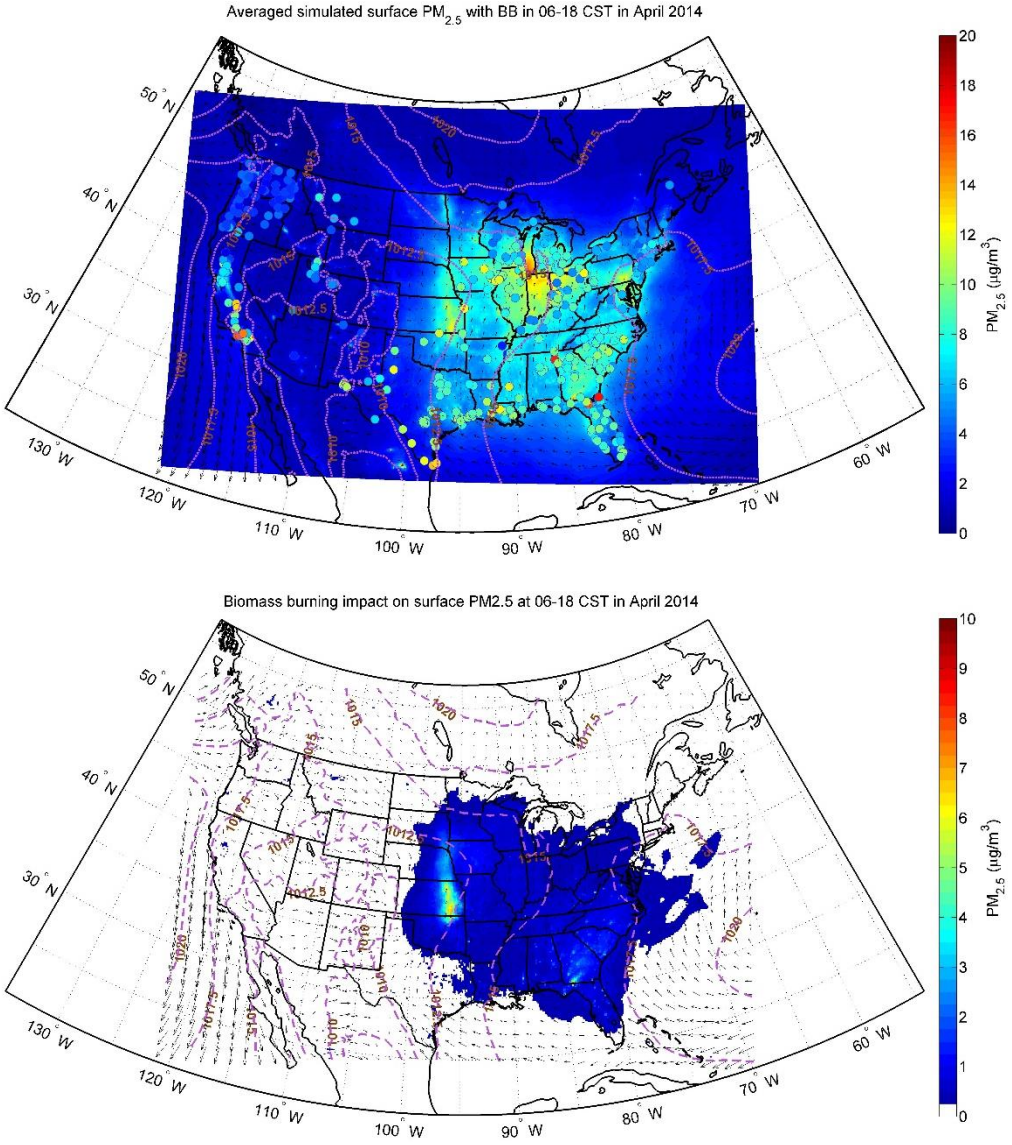

Figure 72: $PM_{2.5}$ model-measurement comparison and biomass burning impacts for the month of April, 2014. Top panel plots the ozone concentrations with biomass burning emissions included. In-situ data are represented by circles in the top panel. The bottom panel plots the differences between the biomass case and the non-biomass one.

$PM_{2.5}$ model-measurement comparisons for the month of April, 2014 are plotted in Figure 72. Elevated concentrations of ~ 10-20 μg m^{-3} are observed in the in-situ measurements over the eastern U.S. and over some stations in California. The model does a good job of reproducing concentration values less than or equal to 12 μg m^{-3} but is unable to capture higher ones. The impacts of biomass burning on $PM_{2.5}$ concentrations is plotted in the bottom panel, where we find that biomass burning emissions cause a change of ~ 1 across the eastern U.S., with higher impacts of 5-6 μg m^{-3} predicted over the Midwest. Plots for the month of May, 2014 tell a similar story;

the impacts plot predicts a 1 μg m^{-3} enhancement over the southeastern U.S., certain parts of the Midwest, southern Canada and northern Mexico.

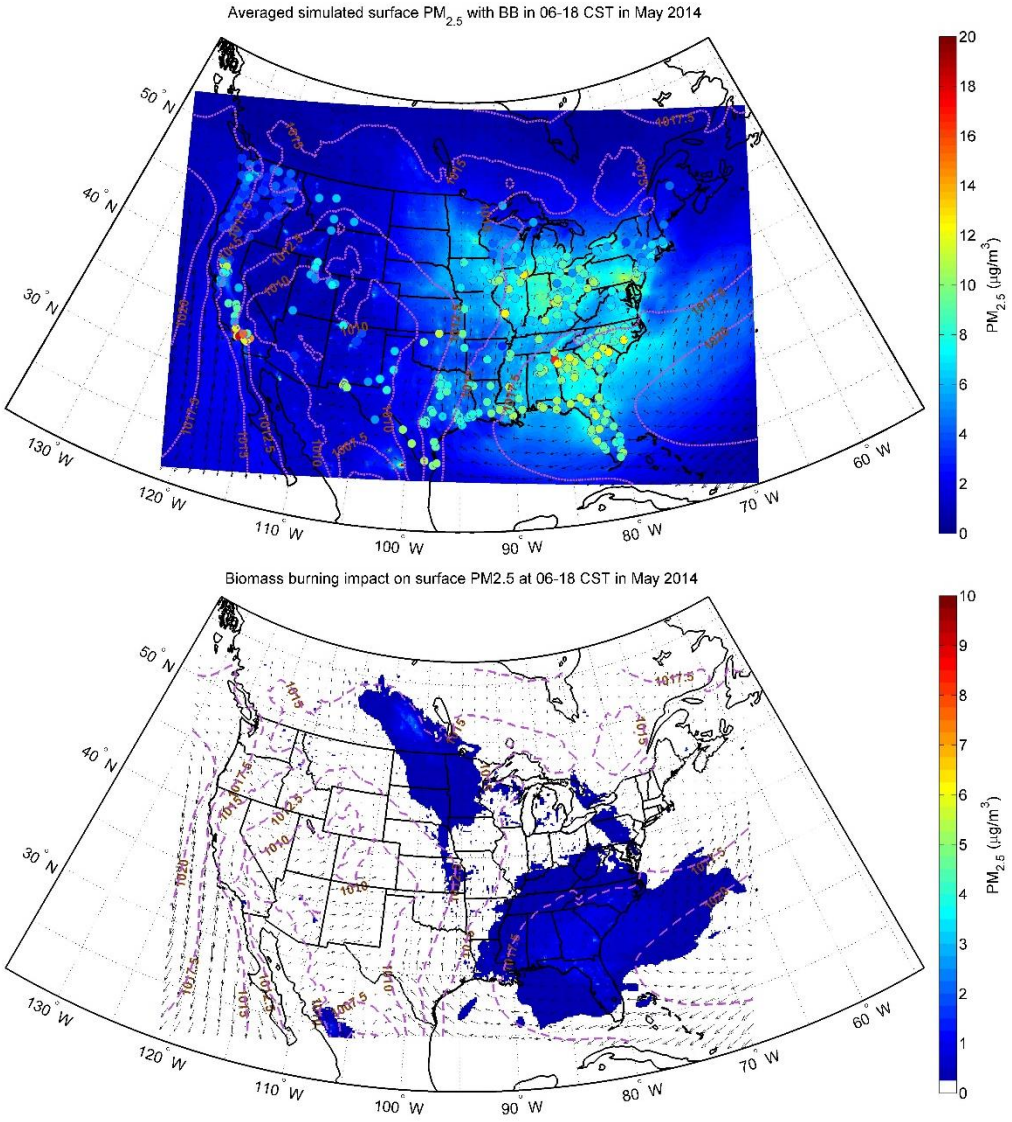

Figure 73: $PM_{2.5}$ model-measurement comparison and biomass burning impacts for the month of May, 2014. Top panel plots the ozone concentrations with biomass burning emissions included. In-situ data are represented by circles in the top panel. The bottom panel plots the differences between the biomass case and the non-biomass one.

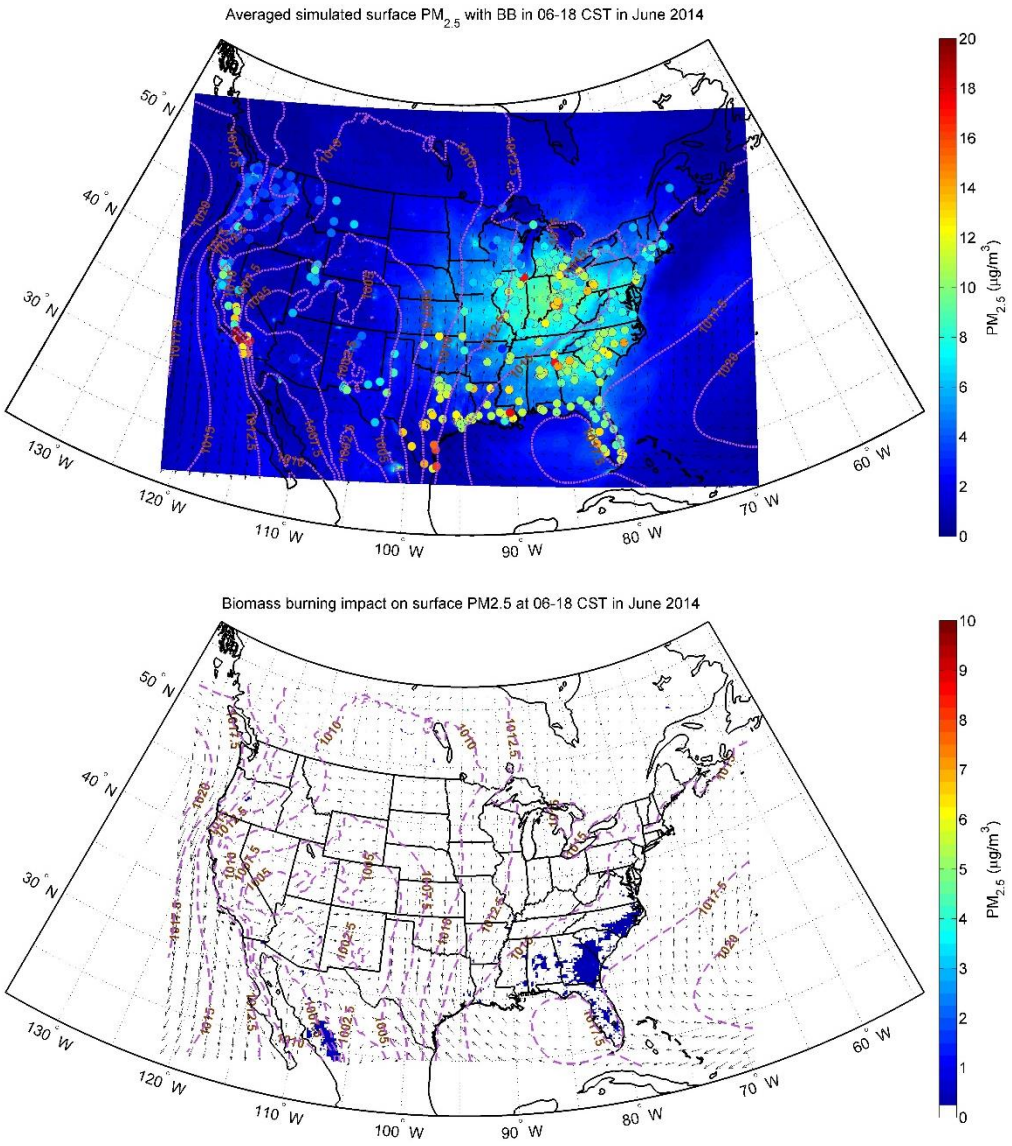

Figure 74: $PM_{2.5}$ model-measurement comparison and biomass burning impacts for the month of June, 2014. Top panel plots the ozone concentrations with biomass burning emissions included. In-situ data are represented by circles in the top panel. The bottom panel plots the differences between the biomass case and the non-biomass one.

Comparisons and impacts for the month of June, 2014 are plotted in Figure 74. In-situ data show elevated concentrations over the eastern U.S. and west coast which the model is clearly unable to reproduce, under-predicting everywhere. The impacts slide in the bottom panel indicates that there was hardly any $PM_{2.5}$ impact due to biomass burning in June 2014, with a 1 μg m^{-3} change predicted in some parts of Georgia, South Carolina, Florida and Mexico. A similar story is told by the July 2014 comparison and impacts plot in Figure 75. For this month, impacts of 1 μg m^{-3} were predicted in Louisiana, northern Nevada, southern Idaho, northern Washington and southwestern Canada.

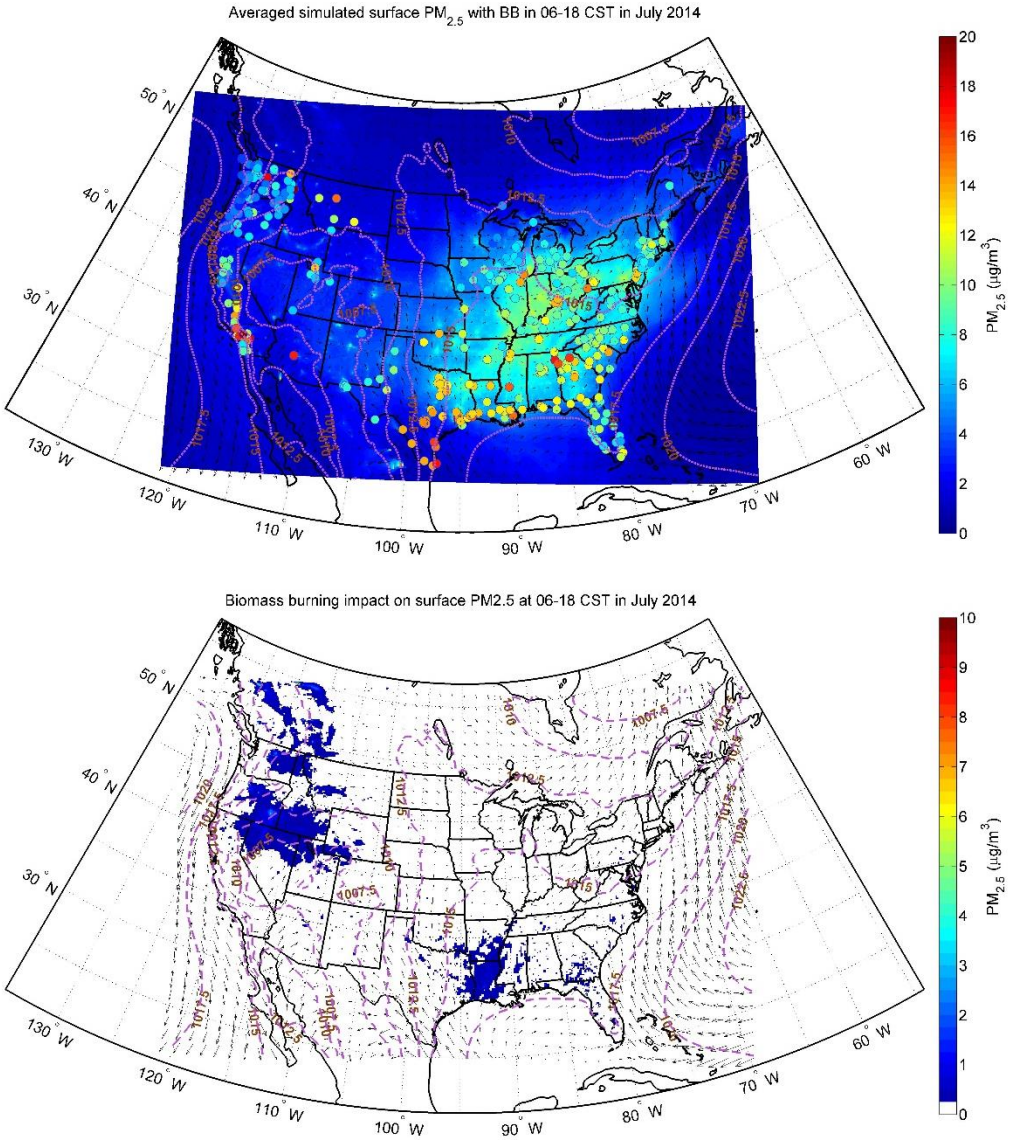

Figure 75: $PM_{2.5}$ model-measurement comparison and biomass burning impacts for the month of July, 2014. Top panel plots the ozone concentrations with biomass burning emissions included. In-situ data are represented by circles in the top panel. The bottom panel plots the differences between the biomass case and the non-biomass one.

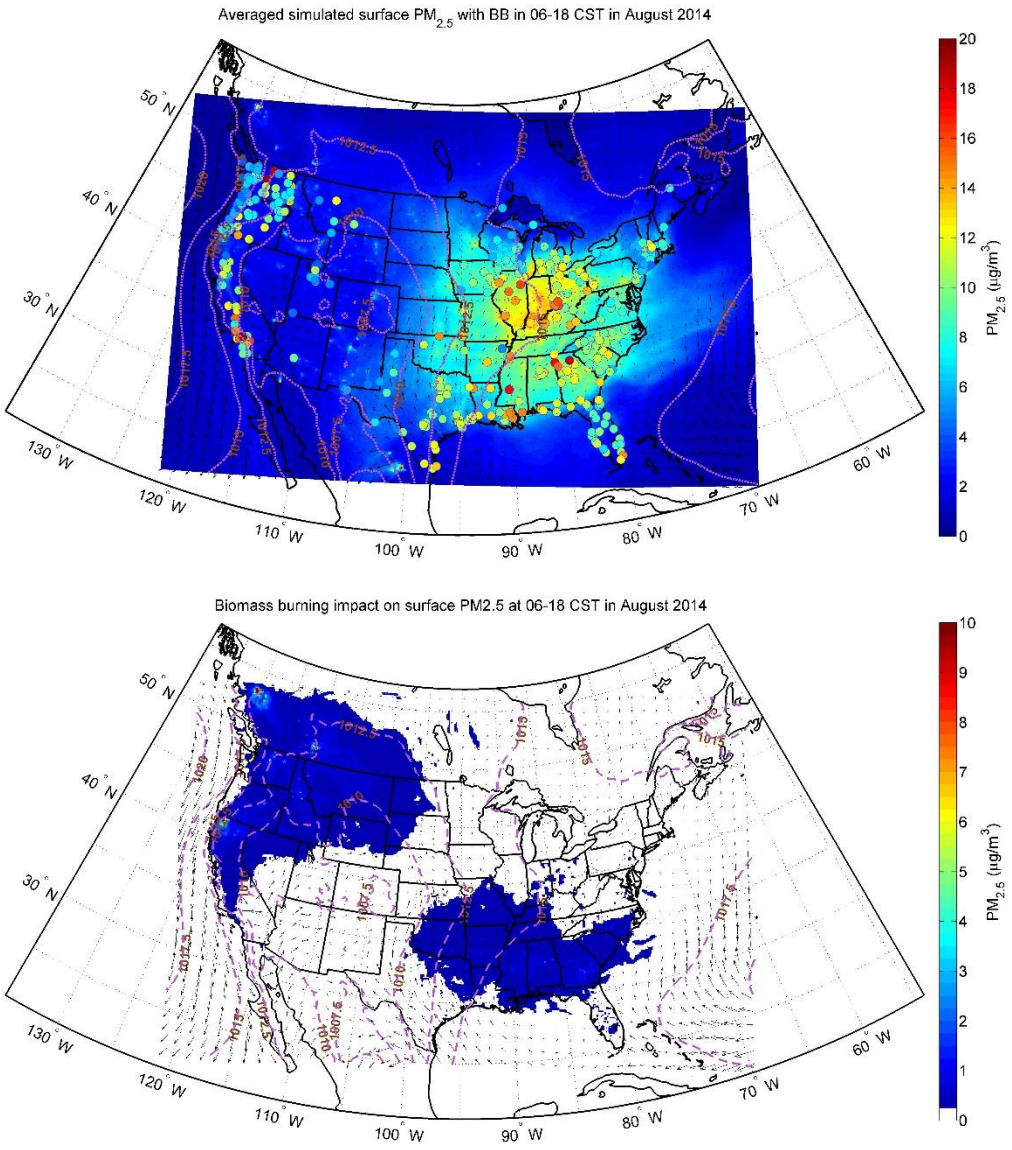

Figure 76: $PM_{2.5}$ model-measurement comparison and biomass impacts for the month of August, 2014. Top panel plots the ozone concentrations with biomass burning emissions included. In-situ data are represented by circles in the top panel. The bottom panel plots the differences between the biomass case and the non-biomass one.

Comparisons and impacts for the month of August, 2014 are plotted in Figure 76. Hotspots are observed for the in-situ data all over the Pacific coast, and the model under-predicts at all of these places. There are several hotspot regions over the eastern U.S., but the model only captures those in Indiana and Illinois, under-predicting elsewhere. The impacts map predicts a 1 μg m^{-3} change over the southern states of Georgia, North and South Carolina, Alabama, Mississippi, Louisiana, northern Texas, Oklahoma, Missouri, Arkansas and Tennessee; and also over northern California, Washington, Oregon, Idaho, Wyoming and Nevada. The model evaluation plots for September and October 2014 conveys a similar message in Figure 77 and 78 respectively. Here, an impact of 1 μg m^{-3} is predicted over almost the entire continental U.S. However, the $PM_{2.5}$ concentrations in October were significantly lower over the eastern U.S. as compared to September.

The time series for the fall season of 2014 for the state of Texas is plotted in Figure 79. The correlation and mean bias are reasonable (R=0.65 and MB=0.86 μg m^{-3}); statistics for the other regions were quite poor, hence not reported here.

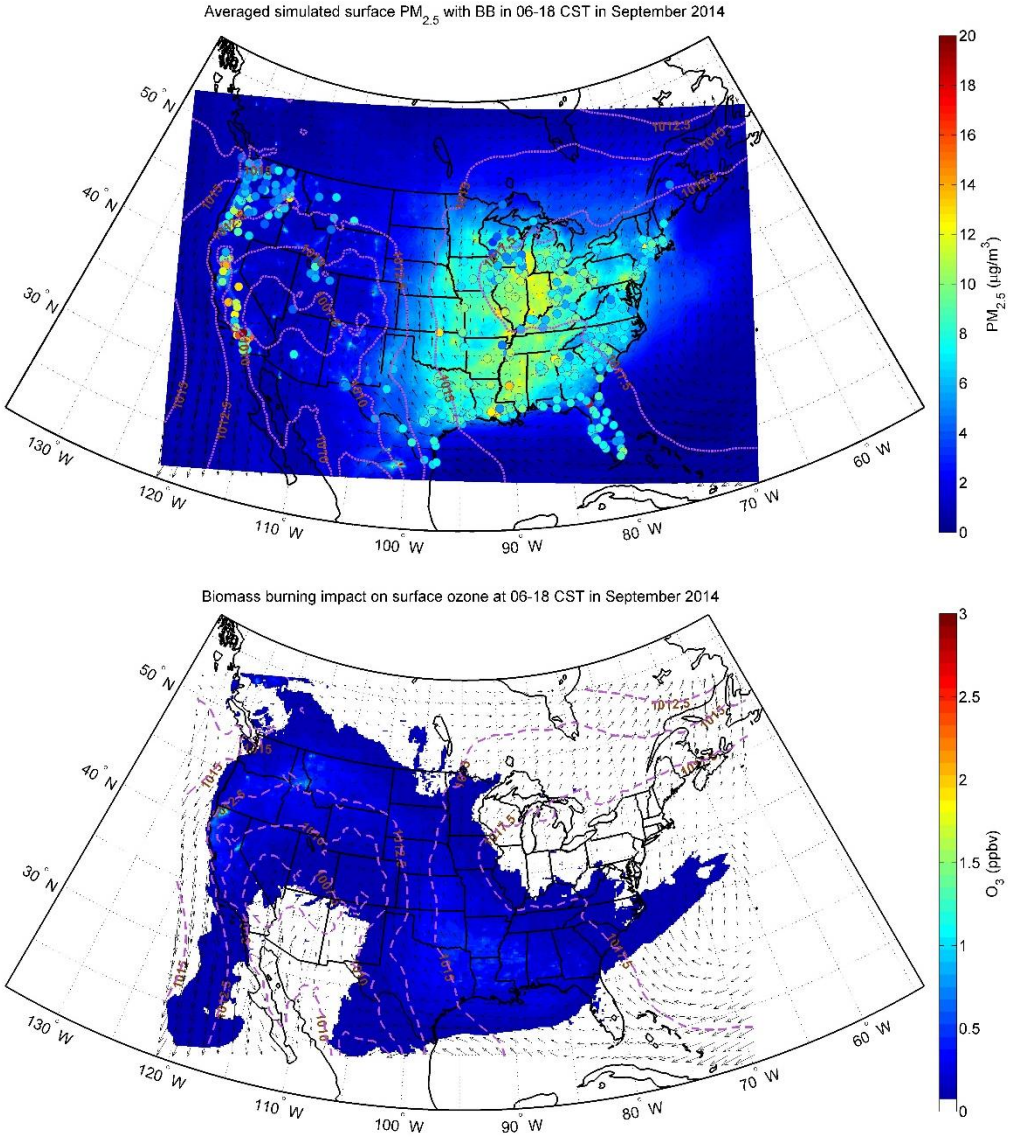

Figure 77: $PM_{2.5}$ model-measurement comparison and biomass burning impacts for the month of September, 2014. Top panel plots the ozone concentrations with biomass burning emissions included. In-situ data are represented by circles in the top panel. The bottom panel plots the differences between the biomass case and the non-biomass one.

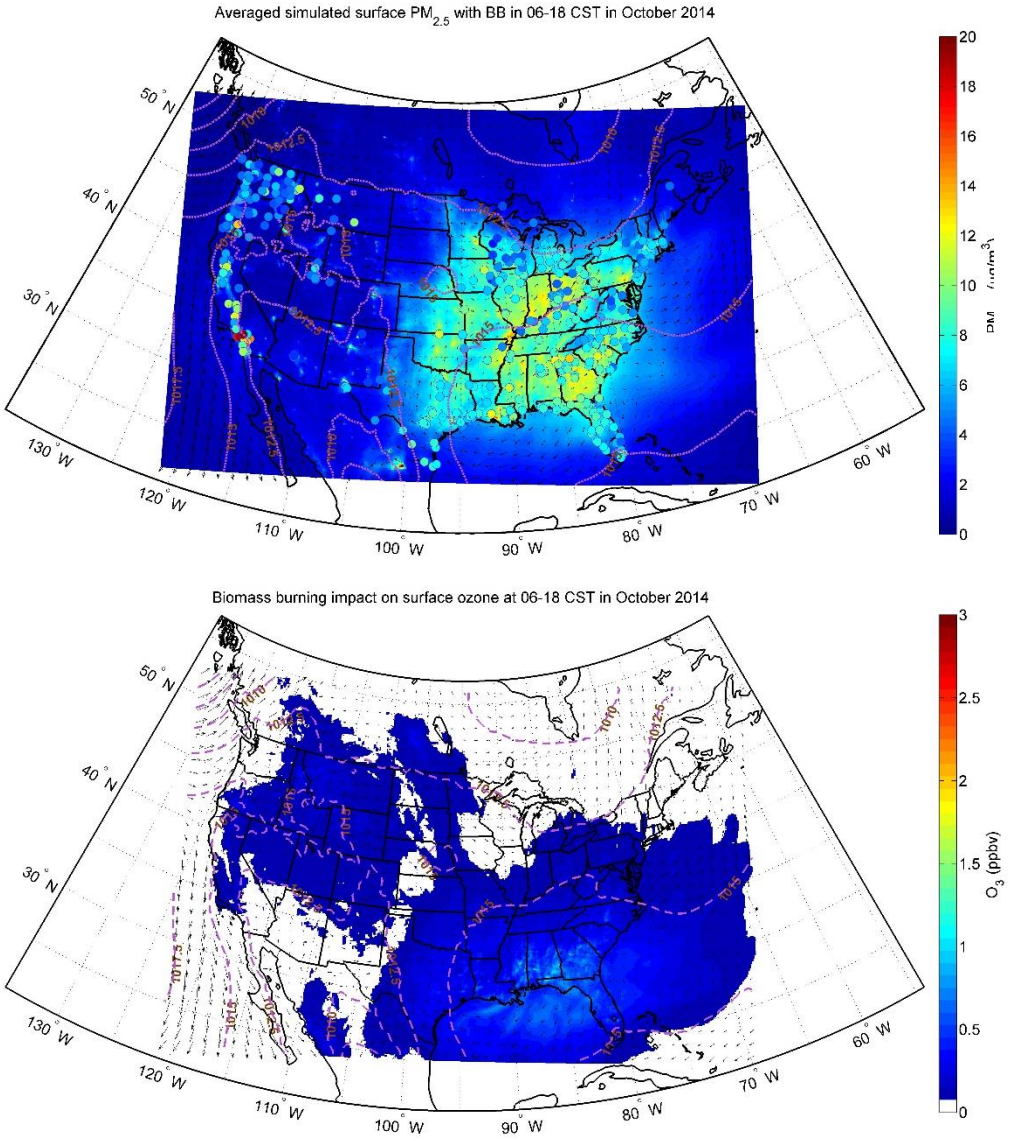

Figure 78: $PM_{2.5}$ model-measurement comparison and biomass burning impacts for the month of October, 2014. Top panel plots the ozone concentrations with biomass burning emissions included. In-situ data are represented by circles in the top panel. The bottom panel plots the differences between the biomass case and the non-biomass one.

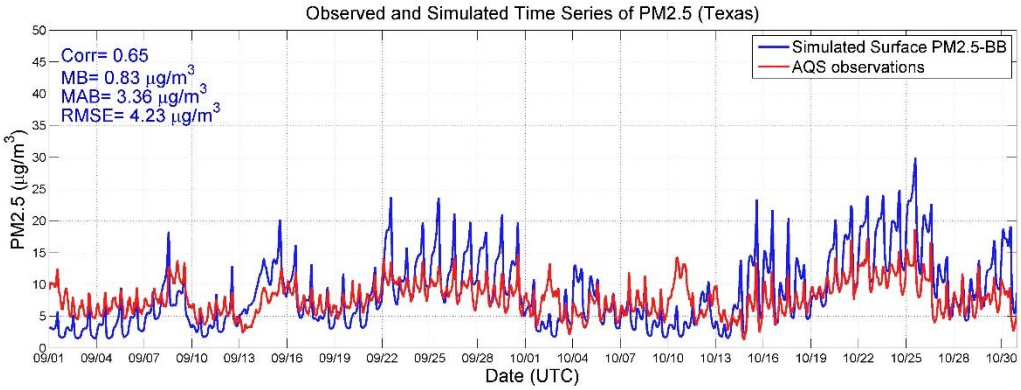

Figure 79: $PM_{2.5}$ time series for model-measurement comparison during fall 2014 for the state of Texas.

CO biomass burning impacts for 2014

The CO enhancements over the continental U.S. due to biomass burning during the summer ozone season of 2014 are plotted in Figures 80-86. In Figure 80, the model predicts that biomass burning emissions will add 15-30 ppb of CO in the Midwest, Georgia, South Carolina and Florida, in addition to a uniform 5 ppb enhancement across the eastern half of the U.S. The plot for May 2014 in Figure 81 indicates that a uniform 5 ppb is added across the eastern U.S., in addition to some parts of Mexico and Canada. Also, a 15 ppb change is noticed in south-central Canada. The plot for June 2014 in Figure 82 indicates that only the southeastern U.S. and northern Mexico experience a 5 ppb enhancement due to biomass emissions. The plot for July 2014 in Figure 83 indicates that in addition to the southeastern U.S., an enhancement of 5 ppb is also predicted for most of the western U.S. The plot for August in Figure 84 shows that a 5 ppb change is predicted across almost the entire continental U.S., in addition to changes up to 30 ppb in northwestern Washington. The plot for September in Figure 85 indicates that a 5 ppb increase is predicted across the entire continental U.S. except for some parts of Texas, Utah, Colorado and the entireties of New Mexico and Arizona. The plot for October 2014 in Figure 86 shows that a 5 ppb increase is predicted over almost the entire eastern U.S. and Pacific coast as well as southwestern Canada. Additionally, increases of 15-20 ppb are predicted for eastern Texas, Arkansas, Louisiana, Mississippi, Alabama, Georgia and Florida.

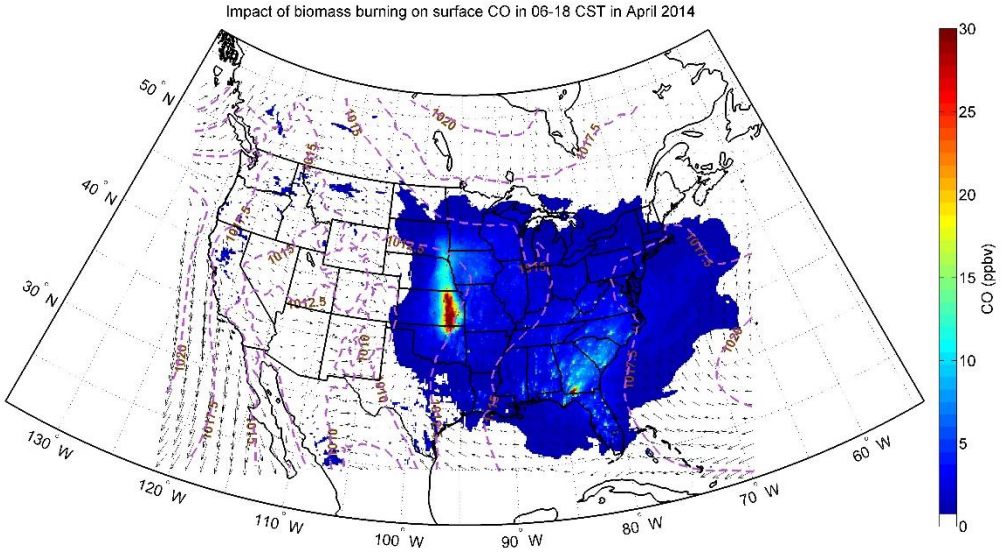

Figure 80: Effect of biomass burning on CO concentrations in April, 2014.

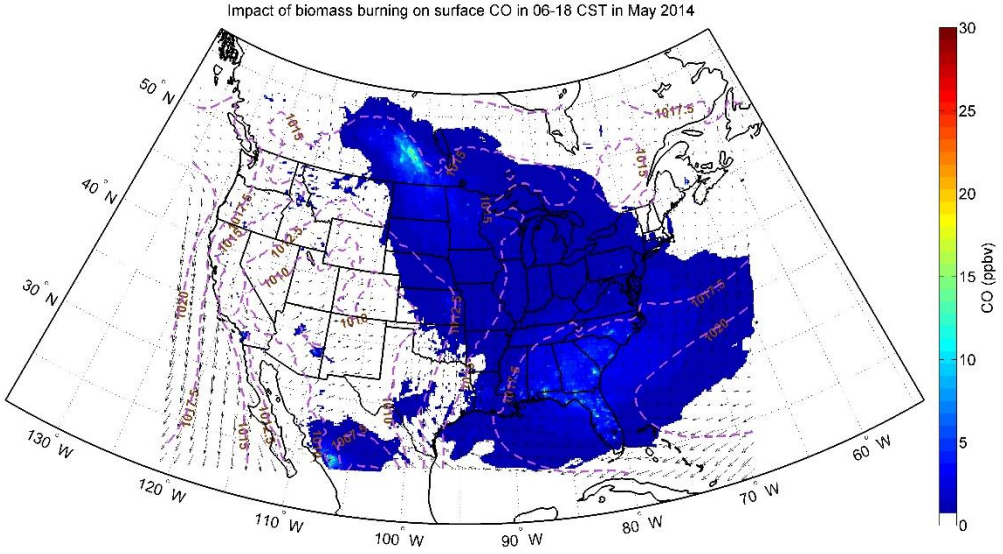

Figure 81: Effect of biomass burning on CO concentrations in May, 2014.

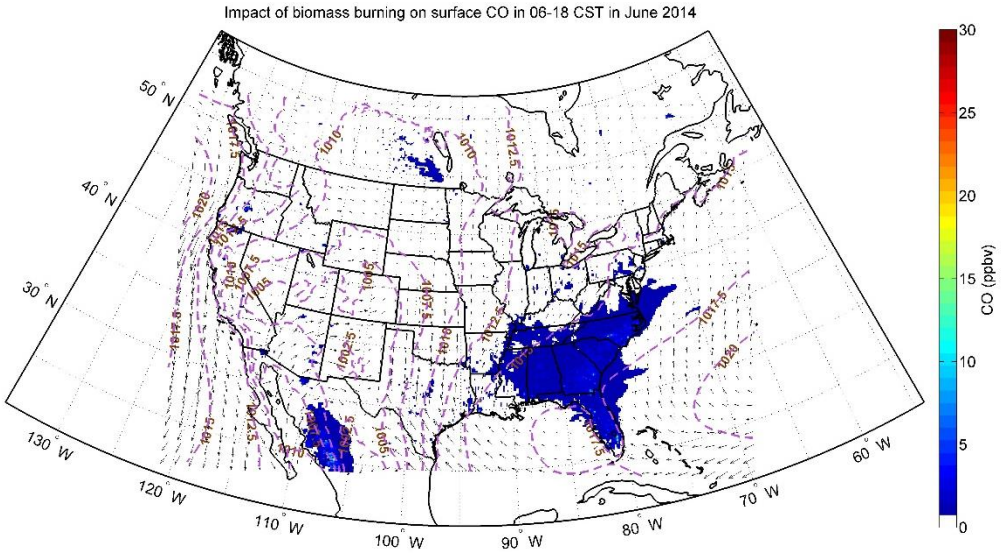

Figure 82: Effect of biomass burning on CO concentrations in June, 2014.

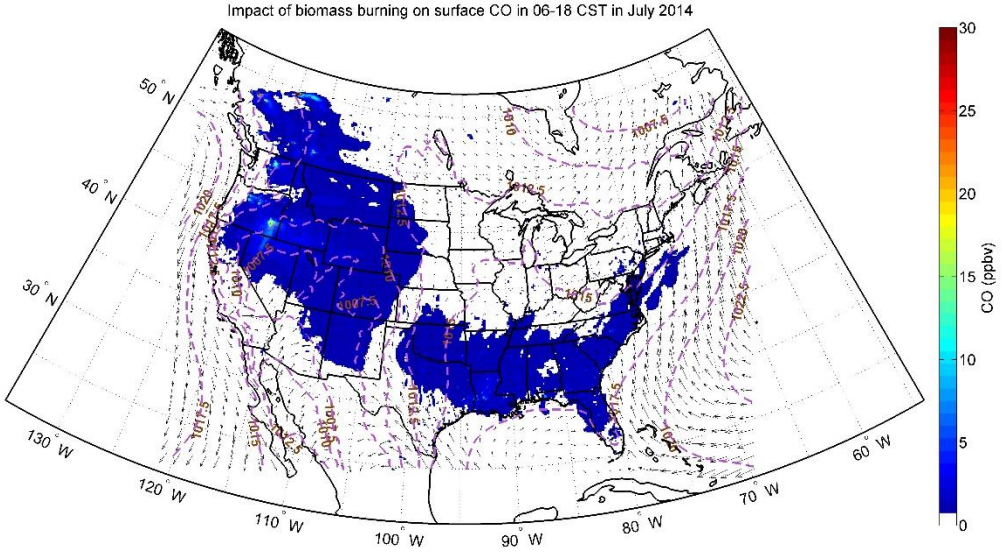

Figure 83: Effect of biomass burning on CO concentrations in July, 2014.

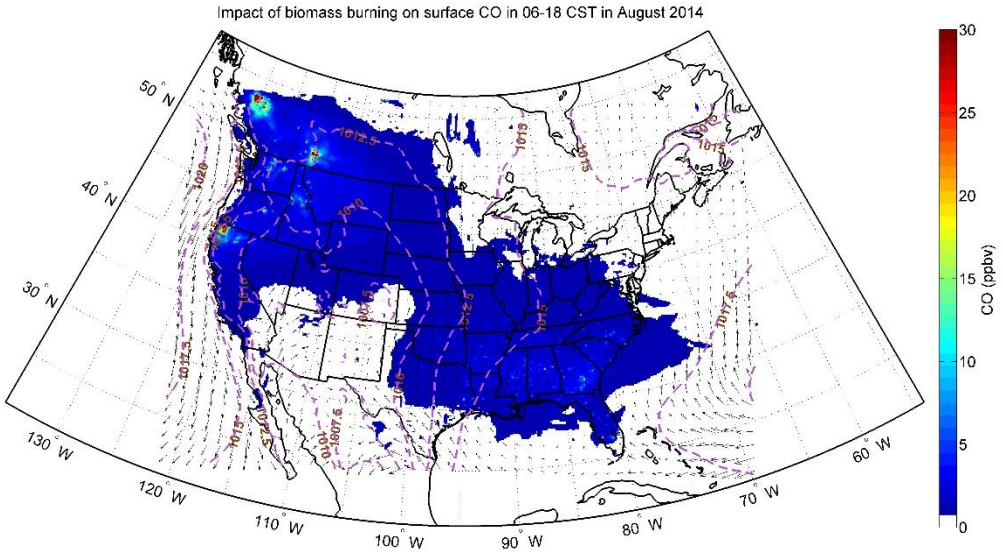

Figure 84: Effect of biomass burning on CO concentrations in August, 2014.

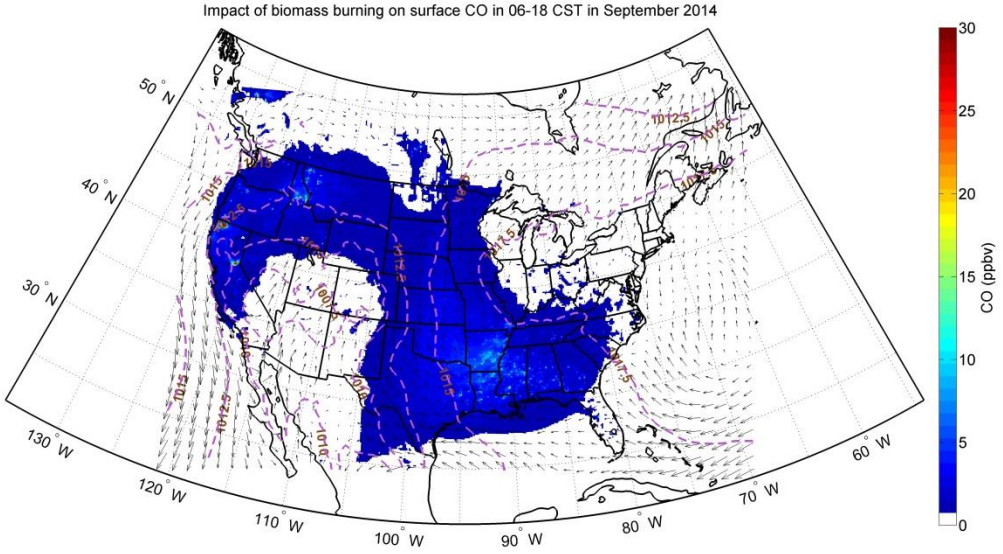

Figure 85: Effect of biomass burning on CO concentrations in September, 2014.

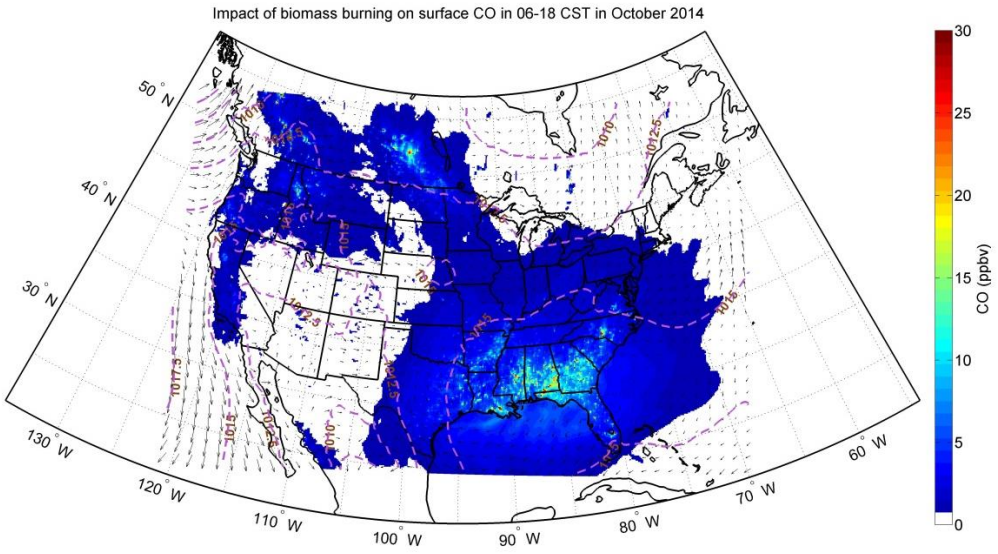

Figure 86: Effect of biomass burning on CO concentrations in October, 2014.

Summary and Conclusions

The NCAR's FINN biomass burning inventory (Wiedinmyer et al., 2011) was used in conjunction with the CMAQ chemical transport model and the WRF meteorological model to assess the impact of biomass burning emissions on ozone, particulate matter and carbon monoxide concentrations over the continental U.S. The simulation episodes chosen were the summer ozone seasons of three years: 2012, 2013 and 2014. In this space, other anthropogenic emissions fields were provided by the SMOKE model. Biogenic emissions were modeled using BEIS. We chose BEIS over MEGAN since previous studies (e.g., Kota et al., 2015; Warneke et al., 2010) indicated that CMAQ modeling using MEGAN over-predicted concentrations of several biogenic VOCs such as isoprene. The FINN VOC emissions were speciated for the MOZART mechanism; these had to be re-mapped to CB05, which is the mechanism used for our CMAQ model. Additionally, the resolution of the FINN inventory was 1-km, which had to be re-gridded to 12 km. We also re-distributed the emissions vertically. Observational data were taken from TCEQ's CAMS and EPA's AQS networks. This study has marked improvements over the previous biomass burning evaluations, which are as follows:

a) A previous study (TCEQ-AQRP Project 14-011) which built the FINN inventory produced air quality model runs for a 45-day simulation episode (May 16-June 30, 2012). This study extended that by doing a model evaluation for the summer ozone seasons of three years.

b) The regional CTMs such as CMAQ model hitherto used static chemical boundary conditions – i.e. these showed no diurnal variation. We generated updated chemical boundary conditions using the global GEOS-Chem model, which were more physically relevant since they showed certain diurnal trends. Since the vertical diurnal profile of the GEOS-Chem output extends up to 80 km, it could be also used to improve the ozone vertical profile derived from stratospheric transport of ozone.

c) Previous studies in our group (Li et al., 2016; Jeon et al., 2015) indicated that improving modeled meteorological fields using methods such as grid nudging and objective analysis could help improve air quality modeling for ozone and $PM_{2.5}$. Following that, we used grid nudging for our current 3-year simulation run.

d) Previous biomass burning studies using the CMAQ modeling used a parameterized version of plume height rise developed by WRAP. We noticed this parameterized version did not exhibit physically relevant trends; for example there was no residual height at night. Hence we used the WRF-Chem plume rise module which showed better trends for nighttime plume height rise.

Model-measurement comparisons and biomass burning impacts of ozone

For evaluation and analysis, we divided our simulation to spring (April-May), summer (June-August), and fall (September-October) seasons. During 2012, broadly, in-situ data showed ozone hotspots of 60-70 ppb across the Western Mountain region and in California, which the model did a good job reproducing. In-situ data for May 2012, showed that in addition to the Western Mountain region and California, there were a couple of hotspots over Ohio and Pennsylvania in the northeast with ozone concentrations around 60 ppb. The model did a good job of capturing these hotspots. Biomass burning emissions caused a change of 1-2 ppb predicted across northern Mexico for this month.

Observations for June and July 2012 indicated several 60-70 ppb hotspots in the Western Mountain, Midwest, East North Central and Northeastern Regions, which the model captures quite well. However, it is unable to capture the hotspots higher than 70 ppb which are observed in Central California. Biomass fires during this period added ~ 1 ppb of ozone in northern Mexico in June, and more than 3 ppb in southern Canada, with a 1 ppb impact extending over a large region there. The August forest fires in Idaho and California added 1-3 ppb ozone in these areas, with a 1-ppb impact crossing state borders. In-situ ozone concentrations in September on average were low (30-40 ppb) across the continental U.S., except for California. Surprisingly, the model over-predicted most of the low ozone across the country but under-predicts the high ozone in California. The reasons behind the under-prediction in California are still unknown and being investigated. Time series comparisons for the state of Texas indicated that overall, the model-measurement comparison demonstrates a very good correlation across all seasons, indicating that the model is able to capture the spatio-temporal trends of the in-situ data.

Similar to 2012, in-situ data for 2013 again showed hotspots over the Western Mountain region and California. The model was able to capture the hotspots over the Western Mountain region for a couple of the months (July and August) but consistently under-predicted in California. Also, in-situ data over the eastern half of the U.S. showed quite low concentrations, 30-40 ppb. The model significantly under-predicted these in the spring month of May, and over-predicted in September; capturing these trends reasonably well in the other months. Biomass burning emissions caused a 1 ppb change at the border of Georgia and Florida in April and May. Additionally, a 1 ppb change was predicted over northern Mexico in May.

Wildfire impacts in June caused changes of 1-3 ppb in northern Mexico and southeastern Canada, along with 1 ppb in Florida, New Mexico and Colorado. Biomass impacts in August indicated changes of ~ 2 ppb in Idaho and northern California, with 1 ppb impacts predicted for Louisiana,

Arkansas and Georgia. Impacts of ~ 1 ppb in Alabama, Arkansas, Louisiana, and eastern Texas, and 2-3 ppb impact in northeastern California were predicted for September of 2013. In October, a 1 ppb change was predicted over Alabama, Georgia, Idaho, Wyoming and southern Canada. The time series comparisons for Texas show a good correlation in spring (0.81), but excellent correlation in summer and fall (0.93 and 0.92 respectively). However, the model tends to over-predict more than 2012. Over-prediction could potentially be due to combined problems in emissions and meteorological fields, as indicated in a submitted manuscript by Pan et al. this year.

Similar to 2013, in-situ data for 2014 again showed ozone hotspots over the Western Mountain region and in California. While the model was able to capture the hotspots over the Western Mountain region, it once again under-predicted in California. Additionally, the eastern U.S. showed low concentrations of ozone overall during the ozone season, 30-40 ppb. The model reproduced these reasonably well in April, July and October; significantly under-predicting these in May by 5-10 ppb and over-predicting in June and August by 10-20 ppb. The reason behind these discrepancies is currently unknown but is being investigated in a current paper. The time series comparison reported the highest over-prediction for the three years.

For the month of April 2014, the model predicted 1-2 ppb changes in some places such as Georgia, South Carolina, Florida and Kansas; while 1 ppb effects in Georgia, Florida, Alabama, North and South Carolina, northern Mexico and southwestern Canada were predicted for May, and minimal impacts for June 2014. The model predicted a 1-2 ppb impact in southeastern Oregon, northwestern Nevada and southern Idaho during July 2014, while in August, 1-3 ppb changes occurred in western California, central Oregon, Idaho, southwestern Canada and southern Georgia. Minimal changes were predicted in September but 1 ppb changes over Georgia, Alabama and Mississippi were modeled for October.

Model-measurement comparisons and biomass burning impacts of $PM_{2.5}$

Broadly in 2012, the model was unable to capture the high $PM_{2.5}$ concentrations across the continental U.S. For example, in-situ data for April 2012 indicate concentrations of 10-12 μg m^{-3} all across the eastern U.S., including southeastern Texas. Additionally, there are a couple of places in Georgia, New Mexico and California where the in-situ $PM_{2.5}$ concentration was greater than 20 μg m^{-3}. The model under-predicted in most of these places but is broadly able to capture the spatial variations across the eastern U.S. However, it is unable to capture the extreme events that result in $PM_{2.5}$ concentrations greater than 20 μg m^{-3}. It will be interesting to understand what is causing the model-measurement error and poor correlation therein. Hence as part of an ongoing study, we will perform model-measurement comparisons of the speciated components of $PM_{2.5}$, which include sulfate, nitrate, and primary and secondary organic aerosol, and evaluate whether it is emissions, chemistry, meteorology or deposition that is the source of the error. Large $PM_{2.5}$ impacts of up to 10 μg m^{-3} in southeastern Canada were predicted in July, 2012. In 2013, in-situ data show concentrations of 8-10 μg m^{-3} over the eastern U.S. reproduced well by the model. However, it still under-predicts in Texas and at several places in California, and also in Washington during the fall months. Biomass fires in southeastern Canada elevated $PM_{2.5}$ concentrations there by 5-10 μg m^{-3} during the summer months of June and July 2013. In October 2013, changes of 5-10 μg m^{-3} were predicted in eastern Texas, Louisiana, Alabama, Georgia, Idaho and southwestern Canada.

In April 2014, elevated concentrations of ~ 10-20 μg m^{-3} are observed in the in-situ measurements over the eastern U.S. and over some stations in California. The model does a good job for reproducing the concentration values less than or 12 μg m^{-3} but is unable to capture higher

concentrations. Impacts of 5-6 μg m^{-3} predicted over the Midwest for this month. The model significantly under-predicted in June when the biomass impact was minimal, indicating that probably error in biomass emissions was not the potential cause for model-measurement error.

Possible Future Biomass Impact Works

Extending the current simulation episode

As part of the future study, we will include the summer ozone seasons in the years 2011 and 2015 as part of our simulations. This is important because 2011 was a major forest fire year in Texas. Additionally, there was a significant fire event in Bastrop County in Texas in 2015 (http://www.cnn.com/2015/10/15/us/bastrop-fire-texas-hidden-pines-wildfire/). Simulating these fire events will help us understand the impacts they had on regional air quality. In this space, we will continue on our current study by using the WRF-Chem plume rise approach, grid nudging and dynamic chemical boundary conditions. Additionally, we will conduct an evaluation of speciated $PM_{2.5}$ components as compared to aggregate $PM_{2.5}$ done in this study.

Solubility basis set

Biomass burning produces copious amounts of water soluble organic compounds since they are highly oxygenated. Some examples include aldehydes such as formaldehyde and acetaldehyde. We calculated the Henry's Law constants for around 200 compounds which included aromatics, straight, branched and cyclic alkanes, alkenes, alkynes and oxygenated compounds such as aldehydes and ketones. The calculations were conducted using the EPA's Estimation Program Interface (EPI) suite. Our results indicated that the Henry's Law constants for aromatics were ~ 10^2 M atm^{-1}, branched alkanes ~10^{-1} M atm^{-1}, cyclic alkanes ~10 M atm^{-1}. The values for alkenes and alkynes ranged from 1 to10 M atm^{-1}. However, the oxygenates ranged from 10^3 to10^6 M atm^{-1}, indicating that they are the most soluble of all compounds. These could result in the formation of aqueous-phase secondary organic aerosol. In this space, it will be helpful to construct a solubility basis set (SBS) based on the Henry's Law constants of the model species classes. The approach will be similar to the Volatility Basis Set concept developed by Donahue et al. (2006). Since model species are usually lumped, we will use the approach of Carlton and Turpin to evaluate the classes; they did a calculation for SAPRC99 species.

Hodzic et al. (2014) indicated that H is a decreasing function of $\log_{10}C^*$. However, it must be noted that the saturation concentrations decrease with oxidation due to increasing O:C ratio which increases the polarity (and hence solubility) of the organic vapors. In other words, solubility is not dependent on alone $\log_{10}C^*$, it is a joint function of O:C ratio and $\log_{10}C^*$. For this study, we will first create a 1-D solubility basis set (SBS) based first on Henry's Law constants, and use the SBS to analyze field campaign data such as those from CalNex, TexAQS, SHARP, MIRAGE/MILAGRO, ICARTT, and SOAS. Hodzic et al. (2014) indicated that H is a decreasing function of $\log_{10}C^*$. However, it must be noted that the saturation concentrations decrease with oxidation due to increasing O:C ratio which increases the polarity (and hence solubility) of the organic vapors. In other words, solubility is not dependent on alone $\log_{10}C^*$, it is a joint function of O:C ratio and $\log_{10}C^*$. We will study the conceptual behavior of the SBS with temperature, similar to the studies of the general VBS (Donahue et al., 2006) and source-specific ones (e.g., Roy and Choi, 2015). The next step would be to build an SBS off the current 2-D VBS developed

by Koo et al. (2014). This VBS is based on $\log_{10}C^*$ and O:C ratio. Here, we will use the parameterization described by Hodzic et al. (2014) to relate H with $\log_{10}C^*$. The simulation data of Hodzic et al. (2014) are available online; we will use this data to develop a correlation between H and O:C ratio, to finally derive a joint function of solubility distribution as a function of $\log_{10}C^*$ and O:C ratio. In other words, Henry's Law based SBS will be parameterized from the 2-D VBS; relating Henry's Law as a function of $\log_{10}C^*$ and O:C ratio.

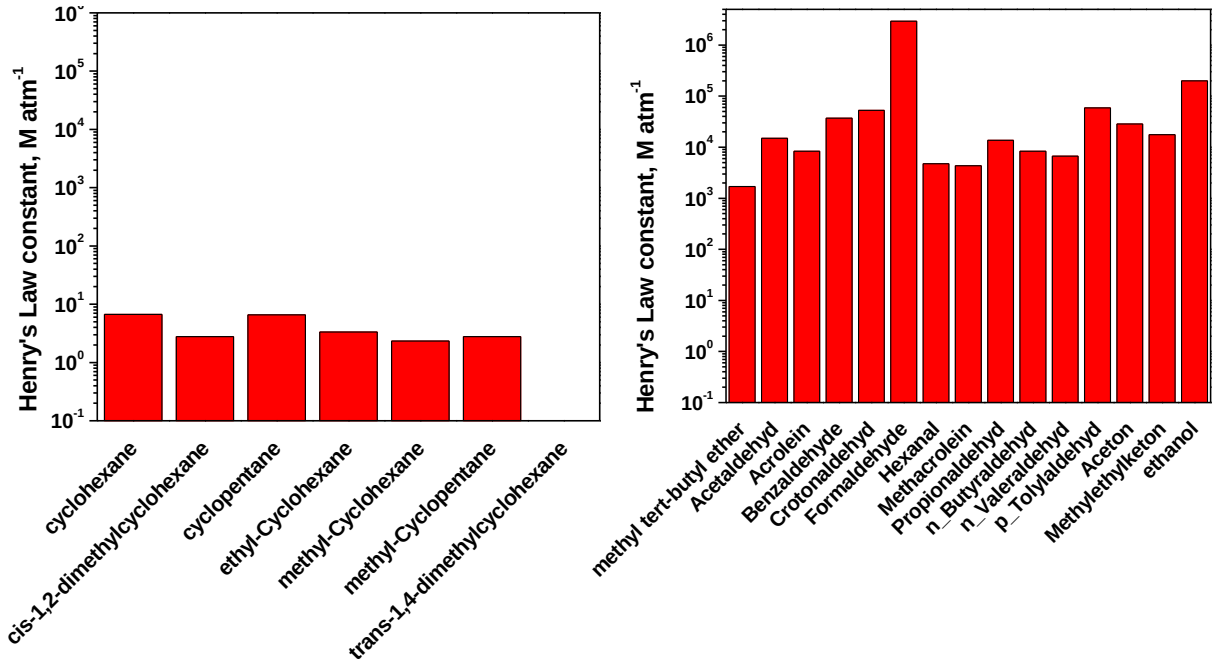

Figure 87: Comparison of Henry's Law constants. Left panel: cyclic alkanes; right panel: oxygenated compounds.

STOPS model for fire impacts

This study investigates the impact of wildfire emissions on the upper troposphere chemistry and radiative forcing. We conduct WRF-CMAQ simulations with the Fire INventory from NCAR (FINN) biomass burning emissions inventory to reproduce wildfire events that occurred during the Deep Convective Clouds and Chemistry (DC3) field campaign period (15 May-30 June 2012). Several sensitivity simulations are conducted using STOPS, a computationally efficient modeling tool, to determine the best injection height and timing of wildfire emissions, which make the most accurate simulation result compared to aircraft measurement. We quantitatively analyze the impact of wildfire plumes on the enhanced CO, O_3, and PM concentrations at the upper troposphere and also examine their contribution to the changes in radiative forcing.

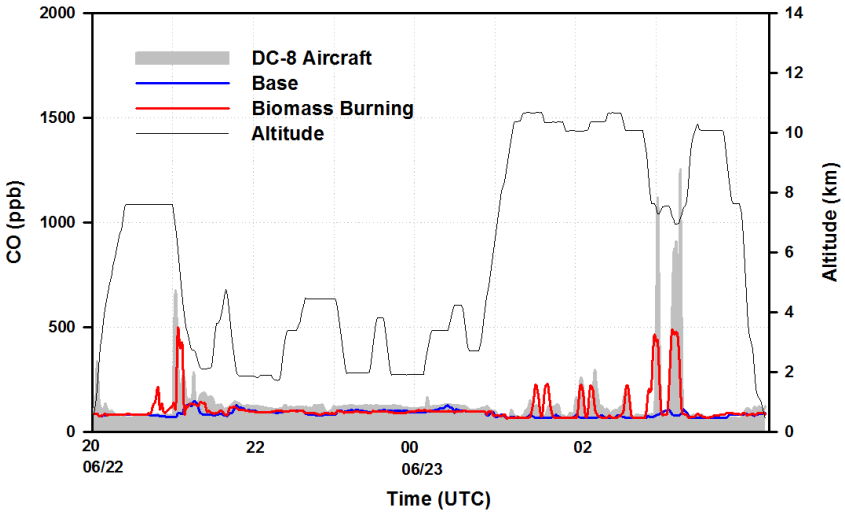

Figure 88: Comparison of CO concentrations using base model and STOPS (indicated by Biomass Burning).The STOPS version clearly is able to capture the peaks better.

Impacts of biomass burning on ammonia, sulfate and nitrate

Figure 89 plots a preliminary result showing the impact of biomass burning on ammonia concentrations. Changes of 0.1 ppbv are predicted for the southeastern U.S. and Midwest, with ~0.4 ppbv predicted in Alabama. We will evaluate these changes over a longer simulation episode (2011-2015) as part of the future work.

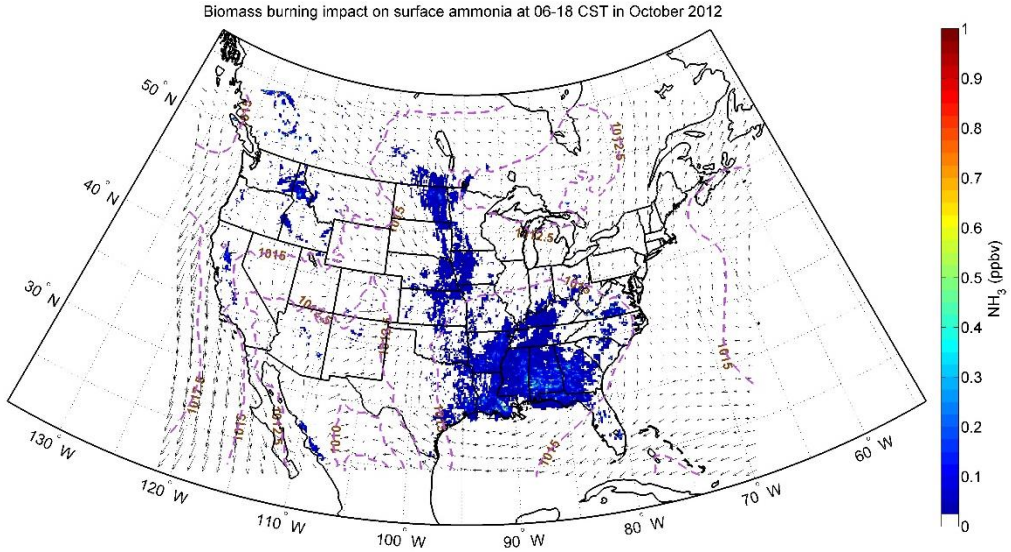

Figure 89: Effect of biomass burning on ammonia concentrations in October, 2014 (preliminary result).

Impact of plume vertical profile on surface and lower tropospheric ozone

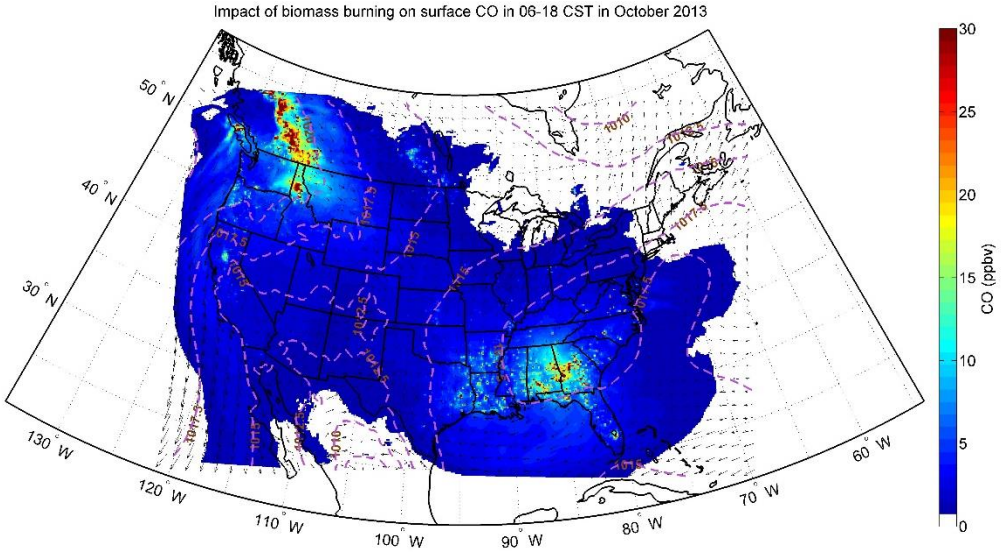

Figure 90: CO impacts in October 2013.

Figure 90 shows the carbon monoxide impacts using the WRF-Chem plume rise approach, showing significant impacts over the southeastern U.S. and Canada. We will evaluate how using different plume rise approaches affects model-measurement comparison for vertical ozone, $PM_{2.5}$ and CO profiles as part of a continuing study.

Effect of grid resolution biomass impacts: HO_x and ozone chemistry at 1 km and 4 km.

The spatial allocation of emission inventory using finer resolution grids allows consideration of detailed emission features. At heavily polluted areas, such as around an industrial power plant, coarse model grids generally average the high emissions with nearby areas, yielding an unexpectedly high emission density for the neighboring areas. Spatial allocations of emissions to model grids at different resolutions will result in differences in predicted concentrations of pollutants. As shown in Fig. 91, the CMAQ simulated NO_x spatial distributions are quite different between 1 km and 4 km grids. We can see in the 1 km case high simulated NO_x concentrations are matched well with highways in urban areas; and large nonlinearity of high simulated values are shown at airports and industrial point sources (Fig. 91-a). The 4 km case also shows high simulated NO_x at urban and industrial regions (Fig. 91-b); however it lacks the detailed textures which are clearly shown in finer resolution. Magnitudes of peak simulated NO_x in the1 km case are also bigger than in the 4 km case. Simulated O_3 is relatively low at peak simulated NO_x grid cells, which could be represented as NO_x-saturated places. Simulated O_3 hotspots are similar in the 1 km and 4 km cases. In the high NO_x environment, more HO_2 can react with NO, so HO_2 are relatively lower at urban and industrial regions, especially along highways and at industrial facilities (Figs. 91-e and f). Grid resolution impacts on low simulated HO_2 are similar to on peak simulated NO_x.

Biomass burning events can produce large amount of VOC emissions. We expect different spatial features of pollutants will be discovered around burning areas at different grid resolutions.

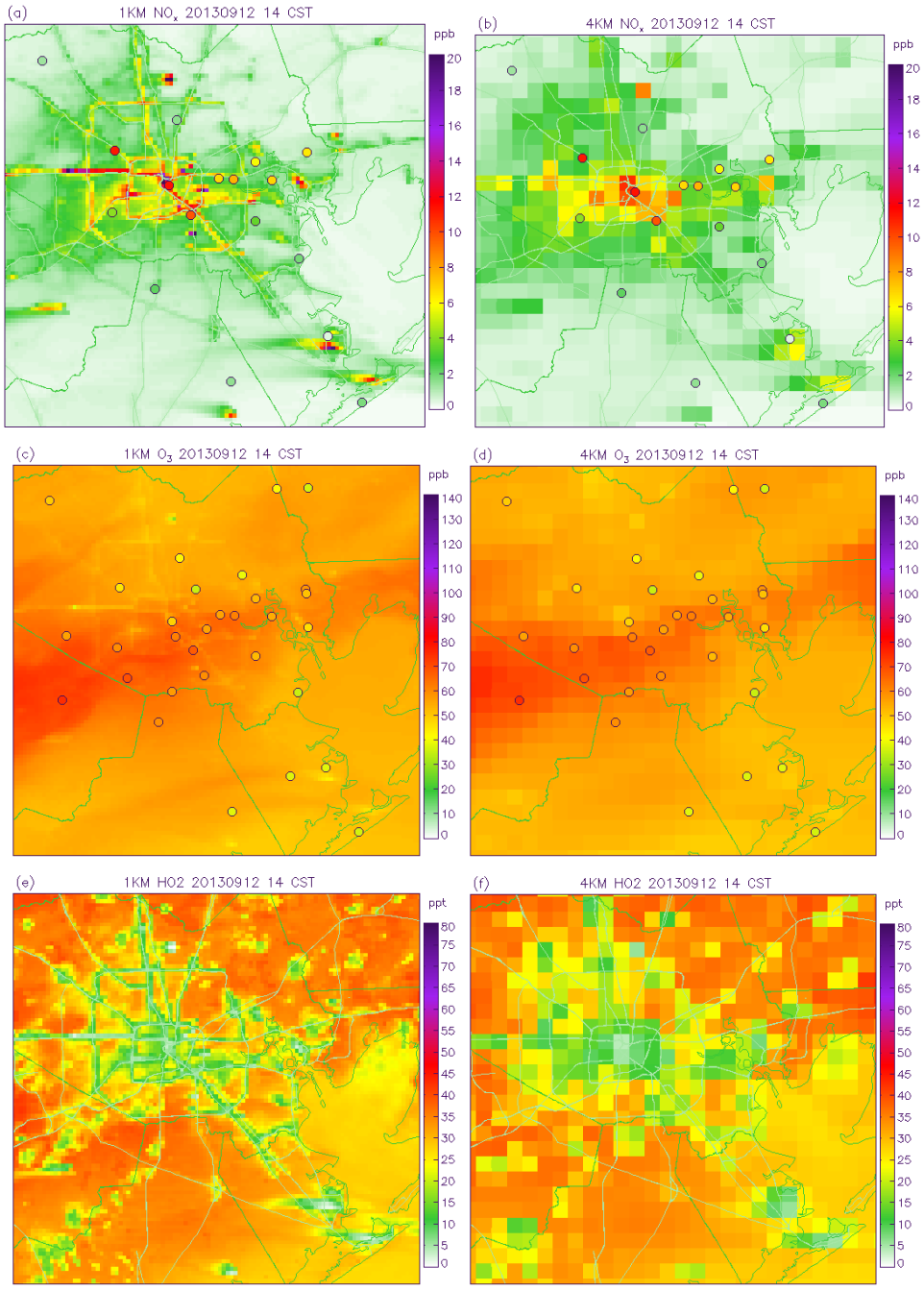

Figure 91: Spatial comparisons of surface NO_x, O_3 and HO_2 at different grid resolutions at 14 CST on September 12th, 2013 at Houston, TX: (a) 1-km with CAMS NO_x; (b) 4-km with CAMS NO_x; (c) 1-km with CAMS O_3; (d) 4-km with CAMS O_3; (e) 1-km HO_2; (f) 4-km HO_2.

Effect of biomass burning on human health

Effective assessment of health and cost effects from air pollution associated with wildfire events is critical for supporting sustainable management and policy analysis to reduce environmental damages. In this proposed study, the health impact of biomass burning events over the continental U.S. is studied using combined air quality and health impact modeling. Through the current TCEQ project, air quality modeling scenarios including biomass burning emissions were conducted using the Community Multiscale Air Quality (CMAQ) modeling system from 2012 to 2014 with a spatial resolution of 12 km. The EPA's GIS-based computer program, Environmental Benefits Mapping and Analysis Program - Community Edition (BenMAP-CE) is employed to address an inclusive figure of health and cost impact caused by changing ambient ozone and $PM_{2.5}$ concentrations due to the fire events. The basis of BenMAP-CE is the use of a damage-function approach to estimate the health impact of an applied change in air quality by comparing a biomass burning scenario (the one that includes wildfire events) with a baseline scenario (without biomass emissions). The major factors influencing such an approach are population, exposure to the pollutants, adverse health effects of a specific pollutant, and consequently economic costs. This study also examines how biomass burning across the U.S. (including Texas) influences people's health in different months, seasons and regions, and the cost impacts of wildfire events during these periods. Since biomass burning events result in higher ozone and $PM_{2.5}$ concentration values in urban regions due to long-range transport, preliminary results indicate that wildfire events cause a considerable increase in incident estimates and costs. This study demonstrates that BenMAP-CE can be successfully utilized as a proper tool to obtain health and cost impact of biomass burning events.

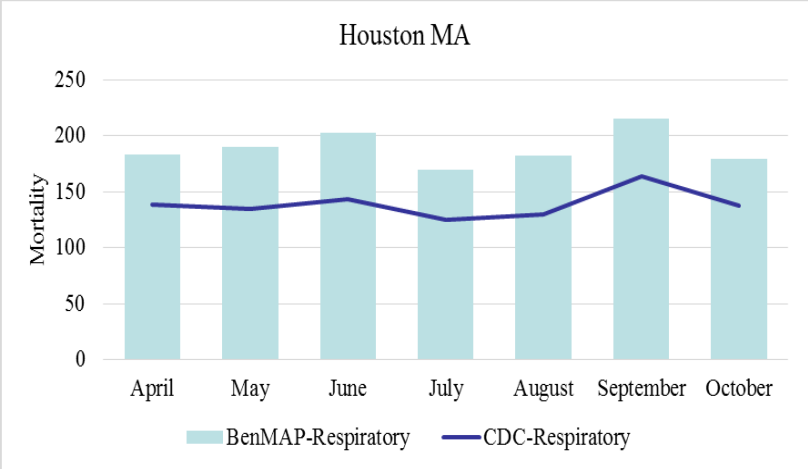

Figure 92: Deaths as the results of respiratory diseases in Houston from the EPA's BenMAP health assessment using the CMAQ simulation results and observed Centers for Disease Control and Prevention (CDC) reports.

Acknowledgments

The authors would like to thank David Westenbarger, who is the Program manager for this TCEQ project, for his useful advice during the course of this work; Christine Wiedinmyer at NCAR for help with FINN, and Greg Yarwood and Zhen Liu at Ramboll-Environ for his help on re-mapping the model species from MOZART to CB05.

References

Allen, D.J., Pickering, K.E., Pinder, R.W., Henderson, B.H., Appel, K.W., and Prados, A., 2012, Impact of lightning-NO on eastern United States photochemistry during the summer of 2006 as determined using the CMAQ model, Atmos. Chem. Phys., 12, 1737-1785

Anderson, D. C., Loughner, C. P., Diskin, G., Weinheimer, A., Canty, T. P., Salawitch, R. J. & Dickerson, R. R.,2014, Measured and modeled CO and NOy in DISCOVER-AQ: An evaluation of emissions and chemistry over the eastern US, Atmospheric Environment, 96, 78-87.

Atkinson, R. and Arey, J., 1998, Atmospheric Chemistry of Biogenic Organic. Compounds, Acc. Chem. Res., 31, 574-583

Banta, R.M., Senff, C.J., Nielsen-Gammon, J., Darby, L.S., Ryerson, T.B., Alvarez, R.J., Sandberg, S.R., Williams, E.J., Trainer, M., 2005. A bad air day in Houston. Bulletin of the American Meteorological Society 86, 657-669.

Bertschi, I. T., and D. A. Jaffe (2005) Long-range transport of ozone, carbon monoxide, and aerosols to the NE Pacific troposphere during the summer of 2003: Observations of smoke plumes from Asian boreal fires, *J. Geophys. Res*., 110, D05303, doi: 10.1029/2004JD005135.

Bey I., Jacob D.J., Yantosca, R.M., Logan, J.A., Field, B., Fiore A.M., Li, Q., Liu, H., Mickley, L.J., and Schultz, M., (2001). Global modeling of tropospheric chemistry with assimilated meteorology: Model description and evaluation, J. Geophys. Res., 106, pp. 23,073-23,096.

Bowden, J.H., Otte, T.L., Nolte, C.G., Otte, M.J., 2012. Examining interior grid nudging techniques using two-way nesting in the WRF model for regional climate modeling. J. Clim. 25, 2805-2823.

Briggs, G. A. 1975. Plume rise predictions. In *Lectures on Air Pollution and Environmental Impact Analyses*, 72–73. Boston, MA, USA: American Meteorological Society.

Bucsela, E. J., et al., 2013, A new stratospheric and tropospheric NO_2 retrieval algorithm for nadir-viewing satellite instruments: application to OMI, Atmos. Meas. Tech., 6, 2607-2626, doi: 10.5194/amt-6-2607-2013

Choi, Y., & Souri, A. H., 2015, Chemical condition and surface ozone in large cities of Texas during the last decade: Observational evidence from OMI, CAMS, and model analysis. Remote Sensing of Environment, 168, 90-101.

Choi, Y., Kim, H., Tong, D., and Lee, P., 2012, Summertime weekly cycles of observed and modeled NOx and O3 concentrations as a function of satellite-derived ozone production sensitivity and land use types over the Continental United States, Atmos. Chem. Phys., 6291-6307.

Choi, Y., Kim, J., Eldering, A., Osterman, G., Yung, Y.L., Gu, Y., Liou, K.N., 2009, Lightning and anthropogenic NOx sources over the United States and the western north Atlantic Ocean: impact on OLR and radiative effects. Geophys. Res. Lett., 36, L17806, doi: 10.1029/2009GL039381

Choi, Y., Osterman, G., Eldering A., Wang, Y., and Edgerton, E., 2010, Understanding the contributions of anthropogenic and biogenic sources to CO enhancements and outflow observed over North America and the western Atlantic Ocean by TES and MOPITT, Atmospheric Environment, 44, 2033-2042

Choi, Y., 2014, The impact of satellite-adjusted NOx emissions on simulated NOx and O3 discrepancies in the urban and outflow areas of the Pacific and Lower Middle US, Atmos. Chem. Phys., 14, 675-690

Choi, Y., Wang, Y., Yang, Q., Cunnold, D., Zeng, T., Shim, C., Luo, M., Eldering, A., Bucsela, E., Gleason, J., 2008b, Spring to summer northward migration of high O3 over the western North Atlantic, 2008b, Geophys. Res. Lett., 35, L04818, doi: 10.1029/2007GL032276

Choi, Y., Wang, Y., Zeng, T., Cunnold, D., Yang, E., Martin, R., Chance, K., Thouret, V., Edgerton, E., 2008a. Springtime transition of NO2, CO and O3 over North America: Model evaluation and analysis, Journal of Geophysical Research, 113, D20311, doi: 10.1029/2007JD009632

Choi, Y., Wang, Y., Zeng, T., Martin, R.V., Kurosu, T.P., Chance, K., 2005, Evidence of lightning NOx and convective transport of pollutants in satellite observations over North America. Geophys. Res. Lett., 32, L02805, doi: 10.1029/2004GL021436

Czader, B. H., Choi, Y., Li, X., Alvarez, S., and Lefer, B., 2015, Impact of updated traffic emissions on HONO mixing ratios simulated for urban site in Houston, Texas, Atmos. Chem. Phys., 15, 1253-1263, doi:10.5194/acp-15-1253-2015.

Czader, B.H., Li, X.S., Rappenglueck, B., 2013, CMAQ modeling and analysis of radicals, radical precursors, and chemical transformations. J Geophys Res-Atmos 118, 11376-11387.

Diner, D. J., et al., MISR level 2 aerosol retrieval algorithm theoretical basis, JPL D11400, Rev. D, Jet Propul. Lab., Pasadena, Calif., 1999a.

Diner, D. J., W. A. Abdou, H. R. Gordon, R. A. Kahn, Y. Knyazikhin, J. V. Martonchik, D. McDonald, S. McMuldroch, R. Myneni, and R. A. West, MISR level 2 ancillary products and data sets algorithm theoretical basis, JPL D-13402, Rev. B, Jet Propul. Lab., Pasadena, Calif., 1999b

Donahue, N.M., Robinson, A.L., Stanier, C.O and Pandis, S.N., 2006. Coupled Partitioning, Dilution, and Chemical Aging of Semivolatile Organics. Environmental Science and Technology, 40, 2635-2643.

Duncan, B.N., Yoshida, Y., Olson, J.R., Silman, S., Martin, R.V., Lamsal, L., Hu, Y., Pickering, K.E., Retscher, C., Allen, D.J., Crawford, J.H., 2010, Application of OMI observations to a space-based indicator of NOx and VOC controls on surface ozone formation, Atmospheric Environment, 44(18), 2213-2223.

Fiore, A.M., R.B. Pierce, R.R. Dickerson, and M. Lin (2014) Detecting and Attributing Episodic High Background Ozone Events, *Environ. Mgt*., February 2014.

Freitas, S. R., K. M. Longo, R. Chatfield, D. Latham, M. A. F. Silva Dias, M. O. Andreae, E. Prins, J. C. Santos, R. Gielow, and J. A. Carvalho Jr. 2007. Including the sub–grid scale plume rise of vegetation fires in low resolution atmospheric transport models. *Atmos. Chem. Phys.* 7 (13):3385–3398. doi: 10.5194/acp-7-3385-2007.

Freitas, S. R., K. M. Longo, J. Trentmann, and D. Latham. 2010. Technical Note: Sensitivity of 1-D smoke plume rise models to the inclusion of environmental wind drag. *Atmos. Chem. Phys.* 10 (2):585–594. doi: 10.5194/acp-10-585-2010.

Fu, J. S., N. C. Hsu, Y. Gao, K. Huang, C. Li, N. H. Lin, and S. C. Tsay. 2012. "Evaluating the influences of biomass burning during 2006 BASE-ASIA: a regional chemical transport modeling." Atmos. Chem. Phys. 12 (9):3837-3855. doi: 10.5194/acp-12-3837-2012.

Grell, G., S. R. Freitas, M. Stuefer, and J. Fast. 2011. "Inclusion of biomass burning in WRF-Chem: impact of wildfires on weather forecasts." Atmos. Chem. Phys. 11 (11):5289-5303. doi: 10.5194/acp-11-5289-2011.

Guenther, A., Baugh, B., Brasseur, G., Greenberg, J., Harley, P., Klinger, L., Serca, D., and Vierling, L., 1999, Isoprene emission estimates and uncertainties for the Central Afraican EXPRESSO study domain, J. Geophys. Res., 104, D23, 30625-30639

Guenther, A., Hewitt, C.N., Erickson, D., Fall, R., Geron, C., Graedel, T., Harley, P., Klinger, L., Lerdau, M., McKay, W.A., Pierce, T., Scholes, B., Steinbrecher, R., Tallamraju, R., Taylor, J., and Zimmerman, P., 1995, A global model of natural volatile organic compound emissions, J. Geophys. Res., 100, D5, 8873-8892

Hill, G. E.: Factors controlling the size and spacing of cumulus clouds as revealed by numerical experiments, J. Atmos. Sci., 31, 646–673, 1974.

Hodzic, A., Aumont, B., Knote, C., Lee-Taylor, J., Madronich, S., Tyndall, G., 2014. Volatility dependence of Henry's law constants of condensable organics: Application to estimate depositional loss of secondary organic aerosols. Geophysical Research Letters, 4795-4804.

Houyoux, M.R., Vulkovich, J.M., Coats, C.J., Wheeler, N.M., and Kasibhatla, P.S., 2000, Emission inventory development and processing for the Seasonal Model for Regional Air Qaulity (SMRAQ) project, J. Geophy. Res., 105, 9079-9090

Hudman, R.C., Murray, L.T., Jacob, D.J., Millet, D.B., Turquety, S., Wu, S., Blake, D.R., Goldstein, A.H., Holloway, J., and Sachse, G.W., 2009, Biogenic versus anthropogenic sources of CO in the United States, Geophys. Res. Lett., 35, L04801, doi: 10.1029/2007GL032393

Jaffe, D., I. Bertschi, L. Jaegle, P. Novelli, J.S. Reid, H. Tanimoto, R. Vingarzan, D.L. Westphal (2004) Long-range transport of Siberian biomass burning emissions and impact on surface ozone in western North America, *Geophys. Res. Lett.*, 31, L16106, doi: 10.1029/2004GL020093.

Jiang, X., C. Wiedinmyer, A.G. Carlton (2012) Aerosols from fires: an examination of the effects on ozone photochemistry in the Western United States, *Environ, Sci. Tech.*, 46, 21, 442-460, doi:10.1021/es301541k.

Kahn, Ralph A., Yang Chen, David L. Nelson, Fok-Yan Leung, Qinbin Li, David J. Diner, and Jennifer A. Logan. 2008. "Wildfire smoke injection heights: Two perspectives from space." Geophysical Research Letters 35 (4) doi: 10.1029/2007GL032165.

Kemball-Cook, S., Yarwood, G., Johnson, J., Dornblaser, B., & Estes, M., 2015, Evaluating NOx emission inventories for regulatory air quality modeling using satellite and air quality model data. Atmospheric Environment, 117, 1-8.

Kim, S.-W., McKeen, S.A., Frost, G.J., Lee, S.-H., Trainer, M., Richer, A., Angevine, W.M., Atlas, E., Bianco, L., Boersma, K.F., and et al., 2011, Evaluations of NOx and highly reactive VOC emission inventories in Texas and their implications for ozone plume simulations during the

Texas Air Quality Study 2006. Atmos. Chem. Phys., 11, 11361-11386, doi: 10.5194/acp-11-11361-2011.

Koo, B., Knipping, E., Yarwood, G., 2014. 1.5-Dimensional volatility basis set approach for modeling organic aerosol in CAMx and CMAQ. Atmospheric Environment, 95, 158-164.

Kota, S.H., Schade, G., Estes, M., Boyer, D., Ying, Q, 2015. Evaluation of MEGAN predicted biogenic isoprene emissions at urban locations in Southeast Texas. Atmospheric Environment, 110, 54-64.

Kuhlmann, G., Hartl, A., Cheung, H. M., Lam, Y. F., and Wenig, M. O., 2014, A novel gridding algorithm to create regional trace gas maps from satellite observations, Atmos. Meas. Tech., 7, 451-467, doi:10.5194/amt-7-451-2014.

Lapina, K., R.E. Honrath, R.C. Owen, M.V. Martin, G. Pfister (2006) Evidence of significant large-scale impacts of boreal fires on ozone levels in the midlatitude Northern Hemisphere free troposphere, *Geophys. Res. Lett*., 33, L10815.

Leung, F.-Y. T., J. A. Logan, R. Park, E. Hyer, E. Kasischke, D. Streets, and L. Yurganov. 2007. Impacts of enhanced biomass burning in the boreal forests in 1998 on tropospheric chemistry and the sensitivity of model results to the injection height of emissions. *J. Geophys. Res.-Atmos.* 112 (D10):D10313. doi: 10.1029/2006JD008132.

Latham, D.: PLUMP: A one-dimensional plume predictor and cloud model for fire and smoke managers, General Technical Report INT-GTR-314, Intermountain Research Station, USDA Forest Service, Nov, 1994.

Li, X., Choi, Y., Czader, B., Kim, H., 2015, the impact of the observation nudging on the simulated meteorology and ozone concentrations during DISCOVER-AQ 2013 Texas campaign. Atmos. Phys. and Chem. In review

Lilly, D. K.: On the numerical simulation of buoyant convection, Tellus, XIV, 2, 148–172, 1962.

Liu, P., Tsimpidi, A.P., Hu, Y., Stone, B., Russell, A.G., Nenes, A., 2012. Differences between downscaling with spectral and grid nudging using WRF. Atmospheric Chemistry and Physics, 12, 3601-3610.

Martin, R.V., Fiore, A.M., and Donkelaar, A.V., Space-based diagnosis of surface ozone sensitivity to anthropogenic emissions, 2004, Geophys. Res. Lett., 31, L06120, doi: 10.1029/2004GL019416

McKeen, S.A., G. Wotawa, D.D. Parrish, J.S. Holloway, M.P. Buhr, G. Hübler, F.C. Fehsenfeld, J.F. Meagher (2002) Ozone production from Canadian wildfires during June and July of 1995, *J. Geophys. Res*., 107, 4192.

Millet, D.B., Goldstein, A.H., Holzinger, R., Williams, B.J., Allan, J.D., Jimenez, J.L., Worsnop, D.R., Roberts, J.M., White, A.B., Hudman, R.C., Bertschi, I.T., Stohl, A., 2006, Chemical characteristics of north American surface layer outflow: insights from Chebogue point, Nova Scotia, J. Geophys. Res., 111, D23S53

Morris, G.A., S. Hersey, A.M. Thompson, S. Pawson, J.E. Nielsen, P.R. Colarco, W.W. McMillan, A. Stohl, S. Turquety, J. Warner, B.J. Johnson, T.L. Kucsera, D.E. Larko, S.J. Oltmans, J.C. Witte

(2006) Alaskan and Canadian forest fires exacerbate ozone pollution over Houston, Texas, on 19 and 20 July 2004. *J. Geophys. Res*., 111, D24S03.

Morton, R., Taylor, G., and Turner, J.: Turbulent gravitational convection from maintained and instantaneous sources, Proc. Roy. Soc. A, 234, 1–23, 1956.

Ngan, F., Byun, D., Kim, H., Lee, D., Rappengluck, B., Pour-Biazar, A., 2012. Performance assessment of retrospective meteorological inputs for use in air quality modeling during TexAQS 2006. Atmos. Env. 54, 86-96.

Noxon, J. F., 1978, Tropospheric NO_2, J. Geophys. Res., 83(C6), 3051–3057, doi: 10.1029/JC083iC06p03051.

Otte, T.L., 2008a. The impact of nudging in the meteorological model for retrospective air quality simulations. Part I: evaluation against national observation networks. J. Appl. Meteorol. Climatol. 47, 1853-1867.

Otte, T.L., 2008b. The impact of nudging in the meteorological model for retrospective air quality simulations. Part II: evaluating collocated meteorological and air quality observations. J. Appl. Meteorol. Climatol. 47, 1868-1887.

Palmer, P.I., Jacob, D.J., Fiore, A.M., Martin, R.V., Chance, K., and Kurosu, T.P., 2003, Mapping isoprene emissions over North America using formaldehyde column observations from space, 108, D6, 4180, doi:10.1029/2002JD002153

Parrington, M., P. I. Palmer, D. K. Henze, D. W. Tarasick, E. J. Hyer, R. C. Owen, D. Helmig, C. Clerbaux, K. W. Bowman, M. N. Deeter, E. M. Barratt, P. F. Coheur, D. Hurtmans, Z. Jiang, M. George, and J. R. Worden. 2012. The influence of boreal biomass burning emissions on the distribution of tropospheric ozone over North America and the North Atlantic during 2010. *Atmos. Chem. Phys.* 12 (4):2077–2098. doi: 10.5194/acp-12-2077-2012.

Paugam, R., M. Wooster, S. Freitas, and M. Val Martin. 2016. A review of approaches to estimate wildfire plume injection height within large-scale atmospheric chemical transport models. *Atmos. Chem. Phys.* 16 (2):907–925. doi: 10.5194/acp-16-907-2016.

Penner, J. E., L. C. Haselman, and L. L. Edwards. 1986. Smoke-plume distributions above large-scale fires-implications for simulations of nuclear winter. *J. Clim. Appl. Meteorol.* 25 (10):1434–1444. doi: 10.1175/1520-0450(1986)025<1434.

Pfister, G.G., Wiedinmyer, C., Emmons, L.K. (2008) Impacts of the fall 2007 California wildfires on surface ozone: integrating local observations with global model simulations, *Geophys. Res. Lett*., 35, L19814.

Pfister, G.G., Emmons, L.K., Hess, P.G., Lamarque, J.-F., Orlando, J-J., Walters, S., Guenther, A., Palmer, P., Lawrence, P.J., 2008, Contribution of isoprene to chemical budgets: a model tracer study with the NCAR CTM MOZART-4, J. Geophys. Res., 113, D05308

Pouliot G. and Pierce T., 2009. Integration of the Model of Emissions of Gases and Aerosols from Nature (MEGAN) into the CMAQ Modeling System, Available at: https://www.epa.gov/air-emissions-modeling/biogenic-emission-inventory-system-beis

Pouliot, George, Thomas Pierce, William Benjey, Susan M. O'Neill, and Sue A. Ferguson. 2005. "Wildfire Emission Modeling: Integrating BlueSky and SMOKE." 14th Internat. Emission Inventory Conf. "Transforming Emission Inventories Meeting Future Challenges Today", Las Vegas.

Raffuse, Sean M., Kenneth J. Craig, Narasimhan K. Larkin, Tara T. Strand, Dana Coe Sullivan, Neil J. M. Wheeler, and Robert Solomon. 2012. "An Evaluation of Modeled Plume Injection Height with Satellite-Derived Observed Plume Height." Atmosphere 3 (1):103.

Rappenglück, B., B. Lefer, B. Czader, X. Li, J. Golovko, S. Alvarez, J. Flynn, C. Haman, and N. Grossberg. 2011. University of Houston Moody Tower 2010 Ozone Formation Research Monitoring; Project Grant No. 582-5-64594-FY10-14, Prepared for the Texas Commission on Environmental Quality, TX 2011

Rodgers, C.D., 2000, Inverse Methods for Atmospheric Sounding: Theory and Practice, World Sci., Hackensack, N.J.

Roy, A.A. and Choi, 2015. Temperature dependence of source specific Volatility Basis Sets for motor vehicle exhaust. Atmospheric Environment, 119, 258-261.

Seinfeld, J. H. and Pandis, S. N., 2012, Atmospheric chemistry and physics: from air pollution to climate

Sharkey, T.D., Singsaas, E.L., Lerdau, T., Geon, C.D., 1999, Weather effects on isoprene emission capacity and applications in emissions in emission algorithms, Ecological Applications, 9, 1131-1137

Shim, C., Wang, Y., Choi, Y., Palmer, P.I., Abbot, D.S., and Chance, K., 2005, Constraining global isoprene emissions with Global Ozone Monitoring Experiment (GOME) formaldehyde column measurements, J. Geophys. Res., 110, D24301, doi: 10.1029/2004JD005629

Sillman, S., 1995. The use of NOy, H_2O_2, and HNO_3 as empirical indicators for ozone-NO_x-hydrocarbon sensitivity in urban locations. J. Geophys. Res., 100, 14,175–14,188.

Simpson, J. and Wiggert, S.: Models of precipitating cumulus towers, Mon. Wea. Rev., 97, 471–489, 1969.

Singh, H.B., D. Herlth, R. Kolyer, R. Chatfield, W. Viezee, L.J. Salas, Y. Chen, J.D. Bradshaw, S.T. Sandholm, R. Talbot, G.L. Gregory, B. Anderson, G.W. Sachse, E. Browell, A.S. Bachmeier, D.R. Blake, B. Heikes, D. Jacob, and H. E. Fuelberg (1996) Impact of biomass burning emissions on the composition of the South Atlantic troposphere: reactive nitrogen and ozone, *J. Geophys. Res*., 101, D19, pp. 24,203-24,219.

Sinha, P., L. Jaegle, P. Hobbs, Q. Liang (2004) Transport of biomass burning emissions from southern Africa, *J. Geophys. Res.-Atmos.,* 109, D20204.

Smagorinsky, J.: General circulation experiments with the primitive equations. Part I, The basic experiment, Mon.Wea. Rev., 91, 99–164, 1963.

Tai, Edward, Michele Jimenez, Ou Nopmongcol, Gary Wilson, Gerry Mansell, Bonyoung Koo, and Greg Yarwood. 2008. Boundary conditions and fire emissions modeling. Novato, CA: ENVIRON International Corporation.

Turner, J. S.: Buoyancy effects in fluids, Cambridge Univ. Press, Cambridge, 368 pp., 1973.

Val Martin, M., Honrath, R.E., Owen, R.C., Pfister, G., Fialho, P., Barata, F. (2006) Significant enhancements of nitrogen oxides, black carbon, and ozone in the North Atlantic lower free troposphere resulting from North American boreal wildfires, *J. Geophys. Res.-Atmos.*, 111, D23S60.

Val Martin, M., J. A. Logan, R. A. Kahn, F. Y. Leung, D. L. Nelson, and D. J. Diner. 2010. Smoke injection heights from fires in North America: analysis of 5 years of satellite observations. *Atmos. Chem. Phys.* 10 (4):1491–1510.

van der Werf, G. R., Randerson, J. T., Giglio, L., Collatz, G. J., Kasibhatla, P. S., 2006, and Arellano Jr., A. F.: Interannual variability in global biomass burning emissions from 1997 to 2004, Atmos. Chem. Phys., 6, 3423-3441, doi:10.5194/acp-6-3423-2006.

Warneke, C., de Gouw, J.A., Del Negro, L., Brioude, J., McKeen, S., Stark, H., Kuster, W.C., Goldan, P.D., Trainer, M., Fehsenfeld, F.C., Wiedinmyer, C., Guenther, A.B., Hansel, A., Wisthaler, A., Atlas, E., Holloway, J.S., Ryerson, T.B., Peischl, J., Huey, L.G. caseHanks, A.T., 2010. Biogenic emission measurement and inventories determination of biogenic emissions in the eastern United States and Texas and comparison with biogenic emission inventories. Journal of Geophysical Research, 115, D00F18, doi: 10.1029/2009JD012445

Wiedinmyer, C., Akagi, S.K., Yokelson, R.J., Emmons, L.K., Al-Saadi, A., Orlando, J.J., Soja, A.J., 2011. The Fire INventory from NCAR (FINN): a high resolution global model to estimate the emissions from open burning. Geoscientific Model Development, Vol.4, Issue 3, 625-641.

Western Governors Association/Western Regional Air Partnership. 2005. 2002 Fire Emission Inventory for the WRAP Region – Phase II. Air Sciences Inc.

Yienger, J. J., and H. Levy II, 1995, Empirical model of global soil-biogenic NOχ emissions, J. Geophys. Res., 100(D6), 11447–11464, doi: 10.1029/95JD00370. John Wiley & Sons.

Zhao, C., Wang, Y., Choi, Y., and Zeng, T., 2009, summertime impact of convective transport and lightning NOx production over North America: modeling dependence on meteorological simulations, Atmos. Chem. Phys., 9, 4315-4327.

Appendix A

List of standard CMAQ variables (Gas phase species)

Var_Name	Unit	Var_Name	Unit
NO2	ppmv	NO	ppmv
O	ppmv	O3	ppmv
NO3	ppmv	O1D	ppmv
OH	ppmv	HO2	ppmv

N2O5	ppmv	HNO3	ppmv
HONO	ppmv	PNA	ppmv
H2O2	ppmv	XO2	ppmv
XO2N	ppmv	NTR	ppmv
ROOH	ppmv	FORM	ppmv
ALD2	ppmv	ALDX	ppmv
PAR	ppmv	CO	ppmv
MEO2	ppmv	MEPX	ppmv
MEOH	ppmv	HCO2	ppmv
FACD	ppmv	C2O3	ppmv
PAN	ppmv	PACD	ppmv
AACD	ppmv	CXO3	ppmv
PANX	ppmv	ROR	ppmv
OLE	ppmv	ETH	ppmv
IOLE	ppmv	TOL	ppmv
CRES	ppmv	TO2	ppmv
TOLRO2	ppmv	OPEN	ppmv
CRO	ppmv	MGLY	ppmv
XYL	ppmv	XYLRO	ppmv
ISOP	ppmv	ISPD	ppmv
TERP	ppmv	SO2	ppmv
SULF	ppmv	ETOH	ppmv
ETHA	ppmv	CL2	ppmv
CL	ppmv	HOCL	ppmv
CLO	ppmv	FMCL	ppmv
HCL	ppmv	BENZENE	ppmv
BENZRO2	ppmv	SESQ	ppmv

List of standard CMAQ variables (Aqueous phase species)

Var_Name	Unit	Var_Name	Unit
ASO4J	µg m^{-3}	ASO4I	µg m^{-3}
ANH4J	µg m^{-3}	ANH4I	µg m^{-3}

ANO3J	μg m^{-3}	ANO3I	μg m^{-3}
AALKJ	μg m^{-3}	AXYL1J	μg m^{-3}
AXYL2J	μg m^{-3}	AXYL3J	μg m^{-3}
ATOL1J	μg m^{-3}	ATOL2J	μg m^{-3}
ATOL3J	μg m^{-3}	ABNZ1J	μg m^{-3}
ABNZ2J	μg m^{-3}	ABNZ3J	μg m^{-3}
ATRP1J	μg m^{-3}	ATRP2J	μg m^{-3}
AISO1J	μg m^{-3}	AISO2J	μg m^{-3}
ASQTJ	μg m^{-3}	AORGCJ	μg m^{-3}
AORGPAJ	μg m^{-3}	AORGPAI	μg m^{-3}
AECJ	μg m^{-3}	AECI	μg m^{-3}
A25J	μg m^{-3}	ACORS	μg m^{-3}
NUMATKN	μg m^{-3}	ASOIL	μg m^{-3}
NUMACC	μg m^{-3}	NUMCOR	μg m^{-3}
SRFATKN	μg m^{-3}	SRFACC	μg m^{-3}
SRFCOR	μg m^{-3}	AH2OJ	μg m^{-3}
AH2OI	μg m^{-3}	ANAJ	μg m^{-3}
ACLJ	μg m^{-3}	ACLI	μg m^{-3}
ANAK	μg m^{-3}	ACLK	μg m^{-3}
ASO4K	μg m^{-3}	ANH4K	μg m^{-3}
ANO3K	μg m^{-3}	AH2OK	μg m^{-3}
AISO3J	μg m^{-3}	AOLGAJ	μg m^{-3}
AOLGBJ	μg m^{-3}	NH3	μg m^{-3}
SV_ALK	μg m^{-3}	SV_XYL1	μg m^{-3}
SV_XYL2	μg m^{-3}	SV_TOL1	μg m^{-3}
SV_TOL2	μg m^{-3}	SV_BNZ1	μg m^{-3}
SV_BNZ2	μg m^{-3}	SV_TRP1	μg m^{-3}
SV_TRP2	μg m^{-3}	SV_ISO1	μg m^{-3}
SV_ISO2	μg m^{-3}	SV_SQT	μg m^{-3}

Appendix B

List of deliverables

(a) Base 2011 NEI inventory, processed by SMOKE: speciated into CB05, gridded into 12 km domain over the Continental United States, and allocated temporally.
(b) FINN inventory re-gridded into CMAQ format and speciated into CB05 (mapped from MOZART); evaluated with two plume rise approaches.
(c) Biogenic emissions input files from BEIS.
(d) WRF-generated meteorological fields.
(e) CMAQ model output with and without biomass emissions.
(f) Model output plots both these cases, along with difference plots.

Appendix C

WRF Namelist

```
&time_control
 run_days                  = 250,
 run_hours                 = 0,
 run_minutes               = 0,
 run_seconds               = 0,
 start_year                = 2014,
 start_month               = 03,
 start_day                 = 24,
 start_hour                = 00,
 start_minute              = 00,
 start_second              = 00,
 end_year                  = 2014,
 end_month                 = 11,
 end_day                   = 07,
 end_hour                  = 00,
 end_minute                = 00,
 end_second                = 00,
 interval_seconds          = 10800
```

```
 input_from_file                 = .true.,
 history_interval                = 60,
 frames_per_outfile               = 1,
 restart                         = .false.,
 restart_interval                = 9999999,
 io_form_history                  = 2
 io_form_restart                  = 2
 io_form_input                    = 2
 io_form_boundary                   = 2
 debug_level                     = 0
 auxinput11_interval_s             = 1800,
 auxinput11_end_h                  = 99999,
 auxinput4_inname                  = "wrflowinp_d<domain>",
 auxinput4_interval               = 180,
 io_form_auxinput4                  = 2
 /
&domains
 time_step                       = 90,
 time_step_fract_num               = 0,
 time_step_fract_den               = 1,
 max_dom                          = 1,
 e_we                            = 470,
 e_sn                            = 310,
 e_vert                          = 28,
 p_top_requested                   = 10000,
 num_metgrid_levels                = 30,
 num_metgrid_soil_levels           = 4,
```

```
 dx                                  = 12000,
 dy                                  = 12000,
 grid_id                             = 1,
 parent_id                           = 0,
 i_parent_start                      = 1,
 j_parent_start                      = 1,
 parent_grid_ratio                   = 1,
 parent_time_step_ratio              = 1,
 feedback                            = 1,
 smooth_option                       = 0
 eta_levels                          = 1.000, 0.996, 0.990, 0.980, 0.970,
                                     0.960, 0.950, 0.940, 0.930, 0.920,
                                     0.910, 0.895, 0.880, 0.865, 0.850,
                                     0.825, 0.800, 0.775, 0.750, 0.720,
                                     0.660, 0.570, 0.475, 0.370, 0.250,
                                     0.145, 0.045, 0.000
 /
&physics
 mp_physics                          = 3,
 ra_lw_physics                       = 1,
 ra_sw_physics                       = 1,
 radt                                = 12,
 sf_sfclay_physics                   = 1,
 sf_surface_physics                  = 2,
 bl_pbl_physics                      = 1,
 bldt                                = 0,
 cu_physics                          = 1,
```

```
 cugd_avedx                  = 1,
 cudt                        = 5,
 isfflx                      = 1,
 ifsnow                      = 1,
 icloud                      = 1,
 surface_input_source        = 1,
 num_soil_layers             = 4,
 sf_urban_physics            = 0,
 sst_update                  = 0,
 /
&fdda
 grid_fdda                   = 1,
 gfdda_inname                = "wrffdda_d<domain>",
 gfdda_end_h                 = 99999,
 gfdda_interval_m            = 180,
 fgdt                        = 0,
 if_no_pbl_nudging_uv        = 0,
 if_no_pbl_nudging_t         = 0,
 if_no_pbl_nudging_q         = 0,
 if_zfac_uv                  = 0,
  k_zfac_uv                  = 10,
 if_zfac_t                   = 0,
  k_zfac_t                   = 10,
 if_zfac_q                   = 0,
  k_zfac_q                   = 10,
 guv                         = 0.0003,
 gt                          = 0.0003,
```

```
 gq                      = 0.0003,
 if_ramping              = 1,
 dtramp_min              = 60.0,
 io_form_gfdda           = 2,
 grid_sfdda              = 0,
 sgfdda_inname           = "wrfsfdda_d<domain>",
 sgfdda_end_h            = 72,
 sgfdda_interval_m       = 180,
 io_form_sgfdda          = 2,
 /
&dynamics
 w_damping               = 1,
 diff_opt                = 1,
 km_opt                  = 4,
 diff_6th_opt            = 0,
 diff_6th_factor         = 0.12,
 base_temp               = 290.
 damp_opt                = 0,
 zdamp                   = 5000.,
 dampcoef                = 0.2,
 khdif                   = 0,
 kvdif                   = 0,
 non_hydrostatic         = .true.,
 moist_adv_opt           = 1,
 scalar_adv_opt          = 1,
 /
```

```
&bdy_control
spec_bdy_width                  = 5,
spec_zone                       = 1,
relax_zone                      = 4,
specified                       = .true.,
nested                          = .false.,
/
 &grib2
/
 &namelist_quilt
nio_tasks_per_group = 0,
nio_groups = 1,
/
```